1-1-2016

Effects of Nanoscale Aggregation on Mechanical Properties and Local Dynamics of Precise Acid- and Ion-Containing Polymers

Luri Robert Middleton
University of Pennsylvania, middleton.lrobert@gmail.com

Effects of Nanoscale Aggregation on Mechanical Properties and Local Dynamics of Precise Acid- and Ion-Containing Polymers

Abstract
Acid- and ion-containing polymers have interchain interactions that alter polymer behavior at the nano, micro, and bulk length scales. Strong secondary-bonds act as thermo-reversible physical crosslinks between chains which drive self-assembly. Tuning theses interactions can modify bulk polymer properties including stiffness, toughness, melt viscosity, resilience, clarity, abrasion resistance and puncture resistance. Furthermore, understanding and improving the relevant factors that control transport properties would have vast implications on developing solid polymer electrolytes (SPEs) for technologically important applications including water desalination, ion exchange membranes and microelectronics. This thesis explores the structure – processing – morphology - property relationships of acid and ionic functionalized polymers.

Improvements in synthetic techniques and advancements in characterization methods have enabled new studies of associating polymer systems. Synthesis of entangled, high molecular weight, linear polyethylene (PE) chains functionalized with interacting pendant groups (acidic or ionic) placed periodically along the polymer backbone represent a new class of associating polymers. These polymers with periodic distributions of acid groups are much more homogenous than the commercially available polymers. Previous studies of these polymers with greater structural homogeneity revealed great variety in morphologies of the nano-aggregated polar groups within the non-polar polymer matrix.

This thesis correlated the morphologies with bulk properties through real-time X-ray scattering and tensile deformation at a range of temperatures and sample compositions. New, transient morphologies and hierarchical morphologies were observed which coincided with unusual tensile strain hardening. These results indicate that improvements in synthetic control of polymers can enhance physical properties such as tensile strain-hardening, through cooperative bonding between chains.

The structural regularity of precise polyethylenes also enables robust comparisons between experiments and computer simulations. At pico- to nano-seconds time scales and length scales of polymer and aggregate dynamics, neutron scattering and molecular dynamics simulations were combined to extend the knowledge of the molecular-level aggregated polymer dynamics. These experiments provide a baseline for future studies of ion-conduction in associating polymer melts.

Degree Type
Dissertation

Degree Name
Doctor of Philosophy (PhD)

Graduate Group
Materials Science & Engineering

First Advisor
Karen I. Winey

Keywords
Acid Copolymer, Ionomer, Precise Polymer

Subject Categories
Mechanics of Materials | Physical Chemistry | Polymer and Organic Materials

EFFECTS OF NANOSCALE AGGREGATION ON MECHANICAL PROPERTIES AND LOCAL DYNAMICS OF PRECISE ACID- AND ION-CONTAINING POLYMERS

Luri Robert Middleton

A DISSERTATION

in

Materials Science and Engineering

Presented to the Faculties of the University of Pennsylvania

in

Partial Fulfillment of the Requirements for the

Degree of Doctor of Philosophy

2016

Supervisor of Dissertation

_____

Karen I. Winey, Professor, Materials Science and Engineering

Graduate Group Chairperson

_____

Shu Yang, Professor, Materials Science and Engineering

Dissertation Committee

Amalie L. Frischknecht, Principal Member of Technical Staff, Sandia National Laboratory

James Runt, Professor, Materials Science and Engineering, Pennsylvania State University

Shu Yang, Professor, Materials Science and Engineering, University of Pennsylvania

EFFECTS OF NANOSCALE AGGREGATION ON MECHANICAL PROPERTIES AND LOCAL DYNAMICS OF PRECISE ACID- AND ION-CONTAINING POLYMERS

To my Family and Friends,

for their everlasting encouragement and support.

ACKNOWLEDGMENT

I owe a great debt to my thesis advisor, Prof Karen Winey, who has enabled me to try and fail, to learn and grow as a scientist. She's trusted me, provided countless opportunities, and the freedom to intellectually explore. I've traveled overseas without oversight, lead and collaborated outside of the university, and explored new experimental techniques for the group. By her example I've learned more through graduate school than I'd ever expected and I'll appreciate this for the rest of my career.

I owe a great thanks to my classmates who've worked alongside me these past 5 years. By height: Nick, Frank, Dan, Daksh and Jacob. You guys are the backbone of my MSE experience. To all the fun late-nights, homework assignments, napping in the grad lounge and being there to celebrate every milestone of the thesis process. I can't imagine this place without you all.

I would like to thank the MSE community at the Penn. I want to recognize my preceding colleagues in the Winey group who I learned so much from: Jae-Hong, Francisco, Rose, Mike, Walter, Sharon, Cathy, and Jim. And those of the Winey group who joined after me and made these years fulfilling and fun: Phil, Ted, James, Lu, and Eric. To my MSE compatriots who drew me to Penn and set the example to live up to: Jason, Elaine, Rahul, Mike, Rob, Cathy, Jim, Ryan, Ashley, Vicky, Pavan, Emma, Danny, Nadia, Spencer and Boris. The time has flown by. The helpful, everyday faces of the MSE department whom deserve great thanks for all the work that keeps the building running. Especially, I would like to acknowledge Steve for his expertise in all equipment and also thank Pat, Vicky, Rico, Raymond, Irene and Jamie.

A very special thank you is in order for people who meant so much to me outside work. To my old buddies who know me best and still stick around for some reason, by year: Baird, Eoin, Brendan, Tom and Joe (15, 14, 14, 14, and 10 years guys, and what have we done to show for it?). Joe and Casey whose friendship means so much to me and stood the test of time and distance. To Brian and Jill, who made graduate school life fun and always worth celebrating together- let's never stop.

Most importantly, I dedicate this thesis to my biggest supporters, my family. To my loving wife who has lived and endured through the highs and lows of graduate school by my side. You are my fellow adventurer, counterweight, and source of cute chaos in my life. Thank you for always making it new, different, exciting and worth every moment. To my parents and sister who have always been there for me, cheering me on in everything I've attempted. To the Mohanraj family whom graciously and warmheartedly welcomed me into their family as one of their own. To my Grandparents, who I strive to be like in all ways. It is the support you have all given me that emboldens me to pursue even the things I fear I cannot achieve. Thank you.

ABSTRACT

EFFECTS OF NANOSCALE AGGREGATION ON MECHANICAL PROPERTIES AND LOCAL DYNAMICS OF PRECISE ACID- AND ION-CONTAINING POLYMERS

Luri Robert Middleton

Professor Karen I. Winey

Acid- and ion-containing polymers have interchain interactions that alter polymer behavior at the nano, micro, and bulk length scales. Strong secondary-bonds act as thermo-reversible physical crosslinks between chains which drive self-assembly. Tuning theses interactions can modify bulk polymer properties including stiffness, toughness, melt viscosity, resilience, clarity, abrasion resistance and puncture resistance. Furthermore, understanding and improving the relevant factors that control transport properties would have vast implications on developing solid polymer electrolytes (SPEs) for technologically important applications including water desalination, ion exchange membranes and microelectronics. This thesis explores the structure – processing – morphology - property relationships of acid and ionic functionalized polymers.

Improvements in synthetic techniques and advancements in characterization methods have enabled new studies of associating polymer systems. Synthesis of entangled, high molecular weight, linear polyethylene (PE) chains functionalized with interacting pendant groups (acidic or ionic) placed periodically along the polymer backbone represent a new class of associating polymers. These polymers with periodic distributions of acid groups are much more homogenous than the commercially available polymers. Previous studies of these polymers with greater structural homogeneity

revealed great variety in morphologies of the nano-aggregated polar groups within the non-polar polymer matrix.

This thesis correlated the morphologies with bulk properties through real-time X-ray scattering and tensile deformation at a range of temperatures and sample compositions. New, transient morphologies and hierarchical morphologies were observed which coincided with unusual tensile strain hardening. These results indicate that improvements in synthetic control of polymers can enhance physical properties such as tensile strain-hardening, through cooperative bonding between chains.

The structural regularity of precise polyethylenes also enables robust comparisons between experiments and computer simulations. At pico- to nano-seconds time scales and length scales of polymer and aggregate dynamics, neutron scattering and molecular dynamics simulations were combined to extend the knowledge of the molecular-level aggregated polymer dynamics. These experiments provide a baseline for future studies of ion-conduction in associating polymer melts.

TABLE OF CONTENTS

LIST OF TABLES

LIST OF FIGURES

CHAPTER 1

INTRODUCTION

Motivation

Predicting and controlling material properties from first-principles is critical to the development of new materials and the advancement of science and technology.[1] Polymers are inherently difficult to describe due to the structural and dynamic heterogeneity of macromolecules. The vast assortment of attainable molecular compositions, chain architectures, and resultant hierarchical morphologies lead to a near-infinite variety of material systems. The dynamics of polymers can exhibit varied length scale dependencies, multiple thermally activated processes, and orders-of-magnitude difference in the timescales of dynamics. These characteristics all contribute to the bulk properties of polymers.

The addition of non-covalent, interchain interactions to macromolecules result in increasingly convoluted but tunable material properties.[2, 3] Strong secondary-bonds in acid- and ion-containing polymers cause nano-scale aggregation of the polar groups which act as thermo-reversible physical crosslinks, generating tough thermoplastics. Many commercially relevant acid- and ion-containing polymers exist with wide-ranging applications from golf-ball coatings to shape-memory polymers, with approximately 300 million pounds of ionomers produced worldwide.[4] The time- and temperature-dependent physical crosslinks govern many of the improved bulk properties including the stiffness, toughness, melt viscosity, resilience, clarity, abrasion resistance and puncture resistant properties of the polymer.[5] Synthetic chemistry is becoming more specific and controlled creating the possibility to engineer molecules. To realize the full potential of applications

utilizing nano-aggregates in polymers the fundamental understanding of their chemical structure – processing – morphology – property relationship is imperative.[6]

Background Information

Synthesis of Precise Polyethylenes. Acyclic diene metathesis (ADMET) is an olefin metathesis polymerization of symmetric diene monomers.[7, 8] This synthetic route yields a controlled method to incorporate pendant groups in linear polymers, which can be used to elucidate fundamental structure-property relationships in polyethylene (PE) based acid- and ion-containing polymers. By utilizing monomers of three different sizes the ADMET synthesis produces functionalized polyethylenes with precisely periodic pendant groups on every 21st, 15th, and 9th carbon atom along a PE chain, Figure 1.1.[9] The ADMET step-growth polymerization and subsequent deprotection and hydrogenation, yields functionalized polymers that are typically unattainable through other chain-growth polymerization methods due to differences in the reactivity of the comonomers.[7] Furthermore ADMET synthesized precise polyethylenes have been functionalized with various pendant group chemistries including acrylic acid (AA), phosphonic acid (PA), and imidizolium bromide.[9] The level of homogeneity in functional group distribution in precise polyethylenes is unprecedented and has enabled a series of fundamental polymer studies.[8, 10-14]

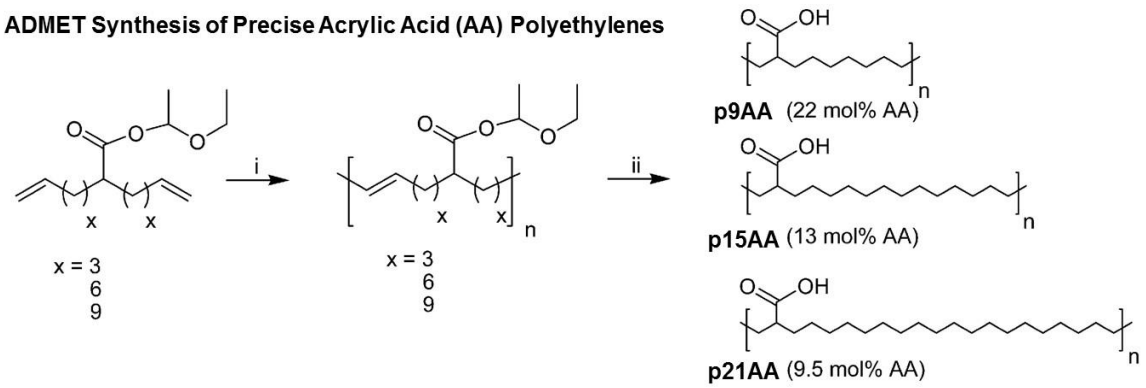

Figure 1.1. General ADMET polymerization procedure to achieve perfectly linear polyethylenes functionalized with precisely sequenced pendants acrylic acid (AA) groups. (i) first-generation Grubbs' catalyst, polymerization; (ii) deprotection through exhaustive hydrogenation; (Reproduced from Baughman et al.[9]).

Morphology of Acid- and Ion-containing Polymers. Aggregates form when the polar groups micro- or nano-phase separate from the low dielectric polymer medium. These aggregates range from hydrogen bonded dimers to larger aggregates comprised of both hydrogen-bonded acid groups and electrostatically bonded ionic groups. The shape, composition and spatial arrangement of the nano-scale aggregates in commercial ionomers have been debated heavily in the literature.[15, 16] This is due to the difficulty in characterizing these systems where there is molecular heterogeneity (chain architecture, acid placement, etc.), difficulty in directly imaging irregular nanoscale morphologies, and the broad distributions of near-aggregate or unperturbed polymer behavior that contribute to the measured bulk properties.

The ADMET synthesized polymers with pendant groups (acidic or ionic) placed periodically along the polymer backbone have greater structural homogeneity than commercial polymers and previously studied random copolymers. Studies of precise

polyethylenes revealed a rich variety in morphologies of the nano-aggregated polar groups within the non-polar polymer matrix, Figure 1.2.[17-19] When the pendant acid groups are distributed frequently along the PE chain, every 9 or 15 carbons, the ability of PE to crystallize is disrupted and the polymers are amorphous. The nano-aggregates are discrete, depicted as colored globules in Figure 1.2, demonstrating the liquid-like distribution of aggregates throughout the amorphous polymer matrix. When the acid groups are distributed further apart, as with the 21 methylene spacer polymers, the methylene can crystallize forming a layered morphology. The layered morphology indicates ordering of the PE spacers, depicted in yellow, as well as ordering of the acid-rich aggregates co-existing with amorphous polymer.

The periodic spacing of functional groups along the backbone with absolute consistency lends itself not only to rigorous experimental work, but is ideal for computer simulations. The homogenous and structurally simple chemical structure has been modeled with both coarse grained and atomistic molecular dynamic (MD) simulations. Simulations reveal real-space structural information at the nano-scale, indicating a variety of aggregate shapes and extending the experimentally accessible knowledge and material systems.[20-24] Simulations could even guide the synthesis of new materials.

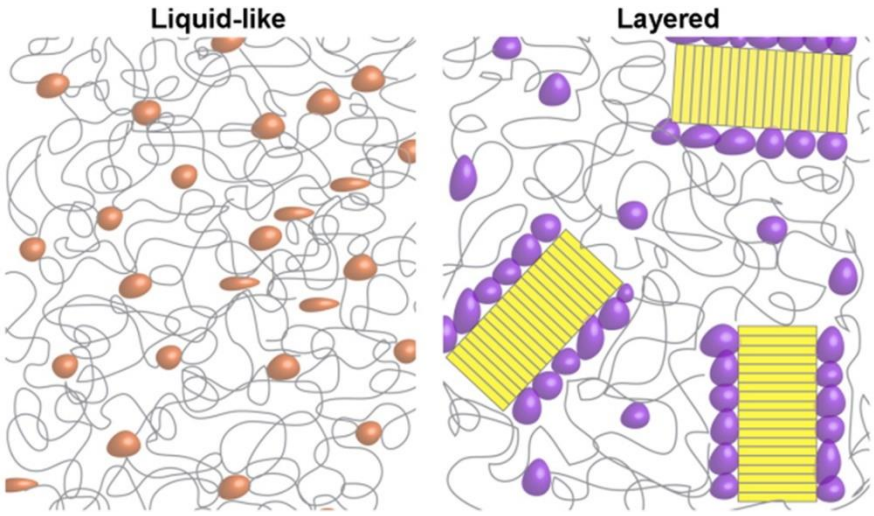

Figure 1.2. Experimentally determined morphology types of precise polyethylenes at room temperature. The aggregates (colored globules) in the PE matrix (grey lines) and PE crystals (yellow). (Reproduced from Buitrago *et al.*[25]).

In short, precision polyethylenes have enabled rigorous studies of the factors that impact equilibrium morphology, specifically pendant spacing, acid type, mono- and geminal-functionalization, temperature, cation type and neutralization level.[8, 9, 17, 26-29]

Outline of Thesis Chapters

This thesis adds to the fundamental understanding of associating polymers by studying the mechanical properties and local dynamics of precise polymers. This thesis correlates the morphologies with bulk tensile properties through real-time X-ray scattering and uniaxial deformation at a range of temperatures and sample compositions. New, transient morphologies and hierarchical morphologies were observed that coincide with unusual tensile strain hardening. These results indicate that improvements in synthetic control of polymers can enhance physical properties such as tensile strain-hardening, by enabling cooperative bonding between chains. Additionally, the structural regularity of precise polyethylenes also enable robust comparisons between experiments and

computer simulations. At pico- to nano-seconds time scales and nano-meter length scales of polymer and aggregate dynamics, neutron scattering and molecular dynamics simulations were combined to study the molecular-level aggregated polymer dynamics. These experiments provide a baseline for future studies of ion-conduction in associating polymer melts.

In Chapter 2 we report the first mechanical property measurements of precise acrylic acid functionalized polyethylenes (p*x*AA). The unusual tensile properties observed were correlated with the evolution of morphologies during deformation. The semi-crystalline precise polymer (p21AA) displays strain hardening which coincides with the originally isotropic acid-rich layered morphologies strongly aligning with acid layers perpendicular to the strain direction, demonstrating the facile nature of H-bonding within the acid aggregates. When the alkyl spacer is only nine carbons (p9AA), the precise polymer withstands strains of > 1000% without failing, because the liquid-like assembly of acid aggregates permits the acid groups to exchange without developing substantial anisotropy in the structure. Both p21AA and p9AA maintain their morphology type during deformation with considerable plastic deformation and only modest increases in their interaggregate distances. In contrast, p15AA exhibits a structural transformation from nominally spherical to layered aggregate morphologies during tensile deformation as evidenced by higher order peaks at intermediate scattering angles and larger interaggregate spacing, coinciding with substantial strain hardening. This was the first report of an amorphous precise polymer forming a layered morphology. Commensurate with this morphology transformation, p15AA is the toughest of the precise acrylic acid functionalized polyethylenes. This chapter was published in *Macromolecules* in 2015.[28]

Chapter 3 is an extension of Chapter 2 wherein the role of acid periodicity and acid chemistry are examined. We report the morphology evolution under tensile deformation for strictly linear polyethylenes with associating functional groups with either precise or pseudo-random periodicity. *In situ* X-ray scattering measurements during elongation reveal that periodic acid group placement along the backbone is required to form hierarchical layered morphologies that coincide with strain hardening. This phenomenon was observed in both semi-crystalline (21 carbon spacer) and amorphous (15 carbon spacer) precise acid polyethylenes with acrylic, geminal acrylic and phosphonic acids. Polymers with non-periodic (pseudo-random) acid placement fail to form layered morphologies and instead retain a liquid-like distribution of nominally spherical acid aggregates. These results broadly indicate that hierarchical acid-rich layered structures, commensurate with improved mechanical properties, form in polymers with strictly periodic chemical structures and sufficient chain mobility for chain alignment during elongation. This was the first report of p15PA exhibiting a layered morphology through elevated temperature deformation. Finally, precise polyethylenes with more strongly associating functional groups have higher modulus. This chapter is currently under review at *Macromolecules*.[30]

Chapter 4 is an extension of Chapter 2 and 3, where the role of lithium-neutralization is examined in precise acrylic acid polyethylenes. *In situ* X-ray scattering measurements simultaneously captured the changes in the inter-aggregate peak and amorphous halo during uniaxial elongation. The role of spacing between acid groups along the linear PE backbone, fraction of neutralized acid groups, and effect of temperature were examined. This study indicates that the neutralization of the acid-functionalized precise polymers with metal salts significantly increases the thermal transitions and mechanical

properties, however, the morphologies remain controlled by the polymer structure. In the melt state the highest acid and ionic content lead to the highest modulus and ultimate tensile strength due to the long-lived ionic aggregates. Strain hardening was observed at elevated temperatures when significant chain orientation occurred corresponding with an anisotropic layered morphology, indicating some chain mobility through facile aggregate exchange. Although the liquid-like morphology persist in the acid form of p9AA, the ionomer with the shortest methylene spacer, p9AA-35%Li, forms a layered morphology during deformation at elevated temperature ($T > T_g$) when the ionic aggregates are long-lived.

In Chapter 5 the melt state dynamics were investigated for a series of the precise acrylic acid polyethylenes. The acrylic acid groups form hydrogen-bonded acid aggregates within the polyethylene (PE) matrix that are discrete (according to atomistic MD simulations). The dynamics of these nanoscale heterogeneous morphologies were investigated from picosecond to nanosecond timescales by both quasi-elastic neutron scattering (QENS) experiments and fully atomistic molecular dynamics (MD) simulations performed by A. Frischknecht. Two dynamic processes were observed at these timescales, with the faster processes being spatially-restricted local motions and the slower process identified as the structural relaxation of the polymer backbone. Higher acid contents, or shorter PE spacers between pendant acid groups, slow the structural relaxation timescale and introduce greater dynamic heterogeneity. The dynamics of specific hydrogen atom positions along the backbone indicate varied dynamics near and far from acid aggregates, however, at longer timescales acid aggregates rearrange and the dynamics of all hydrogens converge implying a characteristic time scale for the passage of chains between aggregates. The characterization of the nanoscale chain

dynamics in these associating polymer systems both provides validation of simulation force fields and provides understanding of dynamic heterogeneity in associating polymers. This chapter will be submitted shortly to *Macromolecules*.[31]

Chapter 6 presents the conclusions of the dissertation and a discussion of ongoing and future work. Appendix A discusses the dynamics of precise ethylene ionomers containing ionic liquid functionality. Appendix B presents a summary of the high frequency dielectric relaxation spectroscopy experiments. Appendix C contains the Fourier-transform infrared spectroscopy characterization of residual protecting groups in precise acrylic acid polymers. Appendices D and E contain additional information for Chapters 2 and 5, respectively.

References

1. *Materials Genome Initiative for Global Competitiveness* **2011**.

2. Ouchi, M.; Terashima, T.; Sawamoto, M. *Chemical Reviews* **2009,** 109, (11), 4963-5050.

3. Lutz, J.-F.; Lehn, J.-M.; Meijer, E. W.; Matyjaszewski, K. *Nature Reviews Materials* **2016,** 1, 16024.

4. Grady, B. P. *Polymer Engineering & Science* **2008,** 48, (6), 1029-1051.

5. Greviskes, B. P.; Bertoldi, K.; Deschanel, S.; Samuels, S. L.; Spahr, D.; Cohen, R. E.; Boyce, M. C. *Polymer* **2010,** 51, (15), 3532-3539.

6. Lehn, J.-M. *Angewandte Chemie International Edition* **2013,** 52, (10), 2836-2850.

7. Baughman, T. W.; Wagener, K. B., Recent Advances in ADMET Polymerization. In *Metathesis Polymerization*, Buchmeiser, M. R., Ed. Springer Berlin Heidelberg: Berlin, Heidelberg, 2005; pp 1-42.

8. Wagener, K. B.; Boncella, J. M.; Nel, J. G. *Macromolecules* **1991,** 24, (10), 2649-2657.

9. Baughman, T. W.; Chan, C. D.; Winey, K. I.; Wagener, K. B. *Macromolecules* **2007,** 40, (18), 6564-6571.

10. Atallah, P.; Wagener, K. B.; Schulz, M. D. *Macromolecules* **2013,** 46, (12), 4735-4741.

11. Boz, E.; Wagener, K. B.; Ghosal, A.; Fu, R.; Alamo, R. G. *Macromolecules* **2006,** 39, (13), 4437-4447.

12. Leonard, J. K.; Hopkins, T. E.; Chaffin, K.; Wagener, K. B. *Macromolecular Chemistry and Physics* **2008,** 209, (14), 1485-1494.

13. O'Gara, J. E.; Wagener, K. B.; Hahn, S. F. *Die Makromolekulare Chemie, Rapid Communications* **1993,** 14, (10), 657-662.

14. Sworen, J. C.; Smith, J. A.; Wagener, K. B.; Baugh, L. S.; Rucker, S. P. *Journal of the American Chemical Society* **2003,** 125, (8), 2228-40.

15. Eisenberg, A.; Kim, J.-S., *Introduction to ionomers*. Wiley: New York, 1998.

16. Eisenberg, A.; Hird, B.; Moore, R. B. *Macromolecules* **1990,** 23, (18), 4098-4107.

17. Seitz, M. E.; Chan, C. D.; Opper, K. L.; Baughman, T. W.; Wagener, K. B.; Winey, K. I. *J. Am. Chem. Soc.* **2010,** 132, (23), 8165-8174.

18. Buitrago, C. F.; Alam, T. M.; Opper, K. L.; Aitken, B. S.; Wagener, K. B.; Winey, K. I. *Macromolecules* **2013,** 46, (22), 8995-9002.

19. Buitrago, C. F.; Opper, K. L.; Wagener, K. B.; Winey, K. I. *ACS Macro Letters* **2012,** 1, (1), 71-74.

20. Hall, L. M.; Seitz, M. E.; Winey, K. I.; Opper, K. L.; Wagener, K. B.; Stevens, M. J.; Frischknecht, A. L. *Journal of the American Chemical Society* **2012,** 134, 574-87.

21. Hall, L. M.; Stevens, M. J.; Frischknecht, A. L. *Physical Review Letters* **2011,** 106, 127801.

22. Hall, L. M.; Stevens, M. J.; Frischknecht, A. L. *Macromolecules* **2012,** 45, 8097-8108.

23. Bolintineanu, D. S.; Stevens, M. J.; Frischknecht, A. L. *ACS Macro Letters* **2013**, 206-210.

24. Bolintineanu, D. S.; Stevens, M. J.; Frischknecht, A. L. **2013**.

25. Buitrago, C. F.; Jenkins, J. E.; Opper, K. L.; Aitken, B. S.; Wagener, K. B.; Alam, T. M.; Winey, K. I. *Macromolecules* **2013,** 46, (22), 9003-9012.

26. Opper, K. L.; Markova, D.; Klapper, M.; Müllen, K.; Wagener, K. B. *Macromolecules* **2010,** 43, (8), 3690-3698.

27. Rojas, G.; Inci, B.; Wei, Y.; Wagener, K. B. *Journal of the American Chemical Society* **2009,** 131, (47), 17376-17386.

28. Middleton, L. R.; Szewczyk, S.; Azoulay, J.; Murtagh, D.; Rojas, G.; Wagener, K. B.; Cordaro, J.; Winey, K. I. *Macromolecules* **2015,** 48, (11), 3713-3724.

29. Aitken, B. S.; Buitrago, C. F.; Heffley, J. D.; Lee, M.; Gibson, H. W.; Winey, K. I.; Wagener, K. B. *Macromolecules* **2012,** 45, (2), 681-687.

30. Middleton, L. R.; Trigg, E. B.; Schwartz, E.; Opper, K. L.; Travis, W. B.; Wagener, K. B.; Winey, K. I. *Macromolecules* **Submitted**.

31. Middleton, L. R.; Tarver, J. D.; Cordaro, J. G.; Madhusudan, T.; Soles, C. L.; Frischknecht, A. L.; Winey, K. I. *Macromolecules* **Submitted**.

CHAPTER 2

Hierarchical Acrylic Acid Aggregate Morphologies Produce Strain-Hardening in Precise Polyethylene-Based Copolymers

Introduction

The structure and properties of acid-containing polymers and ionomers have been of interest for decades in various applications where tunable and mechanically robust polymers are of great importance. Extensive studies of the morphology and deformation of polyethylene-based (PE) acid-containing random copolymers and their ionomers have been performed on inherently complex materials having highly branched architectures, semi-crystalline morphologies, and unknown aggregate morphologies.[1] The effect of acid content on mechanical properties has been difficult to describe because of the interrelated factors of T_g, T_m, the degree of crystallinity and crystal structures formed in acid copolymers, all of which can be affected by acid content.[2-8] It has been well established that crystallinity dominates many mechanical properties in semi-crystalline polymers and requires multi-component models to represent the crystalline and amorphous domains.[9-14]

Deformation models of semi-crystalline polymer, such as the Davies model, incorporate the degree of crystallinity, crystal structure, and assumption of the modulus of the lamellae and modulus of the amorphous domain.[9, 10, 13, 14] Polyethylene deformation mechanisms and the relation with mechanical properties have been well studied with these models such that lamellae slip, crystal melting, alignment of amorphous chains and fiber-like morphology development are largely understood. The effect of copolymerizing

PE with acid groups, however, is more complex because of the simultaneous changes in T_g, T_m, and the degree of crystallinity with acid content. For example, the yielding behavior of poly(ethylene-co-methacrylic acid) random copolymers (EMAA) show an unusual minimum in Young's modulus with increasing %MAA. The origin of this minimum is the competition between the increased T_g of the amorphous PE domains and the concurrent loss of crystallinity with increasing acid content.[11] Since the modulus of a lamellae is ~1,000 larger than the modulus of the amorphous domains it has been difficult to describe how acid groups affect mechanical properties outside of the effect on crystalline content. Also, copolymer structures with irregular placement of the acid functionality may lead to acid-rich and acid-deficient domains that further complicate analysis.

To overcome these complexities a model polymer requires well-controlled and uniform chemical structure. One such set of model materials is the so-called *precise* acid copolymers which are polymerized by acyclic diene metathesis (ADMET).[15, 16] Precise acid copolymers have a fixed number of carbons between each pendant acid group along a strictly linear PE backbone. Table 2.1 shows three precise copolymers with a pendant acrylic acid group (AA) on every 9th, 15th, or 21st carbon. This structural simplicity and the ability to study systematic changes in the chemical structure have enabled a series of fundamental studies of acid copolymers. The morphology of these model polymers has been studied extensively at room temperature and at elevated temperature.[16-27] Furthermore, experiments and simulations have provided novel insight into the microstructures and the local dynamics of the polymers and ions. [28-30] Greater homogeneity in the acid- and ion-group distribution along the backbone leads to better defined interaggregate spacing in X-ray scattering.[16, 24, 25, 27, 28, 31, 32] In contrast, comparable random copolymers have a broader distribution of inter-acid distances such

that the X-ray scattering peak is often too broad and too weak to confidently measure small structural changes.

Table 2.1. Polymer nomenclature, composition and chemical structure of the precise copolymers.

Sample Name	Acid Concentration (mol%)	Carbons between COOH	Chemical Structure
p21AA	9.5%	21	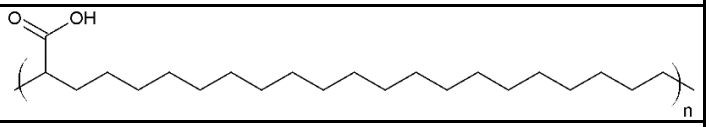
p15AA	13%	15	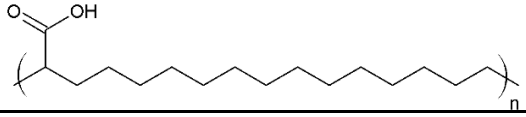
p9AA	22%	9	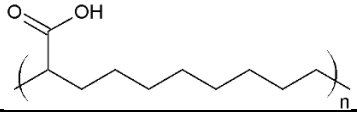

Atomistic molecular dynamics (MD) simulations of p9AA at 150°C found that the functional groups form compact isolated acid aggregates with 2-5 acid groups.[23] The compact isolated aggregates were also found by atomistic MD simulations at 120°C for p9AA, p15AA and p21AA and, moreover, the scattering patterns generated from these simulations and X-ray scattering experiments at 120°C are in good agreement.[22] Upon neutralization with metal cations, MD simulations showed a change in the aggregate morphology to stringy, branched aggregates or percolated aggregates.

Previous X-ray scattering studies of the precise acrylic acid copolymers at room temperature have identified either layered (p21AA) or liquid-like (p9AA, p15AA)

morphologies.[18] The layered morphology in p21AA is semi-crystalline with acid groups assembling into layers perpendicular to the polymer chains. The semi-crystalline nature of p21AA is also evident in NMR and DSC. Upon cooling from above the melting temperature to room temperature, p21AA crystallizes which transforms the compact isolated aggregates evident in atomistic MD into the layered morphology. The precise acrylic acid polymers with shorter alkyl spacer lengths between acid groups (p9AA and p15AA) have a liquid-like morphology that is characterized by an amorphous PE matrix and liquid-like packing of the compact, isolated aggregates. Unlike p21AA, cooling p9AA and p15AA from elevated temperature to room temperature fails to induce crystallization, so the liquid-like morphology at room temperatures is likely to possess compact isolated aggregates comparable to those found by atomistic MD simulations at elevated temperatures.

These three precise acrylic acid copolymers provide an opportunity to directly measure the effect of acid concentration on mechanical properties both with and without lamellae present at room temperature. In this study X-ray scattering is collected simultaneously to tensile deformation such that changes in mechanical properties can be directly related to changes in morphology. *In situ* measurements were also performed on linear low density polyethylene and a strictly linear polyethylene for comparison.

Experimental Section

Materials. The synthesis method and morphology of well-defined poly(ethylene-*co*-acrylic acid) copolymers[16] and strictly linear polyethylene[33] were reported previously. In brief, a symmetric diene was synthesized with a protected acrylic acid group, these macromonomers were polymerized using acyclic diene metathesis (ADMET), and then the double bonds were hydrogenated and the acid group deprotected. Synthesis details

of the poly(ethylene-*co*-acrylic acid) copolymers used in this study are reported in the supplemental information.[34] The sample nomenclature is p*x*AA, where p indicates a precise copolymer, *x* is the carbon spacing length (*x* = 9, 15 or 21) between pendant acrylic acid (AA) groups, Table 2.1. In addition to the precise copolymers, linear low density polyethylene (LLDPE) and ADMET synthesized strictly linear, precise PE (termed pPE)[33, 35] were studied for comparison. LLDPE was purchased from Sigma Aldrich (428108) and used as received. The molecular weights were measured by GPC, Table 2.2.

Table 2.2. Polymer thermal characterization (DSC) and molecular characterization (GPC) of the samples used in this work.

Sample Name	T_g (°C)	T_m (°C)	% Crystallinity ΔH_m (J/g)	M_n (kg/mol)	PDI (M_w/M_n)
p21AA	13	46.0	22% 60.5	18.3	1.9
p15AA	3	-	-	62.7	1.8
p9AA	7	-	-	41.5	1.9
LLDPE	-15	109	57% 157.4	Melt index 100g/ 10 min	
pPE		129	62% 172.1	44.9	1.8

Sample Preparation. Samples were prepared for both X-ray scattering characterization and tensile testing with the same procedure. Films were melt-pressed in a Carver 4122 hot press at 150ºC, which is above the T_g and T_m, for 20 m. The films are then subject to rapid cooling (~15ºC/min) through a heat exchanger with circulating tap water. The tensile samples were punched from films using a custom dogbone shaped die. The gage length was 10mm with lateral dimensions of 5mm x 0.13mm and was based on

the sample dimension ratios reported in ASTM Microtensile Specimens Standard (D1708 – 10). The custom die enables the testing of small quantities of sample and also serves to localize the deformation of the sample such that the X-ray scattering captures representative portions of deformation during *in situ* testing. All films were aged a minimum of 3 days in an evacuated desiccator at room temperature before conducting experiments.

DSC. Differential scanning calorimetry (DSC) measurements were performed using a Q2000 differential scanning calorimeter (TA instruments) at a scan rate of 10 °C/min. To reduce the influence of moisture, samples were melted inside an evacuated desiccator, then transferred and sealed into hermetic pans under inert atmosphere. Sealed sample pans were aged at room temperature for a minimum of 3 days. Thermal transitions were extracted from the first scan with T_g at the point of inflection and T_m as the maximum in the melting peak. Values were found to be comparable to previous published data.[16, 18, 21]

Tensile Testing. Room temperature tensile tests were performed on the dogbone shaped samples using an Instron Model 5564 Table Mounted Materials Testing System. Uniaxial tensile test samples were conducted at three strain rates, $\dot{\varepsilon}$=0.016, 0.17, 0.83s^{-1}. Stress and strain were calculated using initial sample cross-section. Additionally, cyclic uniaxial deformation tests were performed. Samples were deformed to a specific strain (ε=10, 25, 50, 100, 200, 400, 800, 1500, 2000%), then the crosshead reversed direction until the applied force returns to 0N, and subsequently the sample is deformed to a new, larger, strain and repeated until sample failure. The strain rate was held constant ($\dot{\varepsilon}$=0.17s^{-1}) for both extension and contraction of the sample. The difference in the applied strain and the residual strain at 0N force separates the elastic and plastic deformation of the sample.

Simultaneous X-ray Scattering and Tensile Testing. Synchrotron X-ray scattering was conducted at beamline 5ID-D (DND-CAT) of the Advanced Photon Source (APS) at Argonne National Laboratory. Room temperature tensile tests of the dogbone shaped samples were conducted on an Instron model 8500 Materials Testing System. The dual servo-hydraulic actuators maintain the center of the sample in the beamline throughout the *in situ* experiment with a strain rate of $0.17s^{-1}$. For the semi-crystalline samples, which exhibit necking, scattering data was collected from within the necked region. Engineering stress-strain values were calculated based on the initial dimensions of the sample and the force-displacement measurements from the Instron instrument. Simultaneously with sample deformation, two-dimensional X-ray scattering data was collected using a MAR-CCD detector at a sample-to-detector distance of 320.7 mm and X-ray energy of 17 keV (λ=0.73Å). This experimental setup provides X-ray scattering information with a large *q*-range of $1.54\text{-}17.98nm^{-1}$ to capture information from length scales of $d = 0.3–6.5$ nm. Exposure times of 1 s were used to obtain sufficient counting statistics for resolution purposes, while also minimizing the collection time needed to accurately determine the structural evolution during continuous deformation. Additionally, a 6 s delay between exposures was necessary to refresh the detector. Silver behenate and amorphous carbon were used to calibrate the scattering angle and normalize detector counts, respectively. The scattering signals were corrected for beam intensity fluctuations, dark counts and Kapton window background scattering. Two-dimensional data reduction and analysis were performed using the Datasqueeze software.[31]

Results and Discussion

Tensile Deformation. The five polymers studied exhibit strikingly different mechanical behaviors under uniaxial deformation, Figure 2.1a. Overall, the higher acid content samples deform to much higher strains, however, the acid content does not coincide with systematic changes in tensile strength (σmax), see Table 2.3. The precise copolymer with the longest spacer (p21AA), linear low density polyethylene (LLDPE), and pPE exhibit mechanical behavior typical of semi-crystalline polymers, Figure 2.1b. The % crystallinity and molecular weight are known to substantially alter the polymer modulus, σmax, εmax and ability to strain harden. Crystallinity typically strongly impacts yielding properties, while molecular weight is strongly tied to strain hardening. [36, 37] The LLDPE and p21AA, which have relatively low molecular weight, exhibit similar yield stress, and yield strains (Figure **2.1**b), and the values for LLDPE agree with values reported by the manufacturer. As expected, the higher crystallinity in pPE leads to higher moduli and yield stress than LLDPE and p21AA, and enhancement to εmax due to higher molecular weight.[36, 37] Interestingly, while the decreased percent crystallinity resulting from the presence of acid groups in p21AA relative to LLDPE (22% vs. 57%, respectively) affects the elastic modulus, it does not substantially impact the yield stress or strain. The εmax of p21AA is similar to commercial ethylene-co-methacrylic acid copolymers of comparable acid content.[38] The ductility of semi-crystalline acid-containing copolymers surpass that of the PE homopolymer with similar molecular weight due to the interactions between acid groups which increases the effective molecular weight and is believed to more evenly distribute the stress throughout the sample.[39]

Linear low density polyethylene (LLDPE), pPE and the precise copolymer with the longest spacer (p21AA) exhibit mechanical behavior typical of semi-crystalline polymers, Figure 2.1b. The linear elastic regime at low strain is followed by a yield point

at ~ 12% and necking. LLDPE and p21AA exhibit similar yield stress, and yield strains (Figure 2.1b), and the values for LLDPE agree with values reported by the manufacturer. As expected, the higher crystallinity in pPE leads to higher moduli and yield stress than LLDPE. Interestingly, while the decreased percent crystallinity resulting from the presence of acid groups in p21AA relative to LLDPE (22% vs. 57%, respectively) affects the elastic modulus, it does not substantially impact the yield stress or strain. The ε_{max} of p21AA is similar to commercial ethylene-co-methacrylic acid copolymers of comparable acid content.[38] The ductility of semi-crystalline acid-containing copolymers surpass that of the PE homopolymer with similar M_w due to the interactions between acid groups which effectively increases the M_w and is believed to more evenly distribute the stress throughout the sample.[39]

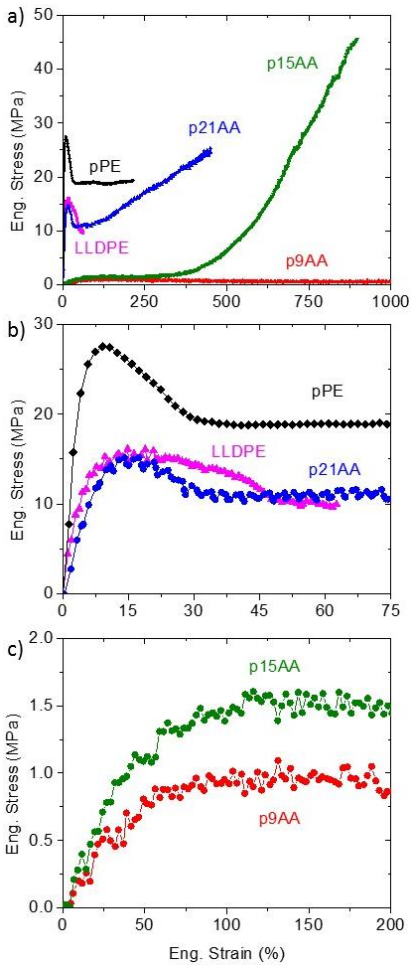

Figure 2.1. a) Engineering stress-strain tensile data for five polymers plotted on the same scale. The strain rate is $\dot{\varepsilon}$ =0.17s^{-1}. The yielding behavior at low strain is highlighted in b) for the semi-crystalline materials (LLDPE, pPE, p21AA) and c) for the amorphous materials (p15AA, p9AA).

Table 2.3. The average and standard deviation of the engineering stress and strain properties measured from 5 replicate samples at $\dot{\varepsilon}$=1.7s^{-1}. Tensile curves shown in Supplemental Information (Figure S2). The modulus of the strain-hardening mechanism, E*, was determined from the slope of the upturn in tensile plot. The onset of the strain-hardening mechanism, ε*, was determined by eye.

	E 10^6 Pa	σ_{yield} 10^6 Pa	ε_{yield} (%)	E^* 10^6 Pa	ε* (%)	σ_{max} 10^6 Pa	ε_{max} (%)
LLDPE	416 ±7.8	13.9 ±0.8	14.1 ±1.1	-	-	13.6 ±.3	43.1 ±19.2
pPE	722 ±114	27.1 ±0.9	11.1 ±1.5	-	-	27.2 ±0.9	213 ±142.7
p21AA	187 ±3.4	14.9 ±2.3	12.7 ±2.9	2.1 ±1.1	59 ±17	18.3 ±4.1	311.6 ±105.7
p15AA	30 ± 13	1.5 ±0.6	79.8 ±12.1	17.1 ±51.	327 ±46	39.8 ±23.2	695.5 ±155.6
p9AA	15 ± 2	1.0 ±0.1	121.9 ±29.2	.3 ±.1	691 ±165	1.4 ±0.6	1345.9 ±270.2

The tensile properties are distinctly different for p15AA and p9AA, wherein the higher acid content disrupts crystallinity and the materials are amorphous. Both amorphous samples deform homogenously and have yield points at much lower stress with similar yielding behavior to elastomers, Figure 2.1c.[40, 41] The yield points, based upon the plateau of the stress-strain curve following the elastic regime, occur at significantly higher strain (~100%) and lower stress than the semi-crystalline samples. While the stress-strain curves are similar below 300% strain, they differ substantially above this critical strain, referred to as ε^* in Table 2.3. The sample with the longer carbon spacer,

p15AA, exhibits a pronounced upturn in the tensile stress indicating a change in the deformation mechanism and the modulus of this strain-hardening upturn (E^*) is reported in Table 2.3. This strain-hardening is reminiscent of vulcanized natural rubber where the increase in strength corresponds to strain-induced crystallization.[40-43] The engineering stress near failure (σ_{max}) of p15AA is the highest of the samples tested, particularly when considering engineering stress does not account for the substantially decreased cross sectional area of the samples at high strains. The p15AA copolymer has an optimal fraction of acid content out of the materials reported here to maximize mechanical toughness in these precise materials. Although p9AA has the highest acid content, it exhibits the lowest yield stress and the highest ε_{max} ~1300%. Surprisingly, by increasing the acid content, the precise copolymer p9AA exhibits stress-strain behavior similar to vulcanized polyisoprene rubber.[40, 41, 43] This significant difference in mechanical properties between the materials cannot be explained by M_w alone (Table 2.2) as the intermediate M_w sample, p9AA, has the lowest modulus, yield point and the highest elongation at failure. Further, the substantial difference in mechanical behavior between the two amorphous samples cannot be explained by the ~5C° difference in T_g. The *in situ* scattering results below identify the origins of these intriguing differences in mechanical behavior.

Figure 2.2 shows the varied stress-strain behavior of the acid copolymers in response to different deformation rates. The most dramatic change in the stress-strain behavior is for the highest acid content sample, p9AA, which transitions from an easily deformed polymer film with negligible strain hardening, to a highly strain-hardening sample at high strain rates. Specifically, in p9AA the onset of strain hardening decreases from ε^*=600% at 0.17s^{-1} to ε^*=400% at 0.83s^{-1}, with a corresponding increase of the modulus of

strain-hardening from 0.3MPa to 40MPa. The higher the acid content, the greater the sensitivity to tensile strain rate indicating that the H-bonded acid aggregate relaxation timescales are important to the tensile deformation mechanism. Ionomers, the acid copolymer neutralized with metal cations, are known to have thermo-reversible physical crosslinks related to the relaxation time of the polymer backbone with a polar aggregate.[44-48] At elevated temperatures, the lifetime of these aggregates become comparable to the deformation rates allowing the ionomer to flow under stress. A similar effect occurs in these acid copolymers where the hydrogen bonding is much weaker than the Coulombic interactions in ionomers such that the conditions for flow occur at room temperature and slow ($\dot{\varepsilon}$~0.17^{-1}) deformation rates. Temporary hydrogen bonded networks have also been reported to modify viscoelastic properties in polymer solutions, elastomer systems and polymer melts where transient supramolecular structures are attributed to their strengthening.[49-51]

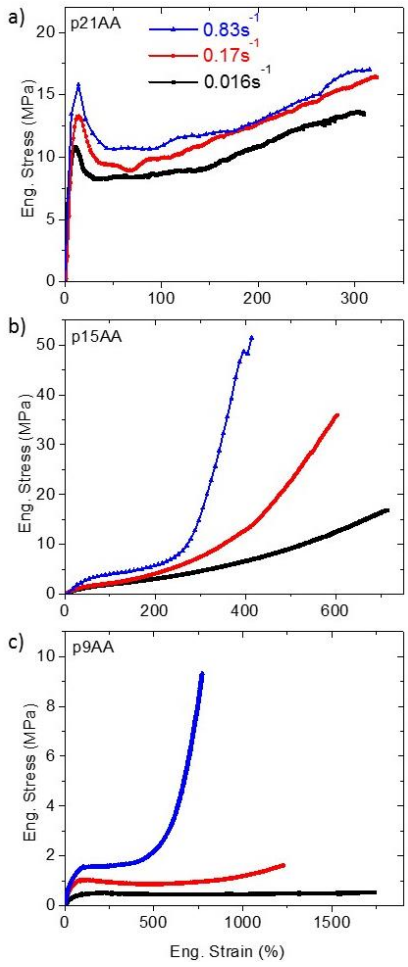

Figure 2.2a-c. The tensile behavior of precise acrylic acid copolymers at three strain rates, $\dot{\varepsilon}$=0.016s^{-1} (black), 0.17s^{-1} (red), 0.83s^{-1} (blue). The p9AA copolymer has the highest acid content and is most sensitive to strain rate.

Cyclic Deformation. The contributions of recoverable and non-recoverable deformation are examined through cyclic tensile tests, Figure 2.3a-c. Samples were deformed to a specific strain, and then the crosshead direction was reversed until the applied force returned to 0N. Samples were immediately deformed to a larger strain and the crosshead reversed again. This cyclic loading and unloading was repeated until the samples failed. The cyclic deformation stress-strain curves are compared with the

standard tensile test behavior re-plotted from Figure 2.1 in Figure 2.3a-c as a grey line. The semi-crystalline sample, p21AA, deforms almost entirely plastically with an elastic component matching the initial yield point, Figure 2.3a. The Young's modulus decreases slightly after every cycle likely due to the loss of crystallinity, because lamellae are destroyed by tensile deformation.[52] At the onset of each cycle, the sample undergoes a new yield point with excellent agreement in yield stress with the continually deformed sample. The amorphous samples, p15AA and p9AA, show similar behavior between the cyclic tensile curves and the standard uniaxial deformation curve including capturing the strain-hardening phenomenon, Figure 2.3b and 3c. Unlike the semi-crystalline sample however the new yield stress at each cycle is noticeably lower than the standard tensile curve indicating relaxation of the structure. This mechanism cannot be attributed to changes in the crystallinity and therefore, is indicative of other microstructural changes such as chain disentanglement and acid groups exchanging between aggregates.

The amorphous samples also exhibit substantial deformation recovery with a very large elastic component. Figure 2.3d compares the applied strain to the residual strain when the sample is unloaded (0N tensile force). When 100% of the applied strain persists as residual strain the slope of the plot will be unity and the sample is perfectly plastic. The semi-crystalline sample, p21AA, exhibits highly plastic behavior as the lamellae deform with a 10% elastic component defined by the x-intercept (Figure 2.3d inset). The material with the next highest plastic component is p9AA, while p15AA is the most elastic. For p9AA the nine carbons between acid groups have limited ability to rearrange without disrupting the acid aggregates, thus tensile strain produces substantial permanent deformation through chain disentanglement and acid aggregates that readily break and reform. The higher elastic recovery of p15AA originates from the fifteen carbons between

acid groups having more accessible conformations that are better able to extend while keeping the acid aggregates intact and thereby limiting chain disentanglement. Thus, the precise acrylic acid copolymer with intermediate acid content exhibits the highest amount of elastic deformation, because p15AA is amorphous and the alkyl spacer can assume extended conformation with less acid aggregate destruction and this provides restoring forces that promote elastic deformation. In contrast, the crystalline lamellae in p21AA are prone to plastic deformation and the short alkyl spacers in p9AA induce acid exchange between facile aggregates.

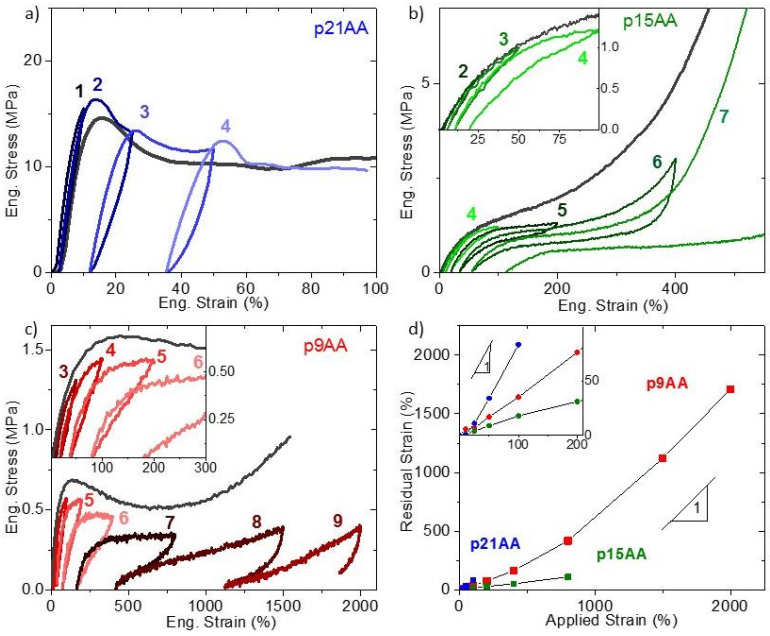

Figure 2.3. Cyclic tensile results from sequentially deforming a sample to a set strain at $\dot{\varepsilon}$=0.17s^{-1}, returning to a 0N force at $\dot{\varepsilon}$= -0.17s^{-1}, then deforming to a larger strain with the cycle number shown next to the data on the plot. For comparison the tensile data (gray) are re-plotted from Figure 1. a) p21AA. b) p15AA. c) p9AA. d) The plot of the applied strain vs residual strain when the sample is returned to 0N load.

Overview of Morphology Evolution. An overview of the 2D X-ray scattering patterns at specified strains is shown in Figure 2.4 and illustrates a variety of structural evolutions during deformation at $\dot{\varepsilon} = 0.17 s^{-1}$. At 0% strain all samples have isotropic scattering patterns indicating no preferred structural alignment. The LLDPE sample, which loosely represents the linear PE backbone without acid groups, reproduces the characteristic PE deformation from literature.[53-55] At large q (8-18nm^{-1}) there is the amorphous halo and two orthorhombic crystalline peaks, [110] and [200]. During yielding there is fine slip within the PE lamellae leading to the martensitic transformation observed as a “4-point pattern” and the appearance of the monoclinic [001] peak at a scattering angle smaller than the [110] orthorhombic peak. At high strain, many of the backbone chains align in the deformation direction and the 4-points converge into a 2-point pattern at the equator corresponding to the backbone-backbone scattering of highly aligned PE chains.

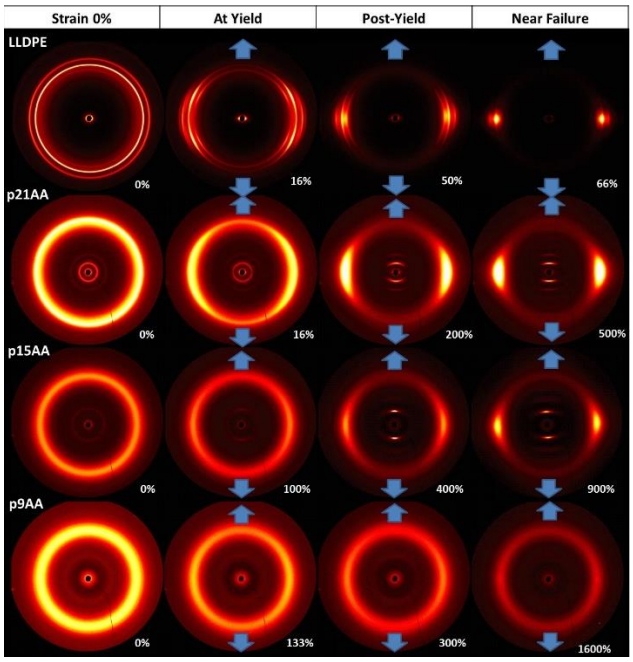

Figure 2.4. *In situ* 2D X-ray scattering data from four polymers (rows) undergoing tensile deformation $\dot{\varepsilon}$=0.17s^{-1}. Columns correspond to the initial state, at yield, post-yield and near failure and the strains are specified in each image. The blue arrows indicate the tensile draw direction. A linear color scale is used for direct comparison between all images.

Each of the acrylic acid copolymers exhibits a distinct morphology evolution with tensile strain: reorientation of the layered morphology in p21AA, transformation of the liquid-like morphology to a layered morphology in p15AA, and persistence of the liquid-like morphology in p9AA. In addition, uniaxial deformation aligns the polymer chains in the direction of strain, although the extent of chain orientation decreases substantially with the increasing acrylic acid content. These three types of structural evolutions are presented schematically in Figure **2.5** and will be discussed separately and in more detail below.

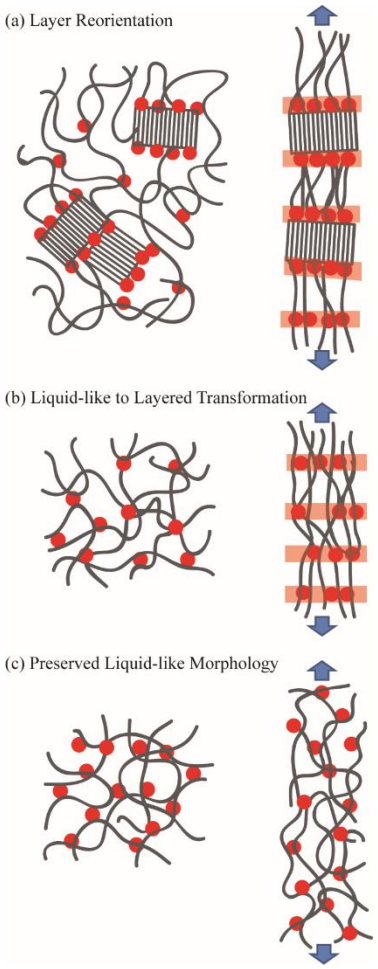

Figure 2.5. a) Schematic of the preexisting layered acid aggregate morphology reorienting and aligning during deformation in p21AA. b) Liquid-like aggregate morphology of p15AA transforming through aggregates breaking and reforming into a layered aggregate morphology. There is significant chain alignment and the aggregate spacing d^* increases indicating chain extension. c) Liquid-like aggregate morphology is preserved with amorphous chains weakly aligning and little chain extension. No change in the aggregate morphology or inter-aggregate distance d^* is observed. The red circles indicate acid aggregates.

To explore the morphology evolution evident in the 2D X-ray scattering images as a function of deformation, the scattering intensities as a function of q are plotted against tensile strain, Figure 2.6. From the 2D data, I(q) was extracted by averaging over the azimuthal angle from -15° to +15° relative to the direction parallel (top row in Figure 2.6) and perpendicular (bottom row) to the tensile deformation. Color indicates the scattering intensity. At 0% strain all samples are isotropic and have identical I(q) profiles in the parallel and perpendicular directions. Again, consider LLDPE (Figure 2.6 a and b) with the backbone-backbone correlations of the broad amorphous halo at q=8-18nm^{-1} and two strong peaks corresponding to orthorhombic PE, namely [110] and [200] peaks at q=15.4nm^{-1} and 16.6nm^{-1}, respectively.[54, 55] Along the deformation direction (Figure 2.6a) the amorphous halo and crystalline peak intensities decrease during deformation and eventually approaches background scattering intensity (black), while perpendicular to the deformation direction (Figure 2.6b) these amorphous halo and crystalline peaks persist. (Note that we have not corrected for sample thinning during deformation. This results in decreasing overall scattering intensity with strain.) In addition, the monoclinic [001] peak (q=13.6nm^{-1}) appears at intermediate strains (~10-40%) as a consequence of fine slip in the lamellae near yield, also referred to as the martensitic transformation in orthorhombic PE.[14, 54, 56, 57]. Finally, LLDPE shows no scattering features at q~2-10nm^{-1} where the acid aggregate scattering occurs in the precise acid copolymers. Below q~2nm^{-1} lamellae-lamellae scattering intensity is observed. Figure **2.6**a and b are consistent with the reorientation of the orthorhombic crystals to have the chain axis along the strain direction in LLDPE.

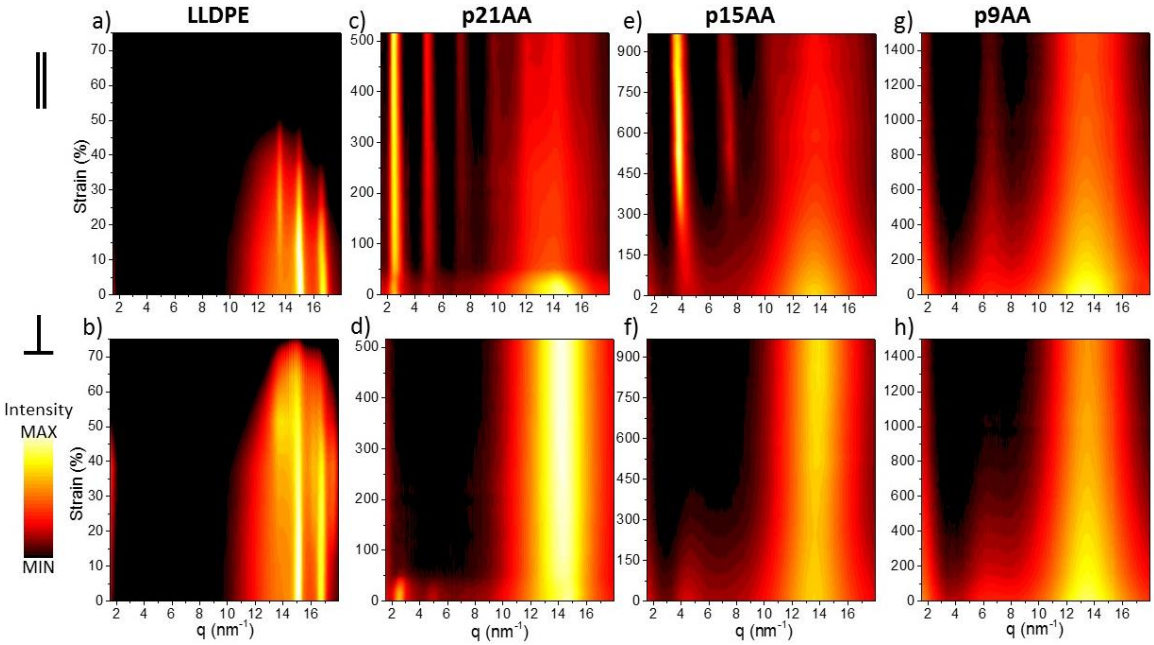

Figure 2.6. The scattering intensities as a function of *q* and strain are plotted for X-ray scattering parallel to deformation in the top row (a,c,e,g) and perpendicular to deformation in the bottom row (b,d,f,h). The I(q) data is averaged over +/-15 degrees from the specified direction. Scattering intensity units are arbitrary with color scale ranges as follows: LLDPE (300-20,000), p21AA (600-14,000), p15AA (1,100-50,000), and p9AA (600-14,000). The strain rate was $\dot{\varepsilon}$=0.17s^{-1}.

Reorientation of the Layered Morphology. The semi-crystalline p21AA has a layered morphology initially and during tensile deformation these layers align perpendicular to the strain, shown schematically Figure 2.5a and in I(q,ε) Figure 2.6c and d. The undeformed p21AA copolymer has an amorphous halo (q=12-16nm^{-1}) and a weakly scattering crystalline reflection at a q-value similar to the [110] peak in orthorhombic PE. This finding is consistent with the decreased crystalline content of this material.[18] At low q-values isotropic peaks (q=2.4nm^{-1}, 4.8nm^{-1}) from inter-aggregate scattering appear

where no features were present in LLDPE.[16, 20, 21, 25] As reported previously this layered morphology has acid-rich, layered lamellae separated by 2.5nm, which is consistent with an all-*trans* conformation of 21 carbons.[21] In the parallel direction (Figure 2.6c), this layered morphology exists before and throughout deformation, indicating the layered morphology aligns in the draw direction. Significant reorientation of the acid peak coincides with strains at the yield point (ε~50%) as evidenced by the disappearance of the low *q* peaks perpendicular to strain (Figure 2.6d). The d-spacing of the acid peak is largely unchanged during reorientation and grows in intensity along the parallel direction with higher degrees of alignment, most evident in the increasing intensity of the second order peak at q = 4.8nm^{-1}, despite the thinning sample. The amorphous halo and crystalline reflections along the parallel direction, however, consistently decrease in intensity during strain as a result of the reorientation of the backbone chains along the deformation direction. Perpendicular to deformation (Figure 2.6d) there is strong scattering at all strains from both the amorphous halo and crystalline peaks indicating chain alignment in the direction of deformation. To establish if the morphology was transient an *in situ* stress relaxation experiment was conducted on p21AA, which was deformed to ~ 600% strain, and held for 16 minutes. There was a significant reduction in the applied stress without a change in the aligned layered morphology. These X-ray scattering data establish that the layered morphology in semi-crystalline p21AA evolves continuously as the acid layers and polymer chains align perpendicular and parallel to deformation, respectively.

Unlike LLDPE, p21AA does not exhibit a 4-point pattern or evidence for fine slip in the lamella in Figure 2.4 or Figure 2.6. Azimuthal integrations of the 2D scattering patterns also fail to detect fine slip. This may be due to the relatively low crystalline content in p21AA or that fine slip is absent in these lamellae which incorporate layers of acid groups.

In either case, at high strains the backbone scattering results in an X-ray peak perpendicular to the deformation direction reminiscent of PE. The acid aggregate peaks at low *q* in p21AA align in the deformation direction, as reported previously after deforming at elevated temperature and cooling to room temperature under strain.[18, 21] The *in situ* X-ray experiments reveal the simultaneous reorganization of the acid peak with the amorphous halo that suggests lamellae are reorienting instead of melting.

Transformation from Liquid-like Morphology to Layered Morphology. The p15AA copolymer at 0% strain has a liquid-like distribution of acid aggregates but evolves into a layered structure during deformation. The liquid-like distribution of acid aggregates is evidenced by the single acid aggregate peak with no higher order reflections, lack of crystalline reflections at high *q*, and the lack of a melting peak in DSC.[18] In the parallel direction there is a shift in the acid peak position from q=0.44nm^{-1} to q=0.37nm^{-1} during deformation (Figure **2.6**e). Near 300% strain, coinciding with the strain hardening observed in tensile tests, the acid peak intensity dramatically increases and higher order reflections appear corresponding to a q/q^* ratio of 1:2:3 consistent with a layered morphology.

The scattering perpendicular to deformation (Figure 2.6f) confirms the gradual loss of acid aggregate ordering until ~400% strain where there is no detectable ordering. If the acid aggregates remain intact it is expected the scattering would exhibit affine-type deformation where elongation in one dimension leads to a contraction in the other two dimensions. The lack of change in q-position or peak breadth of the acid peak and instead the loss of scattering intensity, suggest acid aggregates are breaking apart during the applied deformation and morphology transformation from a liquid-like morphology to a layered morphology. The amorphous halo becomes anisotropic during deformation

indicating polymer chains align along the direction of applied strain, although there is no evidence of polymer crystallization.

When *in situ* X-ray scattering was performed at a higher strain rate, the morphology transformation from liquid-like to layered morphology in p15AA was more pronounced. After 400% strain at 0.63 s^{-1}, the amorphous halo shows more chain alignment, the first and second order acid aggregate peaks are stronger and more oriented, and the third order peak is more distinct. As shown in Figure 2.2, the onset of strain hardening occurs at lower strains for higher strain rates. Thus, the greater orientation found at 400% strain and a faster strain rate is consistent with the morphology transformation from liquid-like to layers corresponding to the onset of strain hardening.

An *in situ* stress relaxation experiment showed that after p15AA was deformed to ~ 600% strain and held for 16 minutes the applied stress necessary to maintain the 600% strain decreased substantially, but there was no significant change in the polymer chain alignment or the aligned layered morphology. This indicates that the anisotropic morphology in p15AA persists as long as the strain is applied. Given the high strains and well-ordered acid aggregate peaks in X-ray scattering, the development of strain induced crystallization (SIC) was considered in p15AA. In an *ex situ* experiment p15AA was deformed into the strain hardened regime (700% strain) and held at constant strain until the stress relaxed and became time independent (approximately 40 m). When the sample was released it recovered significant amounts of deformation. Segments of the gauge length were collected and placed in a differential scanning calorimetry (DSC) pan and tested for crystallinity within 5 m, where no crystallinity was detected. Based on 1) large

deformation recovery upon the release of stress and 2) no detectable DSC crystallinity or phase transitions, it was concluded that strain induced crystallinity did not occur in p15AA.

Figure **2.5**b shows the liquid-like packing of acid aggregates within an amorphous polymer matrix. During deformation the polymer chains disentangle and the acid aggregates begin to break apart, and reform as the backbones slide past one another. For every acid group participating in an aggregate, there is a series of acid groups with equal spacing along the oriented backbone, which generates the layered morphology indicated by q/q^* = 1:2:3. This structural transformation coincides with the onset of strain hardening at ε^* when the chains are oriented and the acid groups in layers begin to cooperatively resist disentanglement. This is the first experimental evidence for a layered acid morphology in an amorphous precise copolymer and has not been reported in our previous *ex situ* X-ray scattering experiments. In both p21AA and p15AA at $0.17s^{-1}$, the formation of an oriented layered morphology correlates with the onset of strain hardening at ~ 50% and ~ 300%, respectively. A key difference between the layered morphology present in p21AA and p15AA scattering patterns is that the layered structure of p21AA exists before deformation whereas p15AA develops the layered scattering pattern during deformation.

Persistence of the Liquid-like Morphology. The liquid-like morphology of p9AA remains unchanged with elongation at $\dot{\varepsilon}=0.17s^{-1}$, as seen in Figure 2.6g and h. The acid peak width and position are largely unchanged with deformation and simply weaken as the tensile specimen thins. Furthermore, no higher order acid peak reflections appear during strain and the highest scattering intensity is from the amorphous halo. While some alignment of the amorphous PE chains occurs during deformation resulting in a preferred alignment of the acid aggregates there is no evidence of a morphology change.

Specifically, the acid aggregate peak indicative of the liquid-like morphology persists up to ~700% strain perpendicular to deformation and up to 1500% strain parallel to deformation. At this strain rate the strain hardening is marginal and deformation continues with a small engineering tensile stress even at strains as high as 1500%.

Figure 2.5c illustrates that for the highest acid content (smallest spacer length) polymer, the liquid-like arrangement of acid aggregates persists under tensile deformation at room temperature. For the high strains applied here this requires the acid aggregates to break and reform. At deformation rates slower than the relaxation timescale of the acid aggregates ($0.17s^{-1}$, Figure 2.4 and Figure 2.6), the acid aggregates break and reform quickly enough to dissipate the stress and the liquid-like morphology is maintained. These findings suggest that acid aggregates are facile and can break and reform while chains disentangle to dissipate the stress during deformation as previously reported in polymers with H-bonding groups.[47, 49-51] Furthermore, the acid aggregate breaking and reconstitution mechanism found in p9AA will also occur in p15AA and p21AA, because the copolymers share the same acrylic-acid H-bonding strength. The primary difference appears to originate from the acid content, where p9AA has the highest acid content and the smallest separation between acid aggregates. Consequently, the acid aggregates in p9AA more easily reconfigure with applied strain and this results in substantially weaker mechanical properties and minimal morphology evolution.

Further Analysis. The interaggregate scattering peak q^* corresponds to a center-to-center distance between the acid aggregates[22, 24, 25], $d^* = 2\pi / q^*$. Figure 2.7shows the normalized interaggregate spacing, d^*_{norm}, which is d^* divided by the length of an all-*trans* alkane chain of 9, 15, or 21 carbons assuming a 120° bond angle and 0.154nm bond length. Normalizing d^* in this way highlights how close the alkyl segments are to the fully

extended conformation.[16] Consistent with being semi-crystalline, p21AA has the highest d^*_{norm}, which increases from ~ 0.89 prior to strain to ~ 0.92 just prior to fracture at ~ 500% strain. We attribute the 8% discrepancy between the length of an all-*trans* conformation and the observed interlayer spacing in p21AA as being the result of gauche conformations near the acid group. If on the other hand the PE chain segments were all-*trans* and tilted relative to the acid layers, then at high strains when the chains are highly aligned (~ 500% strain) four interaggregate scattering peaks would be expected at ± 23° relative to the strain direction. In contrast, two interaggregate peaks are observed throughout the deformation, which further establishes that the acid layers are perpendicular to the PE chain segments and that the chain conformations are not tilted relative to the PE. Further work is underway to determine the detailed chain conformations that allow the acid layers to be accommodated in p21AA and other semi-crystalline precise copolymers. The liquid-like morphology of p9AA has a lower d^*_{norm} of ~ 0.81 which is nearly independent of applied strain, which is consistent with the persistence of the original liquid-like morphology of compact isolated aggregates. At zero strain p15AA has the smallest d^*_{norm} of ~ 0.70, which suggests that the 15-carbon alkyl spacers is short enough to prevent crystallization and long enough to accommodate the acid aggregates with less distortion of the chain conformation than p9AA. Sample p15AA also exhibits the largest change in d^*_{norm} increasing to ~ 0.85, which is consistent with the transformation of a liquid-like morphology or a layered morphology with significant chain alignment.

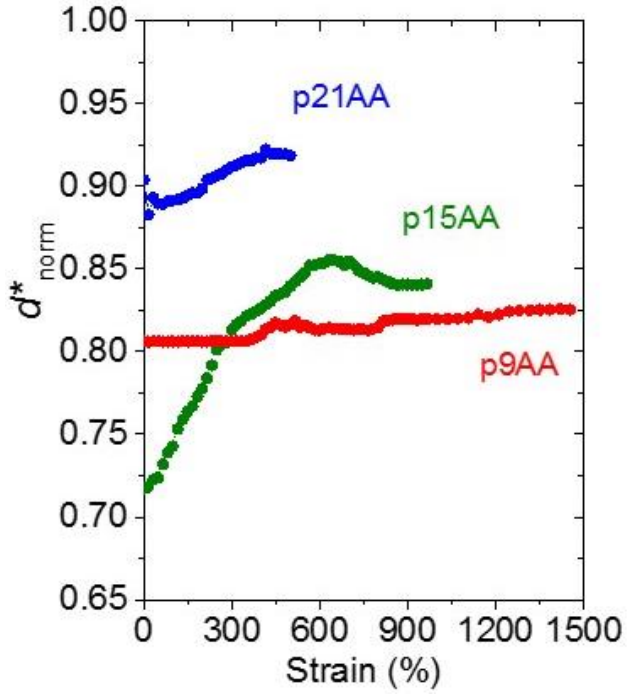

Figure 2.7. The normalized interaggregate distance, d^*_{norm}, for p9AA, p15AA and p21AA as a function of strain. The value of 1.0 indicates that the distance between acid aggregates is identical to an all-*trans* alkyl chain of 9, 15, or 21 carbons.

As is evident from Figure 2.4, the scattering from both the acid aggregate morphologies and the polymer chains becomes anisotropic with strain. The Herman's orientation parameter (f_2) quantifies how the orientation evolves with strain by analyzing the scattering intensity (I) as a function of the azumthal angle (ø), Figure **2.8**.[58] The samples were confirmed to have fiber symmetry where the layered morphology in the in-

plane direction was the same as the through-plane direction of the film. Thus, the appropriate form for the Herman's parameter is

$$f_2 = \frac{3\langle \cos^2 \emptyset \rangle - 1}{2} \tag{1}$$

$$\text{where } \langle \cos^2 \emptyset \rangle_{hkl} = \frac{\int_0^{\frac{\pi}{2}} I(\emptyset) \cos^2 \emptyset \, \sin \emptyset \, d\emptyset}{\int_0^{\frac{\pi}{2}} I(\emptyset) \, \sin \emptyset \, d\emptyset} \tag{2}$$

All the acrylic acid copolymers are uncorrelated (f_2=0) before deformation, when ε=0%. During deformation, the acid peak becomes correlated with the deformation direction (f_2 > 0) while the amorphous halo is anti-correlated (f_2 < 0), Figure 2.4c-h. Figure 2.8 shows that sample p21AA has the strongest correlations in both the interaggregate scattering peak and the amorphous halo (closed and open symbols, respectively). Both Herman's order parameters change abruptly at the onset of strain hardening as the layered morphology in p21AA reorients. In contrast, the order parameters for p9AA change smoothly and remain weak (-0.05< f_2<0.05) even at 900% strain, which is consistent with the persistence of the liquid-like morphology and just a slight alignment. Sample p15AA shows intermediate order parameters and interestingly a maximum in the orientation

parameter for the interaggregate scattering near 450%, somewhat above the onset of strain hardening, while f_2 for the amorphous halo decreases monotonically.

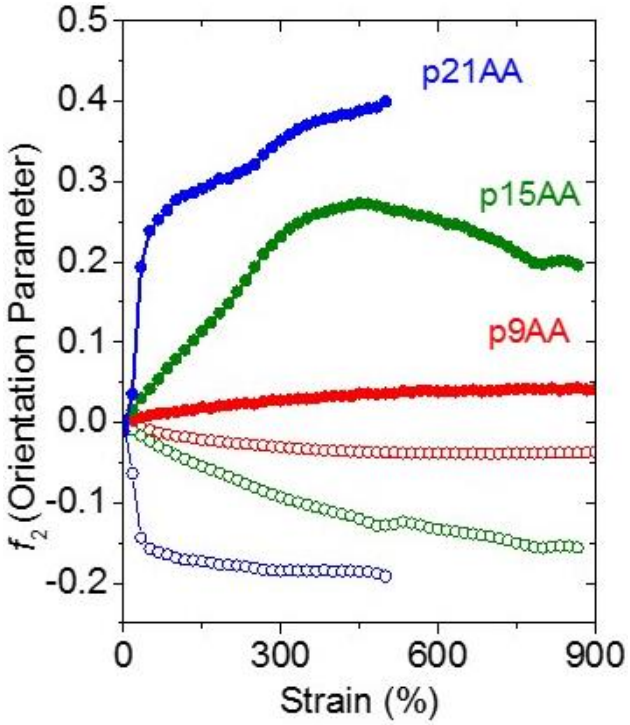

Figure 2.8. Herman's orientation parameter (f_2) for the interaggregate scattering peak (solid points) and the amorphous halo (open points) of the acid copolymers. The acid peak was integrated as follows: p9AA q = 5.3-7.2 nm^{-1}, p15AA q = 3.9-4.6 nm^{-1}, and p21AA q = 2.2-2.8 nm^{-1}. The amorphous halo was integrated across q = 12.9-14.5 nm^{-1}; note that the crystalline peak intensity is outside the range selected for the amorphous halo.

Conclusions

We report the first tensile testing characterization of precise acid copolymers along with *in situ* X-ray scattering. The acrylic acid groups are pendant to linear polyethylene chains and separated by exactly 9, 15, or 21 carbons. This spacer length dictates the bulk

mechanical properties, initial morphology and morphology evolution during deformation. The relatively weak H-bonding between the acid groups allows the acid aggregates to be destroyed and reconstituted during tensile deformation, where the relative time scale of the chain and aggregate relaxations influences the extent of structural orientation.

The acid copolymer with the longest spacer (p21AA) is semi-crystalline with the acid groups arranged in layers perpendicular to the PE spacers and this structure progressively aligns during elongation such that the layers are perpendicular to the stress. Relative to LLDPE or strictly linear PE (pPE), p21AA exhibits pronounced strain hardening which corresponds to the onset of significant orientation of the polymer chains along the direction of applied stress and the layer perpendicular to deformation. The reversible nature of the H-bonding within the acid layers facilitates the ongoing deformation by allowing polymers to dissociate with their neighbors, move relatively small distances (~ 2.5nm) and reform the acid layers that act to reinforce the polymer. In p21AA the crystallinity of the PE segments slows the chain relaxations and leads to significant structural orientation.

Strain-hardening is also evident in p15AA and correlates to the transformation of the acid aggregates from nominally spherical aggregates with liquid-like ordering to layers aligned perpendicular to the applied stress. While p21AA is semi-crystalline before and during deformation, the shorter PE-spacer in p15AA prevents crystallization and the significant chain extension associated with constructing acid layers provides a strong restoring force that returns p15AA to its initial morphology when the stress is unloaded. The onset of strain hardening and the corresponding structural changes in p15AA are particularly sensitive to the strain rate (0.016 to 0.83s^{-1}), because the relaxation times of the PE segments and the acid aggregates are accessible.

Finally, although p9AA has the highest concentration of acid groups, this copolymer has mechanical properties reminiscent of an elastomer and only a modest amount of structural orientation. The maximum strain in p9AA is ~ 1300% with an engineering stress at break of ~ 1MPa and the *in situ* X-ray scattering shows an invariant interaggregate scattering peak corresponding to 1.01nm. Reconciling both this larger deformation and the absence of structural evolution requires that the compact, isolated acid aggregates are being destroyed and reconstituted during tensile deformation. This requires that single acid groups or perhaps acid dimers are dislodged from an aggregate and move into another nearby aggregate. The high acid content p9AA copolymers with short chain segments between the acid groups leads to lower modulus and yield strain and inhibits morphology evolution by frequent exchange of the acid groups between aggregates.

This study of mechanical properties and morphology evolution of precise acid copolymers lays the foundation for investigating precise acid copolymer with some of the acid groups neutralized with metal cations, namely precise ionomers. Neutralization is expected to transform the facile acid aggregates to ionic aggregates that are more resistant to deformation. Furthermore, precise copolymers having functional groups with stronger secondary bonding could also be used to explore the importance of facile aggregates for both mechanical properties and morphology evolution.

References

1. Adi Eisenberg, J.-S. K., *Introduction to Ionomers*. 1st ed.; Wiley: New York, 1998; p 326.

2. Quiram, D. J.; Register, R. A.; Ryan, A. J. *Macromolecules* **1998,** 31, (4), 1432-1435.

3. Aitken, B. S.; Buitrago, C. F.; Heffley, J. D.; Lee, M.; Gibson, H. W.; Winey, K. I.; Wagener, K. B. *Macromolecules* **2012,** 45, (2), 681-687.

4. Alamo, R. G.; Jeon, K.; Smith, R. L.; Boz, E.; Wagener, K. B.; Bockstaller, M. R. *Macromolecules* **2008,** 41, (19), 7141-7151.

5. Boz, E.; Wagener, K. B.; Ghosal, A.; Fu, R.; Alamo, R. G. *Macromolecules* **2006,** 39, (13), 4437-4447.

6. Few, C. S.; Wagener, K. B.; Thompson, D. L. *Macromol Rapid Commun* **2014,** 35, (2), 123-32.

7. Opper, K. L.; Markova, D.; Klapper, M.; Müllen, K.; Wagener, K. B. *Macromolecules* **2010,** 43, (8), 3690-3698.

8. Hosoda, S.; Nozue, Y.; Kawashima, Y.; Suita, K.; Seno, S.; Nagamatsu, T.; Wagener, K. B.; Inci, B.; Zuluaga, F.; Rojas, G.; Leonard, J. K. *Macromolecules* **2011,** 44, (2), 313-319.

9. Deschanel, S.; Greviskes, B. P.; Bertoldi, K.; Sarva, S. S.; Chen, W.; Samuels, S. L.; Cohen, R. E.; Boyce, M. C. *Polymer* **2009,** 50, (1), 227-235.

10. Hong, K.; Rastogi, A.; Strobl, G. *Macromolecules* **2004,** 37, (26), 10165-10173.

11. Scogna, R. C.; Register, R. A. *Polymer* **2008,** 49, (4), 992-998.

12. Scogna, R. C.; Register, R. A. *Polymer* **2009,** 50, (2), 585-590.

13. Shan, G.-F.; Yang, W.; Yang, M.-B.; Xie, B.-H.; Fu, Q.; Mai, Y.-W. *Journal of Macromolecular Science, Part B* **2009,** 48, (4), 799-811.

14. Na, B.; Zhang, Q.; Fu, Q.; Men, Y.; Hong, K.; Strobl, G. *Macromolecules* **2006,** 39, (7), 2584-2591.

15. Wagener, K. B.; Boncella, J. M.; Nel, J. G. *Macromolecules* **1991,** 24, (10), 2649-2657.

16. Baughman, T. W.; Chan, C. D.; Winey, K. I.; Wagener, K. B. *Macromolecules* **2007,** 40, (18), 6564-6571.

17. Alam, T. M.; Jenkins, J. E.; Bolintineanu, D. S.; Stevens, M. J.; Frischknecht, A. L.; Buitrago, C. F.; Winey, K. I.; Opper, K. L.; Wagener, K. B. *Materials* **2012,** 5, (12), 1508-1527.

18. Buitrago, C. F.; Jenkins, J. E.; Opper, K. L.; Aitken, B. S.; Wagener, K. B.; Alam, T. M.; Winey, K. I. *Macromolecules* **2013,** 46, (22), 9003-9012.

19. Jenkins, J. E.; Seitz, M. E.; Buitrago, C. F.; Winey, K. I.; Opper, K. L.; Baughman, T. W.; Wagener, K. B.; Alam, T. M. *Polymer* **2012,** 53, (18), 3917-3927.

20. Buitrago, C. F.; Alam, T. M.; Opper, K. L.; Aitken, B. S.; Wagener, K. B.; Winey, K. I. *Macromolecules* **2013,** 46, (22), 8995-9002.

21. Seitz, M. E.; Chan, C. D.; Opper, K. L.; Baughman, T. W.; Wagener, K. B.; Winey, K. I. *Journal of the American Chemical Society* **2010,** 132, (23), 8165-8174.

22. Buitrago, C. F.; Bolintineanu, D. S.; Seitz, M. E.; Opper, K. L.; Wagener, K. B.; Stevens, M. J.; Frischknecht, A. L.; Winey, K. I. *Macromolecules* **2015,** 48, (4), 1210-1220.

23. Lueth, C. A.; Bolintineanu, D. S.; Stevens, M. J.; Frischknecht, A. L. *The Journal of Chemical Physics* **2014,** 140, (5), 054902.

24. Hall, L. M.; Seitz, M. E.; Winey, K. I.; Opper, K. L.; Wagener, K. B.; Stevens, M. J.; Frischknecht, A. L. *Journal of the American Chemical Society* **2012,** 134, (1), 574-87.

25. Hall, L. M.; Stevens, M. J.; Frischknecht, A. L. *Physical Review Letters* **2011,** 106, (12), 127801.

26. Todd, M. A.; Janelle, E. J.; Michelle, E. S.; Buitrago, C. F.; Karen, I. W.; Kathleen, L. O.; Travis, W. B.; Kenneth, B. W., H1 MAS NMR Spectroscopy of Polyethylene Acrylic Acid Copolymers and Ionomers. In *NMR Spectroscopy of*

Polymers: Innovative Strategies for Complex Macromolecules, American Chemical Society: 2011; Vol. 1077, pp 115-131.

27. Bolintineanu, D. S.; Stevens, M. J.; Frischknecht, A. L. *ACS Macro Letters* **2013,** 2, (3), 206-210.

28. Hall, L. M.; Stevens, M. J.; Frischknecht, A. L. *Macromolecules* **2012,** 45, (19), 8097-8108.

29. Ting, C. L.; Stevens, M. J.; Frischknecht, A. L. *Macromolecules* **2015,** 48, (3), 809-818.

30. Choi, U. H.; Middleton, L. R.; Soccio, M.; Buitrago, C. F.; Aitken, B. S.; Masser, H.; Wagener, K. B.; Winey, K. I.; Runt, J. *Macromolecules* **2015,** 48, (2), 410-420.

31. Heiney, P. *Commission on Powder Diffraction Newsletter* **2005**, (32), 9-11.

32. Bolintineanu, D. S.; Stevens, M. J.; Frischknecht, A. L. *Macromolecules* **2013,** 46, (13), 5381-5392.

33. O'Gara, J. E.; Wagener, K. B.; Hahn, S. F. *Die Makromolekulare Chemie, Rapid Communications* **1993,** 14, (10), 657-662.

34. Frischknecht, A. L.; Todd, M. A.; Azoulay, J.; Bolintineanu, D. S.; Cordaro, J. G.; Hall, L. M.; Jenkins, J. E.; Lueth, C. A.; Murtagh, D.; Rempe, S. L. B.; Stevens, M. J. *Effects of Morphology on Ion Transport in Ionomers for Energy Storage*; SAND2012-8304; Sandia National Laboratories: Sandia Rerport, 2012.

35. Rojas, G.; Wagener, K. B. *Macromolecules* **2009,** 42, (6), 1934-1947.

36. Kennedy, M. A.; Peacock, A. J.; Failla, M. D.; Lucas, J. C.; Mandelkern, L. *Macromolecules* **1995,** 28, (5), 1407-1421.

37. Kennedy, M. A.; Peacock, A. J.; Mandelkern, L. *Macromolecules* **1994,** 27, (19), 5297-5310.

38. Scogna, R. C.; Register, R. A. *Journal of Polymer Science Part B: Polymer Physics* **2009,** 47, (16), 1588-1598.

39. Wakabayashi, K.; Register, R. A. *Polymer* **2005,** 46, (20), 8838-8845.

40. Landel, R. F.; Nielsen, L. E., *Mechanical properties of polymers and composites*. 2 ed.; CRC Press: 1993.

41. Young, R. J.; Lovell, P. A., *Introduction to polymers*. 3 ed.; CRC press: 2011.

42. Choi, T.; Fragiadakis, D.; Roland, C. M.; Runt, J. *Macromolecules* **2012,** 45, (8), 3581-3589.

43. Toki, S.; Che, J.; Rong, L.; Hsiao, B. S.; Amnuaypornsri, S.; Nimpaiboon, A.; Sakdapipanich, J. *Macromolecules* **2013,** 46, (13), 5238-5248.

44. Tierney, N. K.; Register, R. A. *Macromolecules* **2002,** 35, (16), 6284-6290.

45. Tierney, N. K.; Register, R. A. *Macromolecules* **2002,** 35, (6), 2358-2364.

46. Colby, R. H.; Zheng, X.; Rafailovich, M. H.; Sokolov, J.; Peiffer, D. G.; Schwarz, S. A.; Strzhemechny, Y.; Nguyen, D. *Physical Review Letters* **1998,** 81, (18), 3876-3879.

47. Leibler, L.; Rubinstein, M.; Colby, R. H. *Macromolecules* **1991,** 24, (16), 4701-4707.

48. Semenov, A. N.; Rubinstein, M. *Macromolecules* **2002,** 35, (12), 4821-4837.

49. Yamauchi, K.; Lizotte, J. R.; Long, T. E. *Macromolecules* **2003,** 36, (4), 1083-1088.

50. Lewis, C. L.; Stewart, K.; Anthamatten, M. *Macromolecules* **2014,** 47, (2), 729-740.

51. Neal, J. A.; Mozhdehi, D.; Guan, Z. *Journal of the American Chemical Society* **2015,** 137, (14), 4846-4850.

52. Ayoub, G.; Zaïri, F.; Naït-Abdelaziz, M.; Gloaguen, J. M. *International Journal of Plasticity* **2010,** 26, (3), 329-347.

53. Butler, M. F.; Donald, A. M.; Bras, W.; Mant, G. R.; Derbyshire, G. E.; Ryan, A. J. *Macromolecules* **1995,** 28, (19), 6383-6393.

54. Butler, M. F.; Donald, A. M.; Ryan, A. J. *Polymer* **1997,** 38, (22), 5521-5538.

55. Butler, M. F.; Donald, A. M.; Ryan, A. J. *Polymer* **1998,** 39, (1), 39-52.

56. Addiego, F.; Dahoun, A.; G'Sell, C.; Hiver, J.-M. *Polymer* **2006,** 47, (12), 4387-4399.

57. Che, J.; Locker, C. R.; Lee, S.; Rutledge, G. C.; Hsiao, B. S.; Tsou, A. H. *Macromolecules* **2013,** 46, (13), 5279-5289.

58. Wilchinsky, Z. W. *Journal of Applied Physics* **1960,** 31, (11), 1969-1972.

CHAPTER 3

Role of Acid Chemistry and Periodicity on the Morphological Evolution and Strength in Precise Polyethylenes

Introduction

The equilibrium morphologies and morphological evolutions of polymers under deformation has direct impact on their tensile properties. Individual polymer chains can exhibit extraordinarily high strengths approaching that of the covalent bonds within the polymer[1, 2], while bulk polymers exhibit much lower mechanical performance due to alternative deformation mechanisms such as bond rotation and chain displacement.[3, 4] As such, the mechanisms of tensile deformation in bulk polymers, both semi-crystalline and amorphous, has been extensively studied.[5, 6] The most ubiquitous polymer studied, polyethylene (PE), is known to deform in both crystalline and amorphous regions[7-10], which under specific conditions lead to the formation of highly oriented shish-kebab morphologies and coincide with substantial improvement in the mechanical properties.[11, 12] Another mechanism for strengthening polymers is the addition of associating groups that enable intrachain secondary bonding and resist chain displacement. Common examples include polyamides such as Nylon® and para-aramid fibers, such as Kevlar®.

The addition of hydrogen bonding functional groups to semi-crystalline PE introduces significant complexity associated with the interrelated factors of composition, thermal characteristics, and hierarchical morphologies. The incorporation of a minor fraction of hydrogen bonding acid groups enhances mechanical performance and tunable properties resulting in commercially important polyethylenes such as Escor® and Nucrel®.[13] The H-bonding groups, or upon neutralization the ionic groups, are thermoreversible crosslinks that improve mechanical properties. Extensive studies of

polyethylene-based acid-containing random copolymers and their ionomers have been performed on inherently complex materials synthesized by free radical methods and have highly branched architectures and semi-crystalline morphologies.[13-21] Studies of morphological evolution during deformation have primarily focused on the PE crystal structures or the neutralized, ionomer forms instead of acid copolymers due to a lack of a low-*q* acid aggregate-aggregate peak. Detailed analyses of systems that do exhibit a low-*q* ionomer peak remains complex due to the breadth of the ionomer peak, indicating a broad distribution of aggregate-aggregate distances and ambiguous aggregate morphologies.

A set of model PE-based acid polymers, so-called *precise* acid polyethylenes, have provided insight into these complex systems. The well-controlled and uniform chain architecture achieved by acyclic diene metathesis (ADMET) can be described as a polymer with a fixed number of carbons between each pendant acid group along a strictly linear PE backbone.[22-25] The morphologies of these model polymers with periodic acid groups along the backbone have been studied extensively at room temperature and at elevated temperature considering the effect of acid type and acid content/spacer length, as well as the effect of neutralization with metal ions.[22-24, 26-31] Experimental and simulation investigations of these materials provide novel insights into the morphologies and the local dynamics of the polymers and ions.[32-35] Specifically, for the acrylic acid systems there is excellent agreement between measured and calculated X-ray scattering profiles from coarse-grained and atomistic molecular dynamics simlations.[36, 37]

In 2015 the first mechanical property study of these precise acid-functionalized polyethylenes reported strain-induced morphologies that correspond to strain hardening.[38] X-ray scattering was collected simultaneously to tensile deformation such that changes in mechanical properties were directly related to changes in morphology. The three precise

acid-functionalized polyethylenes (p*x*AA) were investigated, where *x* is the number of backbone carbons between pendant acrylic acid groups along the polyethylene chain (*x* = 9, 15, 21). The spacer length *x* has a profound impact on both the tensile properties and the morphological evolution at room temperature. When the interchain H-bonding was sufficiently long-lived, an anisotropic hierarchical morphology of layered acids formed and substantially enhanced tensile strength. Two routes to forming the layered morphology were identified. One case is in semi-crystalline p21AA that prior to elongation has acid-rich layers oriented isotopically due the crystallization of the alkyl segments.[28] The acid-rich layered morphology strongly aligns under deformation wherein acid layers comprise H-bonds and orient perpendicular to the strain direction. Secondly, the amorphous p15AA polymer exhibits a structural transformation from a liquid-like distribution of compact, isolated acid aggregates into a layered aggregate morphology during tensile deformation, coinciding with substantial strain hardening. The structural changes in p15AA are particularly sensitive to the strain rate, due to the relaxation times of the PE segments and acid aggregates. In contrast, p9AA withstands strains of >1000% as the shorter spacers enable the liquid-like assembly of acid aggregates to exchange acid groups without developing substantial anisotropy in the structure.

The ability to form anisotropic hierarchical acid layers that lead to strain hardening and the factors necessary to create nanoscale, layered morphologies are the focus of this paper. What polymer characteristics dictate when a nanoscale layered morphology forms? More broadly, when do supramolecular hydrogen-bonded networks form and enhance properties in self-healing polymers and stimuli-responsive polymers, as well as biomaterials? The simple and systematic changes of the chemical structures in these functional polyethylenes provide an opportunity to directly measure the effect of 1) periodic versus non-periodic placement of pendant acid groups along a polymer, 2) the pendant

acid chemistry, and 3) the mole fraction of acid groups on the morphological evolution and mechanical properties during room temperature tensile deformation.

Experimental Section

Materials. The synthesis methods and room temperature morphologies of precise and pseudo-random functionalized polyethylene with acrylic acid[22, 38] and phosphonic acid[24] were reported previously. For the precise polyethylenes (periodic) a symmetric diene was synthesized with a protected acid group, these macromonomers were polymerized using acyclic diene metathesis (ADMET), and then the double bonds were hydrogenated and the acid groups deprotected. For the pseudo-random polyethylenes (non-periodic) a ring opening polymerization (ROMP) was used to create polymers with irregularly distributed pendant groups along a linear backbone and acid concentrations equal to the precise polymers.[22] Both ADMET and ROMP produce linear polymers. The sample notation signifies precise vs pseudo-random acid placement (p21AA vs r21AA), the precise or average number of backbone carbons between pendant acid groups along the polyethylene chain (x = 9, 15, 21), and acid type (acrylic acid (AA), phosphonic acid (PA) and geminal acrylic acid (gAA)).

Table **3.1** indicates the sample compositions, thermal transitions and molecular weight information.

Table 3.1. Polymer Nomenclature, Composition, Thermal Characterization (DSC), and Molecular Characterization (GPC) of the polymers studied.

Name	Acid Content (mol%)	T_g C°	T_m C° (Enthalpy of melting J/g)	Ref	M_n (kg/mol)	PDI (M_w/M_n)	Ref
p21AA	9.5%	13	46.0 (ΔH_m=60.5)	[38]	18.3	1.9	[38]
r21AA	9.5%	11	86.0 (ΔH_m=106.1)		85.4	1.4	[22]
p21PA	9.5%		47.4, 63.0 (ΔH_m=45)	[28]	17.9	1.9	[24, 28]
r21PA	9.5%		53, 79 (ΔH_m=39.6)		24.2	1.6	[39]
p21gAA	19%		46.1 (ΔH_m=38.8)	[28]	21.0	1.8	[22, 28]
p15AA	13.3%	3	-	[38]	62.7	1.8	[38]
p15PA	13.3%	46	-	[28]	23.6	1.7	[24]
p9AA	22.2%	7	-	[38]	41.5	1.9	[38]

Sample Preparation. Samples were prepared for both X-ray scattering characterization and tensile testing with the same procedure. Films were melt-pressed in a Carver 4122 hot press at 130°C, which is above the T_g and T_m, for 20 min. The films are

then rapidly cooled to room temperature (~15°C/min) through a heat exchanger with circulating tap water. The tensile samples were then punched from the films into dogbone or smaller rectangular geometries. The dogbone shaped die with length of 25mm and lateral dimensions of 10mm x 0.13mm was based on the sample dimension ratios in ASTM Microtensile Specimens Standard (D1708 – 10). The second sample geometry is a rectangle (10mm x 3mm x 0.13mm) to fit within the Linkham TST350 tensile system. All films were aged a minimum of 3 days in an evacuated desiccator at room temperature before conducting experiments.

In situ X-ray Scattering and Tensile Testing. *In situ* synchrotron X-ray scattering was conducted at beamline 5ID-D (DND-CAT) of the Advanced Photon Source (APS) at Argonne National Laboratory. Improvements to this beamline were made over the course of the study. Room temperature tensile tests were conducted on an Instron model 8500 Materials Testing System, as well as the Linkam TST350 Tensile System. The Instron 8500 system has dual servo-hydraulic drive and the Linkam TST350 uses lead screws that drive the grips in opposite directions to maintain the sample center in the X-ray beam. For the semi-crystalline samples, that exhibit necking, scattering data was collected from within the necked region either by shifting the Instron and sample vertically to position the necked region in the beam path, or by adding a small notch in the sample gage length of samples loaded into the Linkam to initiate necking near the incident beam. Engineering stress-strain values were calculated based on the initial dimensions of the sample and the force-displacement measurements from the tensile instruments.

Simultaneously with sample deformation, two-dimensional X-ray scattering data was collected. Two detector configurations were used. First, a single MAR-CCD detector used a sample-to-detector distance of 0.32 m and the X-ray energy was 17 keV (λ=0.73Å). This experimental setup provides X-ray scattering information with a *q*-range of 1.54-

17.98nm^{-1} to capture information from length scales of d = 0.3-6.5 nm. Exposure times of 1 s were used to obtain both sufficient counting statistics and adequate time resolution to accurately determine the structural evolution during continuous deformation. Additionally, a 6 s delay between exposures was necessary to refresh the detector. The second detector configuration used three MAR-CCD detectors with sample-to-detector distances of 0.2m, 0.14m and 8.5m to provide overlapping q-ranges. The X-ray energy was 17 keV (λ=0.73Å) and the full q-range was 0.0256-34.4nm^{-1} corresponding to length scales of d = 0.18-245nm. Exposure times were 1 s with a 3.5 s delay between exposures. In both detector configurations silver behenate, lanthanum hexaboride, and amorphous carbon were used to calibrate the scattering angle and normalize detector counts, respectively. The scattering signals were corrected for beam intensity fluctuations, dark counts and Kapton window background scattering. Two-dimensional data reduction and analysis were performed using the Datasqueeze software.[40]

Ex situ X-ray scattering. X-ray scattering was also performed in the multi-angle X-ray scattering (MAXS) facility at the University of Pennsylvania using a Nonius FR591 rotating-anode generator operated at 40 kV and 85 mA. A bright, highly collimated beam was obtained via Osmic Max-Flux optics and triple pinhole collimation under vacuum. The scattering data were collected for 30 min using a Bruker Hi-Star multiwire two-dimensional detector at a sample-to-detector distance of 11 cm. Two-dimensional data reduction and analysis of data were performed using the Datasqueeze software.[40]

Results and Discussion

Figure 3.1(A-E) shows an overview of the 2D X-ray scattering patterns for the five acid-functionalized polyethylenes spacer length 21: p21AA, r21AA, p21PA, r21PA and p21gAA. The scattering patterns are shown at select strains (columns) that coincide with

the *in situ* tensile deformation curves shown in Figure 3.2(A-C). In the undeformed state, the first column or ε=0%, all samples are isotropic (intensity is independent of azimuthal angle) demonstrating that there is no preferential orientation of the samples prior to deformation. Upon tensile deformation in the vertical direction, indicated by blue arrows in Figure 3.1, a variety of aligned morphologies form with direct effect on the tensile properties. The continuous morphological evolution in the parallel and perpendicular directions relative to deformation are extracted from the 2D X-ray scattering data. The *I* vs *q* data along the meridian and the equator, corresponding to the structure in the parallel and perpendicular directions relative to deformation, are plotted as a function of strain (Figure 3.3). It can be noted that at ε=0%, the parallel and perpendicular scattering are identical because the morphology is initially isotropic.

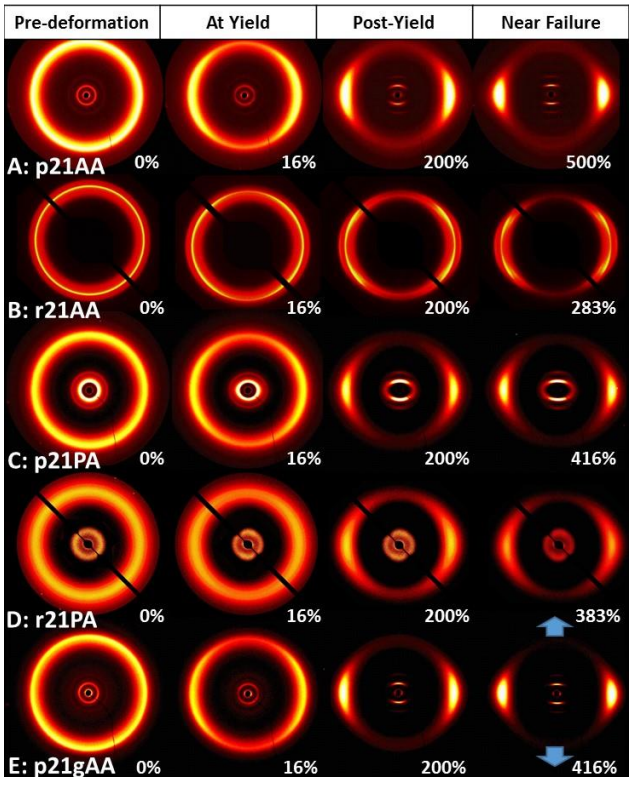

Figure 3.1. *In situ* 2D X-ray scattering overview for the five acid-containing polyethylenes with precisely or on average 21 carbons between acids (rows A-E). The tensile

deformation is applied at $\dot{\varepsilon} = 1.7\ s^{-1}$. Columns correspond to initial state, at yield, post-yield and near failure and the strains are specified in each image. The tensile deformation direction in all images is along the vertical axis as indicated by the blue arrows. The intensity is adjusted for clarity in each image.

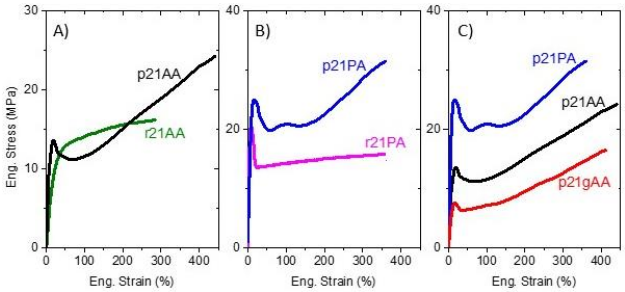

Figure 3.2. In situ engineering stress–strain tensile data for five acid-containing polymers (*x*=21) undergoing deformation at a strain rate of $\dot{\varepsilon} = 1.7\ s^{-1}$.

The effect of precise vs. pseudo-random acid placement will be examined in acrylic acid polymers (p21AA vs r21AA) and then phosphonic acid polymers (p21PA vs r21PA). Additionally, the effect of geminal acid substitution, effectively doubling the acid content, is examined (p21AA vs p21gAA). Finally, the morphology evolution of amorphous precise polyethylenes (p15AA, p15PA and p9AA) will be presented.

Effect of Acid Periodicity in Equimolar Acrylic Acid Polymers (p21AA vs r21AA). The tensile mechanical properties and the morphology evolution are distinct for p21AA and r21AA. In p21AA the deformation is dominated by lamellae fragmentation and reorientation that lead to substantial strain hardening.[38] The r21AA sample exhibits lamellae slip, fragmentation and reorientation typical of unfunctionalized PE.[8-10, 41, 42]

The initial morphologies of p21AA and r21AA are different as measured with X-ray scattering, demonstrating that the placement of acid groups impacts polymer morphology. Starting with the p21AA sample at 0% strain (Figure 3.1A), several isotropic features are

observed at different *q* positions. In agreement with previous studies[22, 28] at low-*q* there is a primary peak (q^*=2.5nm^{-1}) corresponding to acid-acid scattering. There are also higher order reflections of this primary peak at a ratio of q/q^*=1:2:3 indicating a layered morphology. The isotropic scattering indicates that these layers are oriented in all directions prior to deformation. At higher *q* a broad amorphous halo (*q*=12-16nm^{-1}) overlaps with a weak crystalline reflection consistent with a PE orthorhombic [110] reflection, see also Figure 3.4A. These features indicate that p21AA is semi-crystalline where some of the methylene spacers between pendant acid groups crystallize and the precisely spaced acid groups assemble into hierarchical layers. This semi-crystalline morphology is consistent with earlier DSC and NMR results.[22, 28] We cannot conclusively identify the difference between a semi-crystalline polymer with small crystallites in an amorphous matrix from the coexistence of smectic liquid crystalline domains within an amorphous polymer. Both morphologies exhibit melting endotherms in DSC, a SAXS peak, layered acid peaks in IAXS, and crystalline scattering in WAXS.

The morphological evolution during deformation (Figure 3.1 top row) clearly highlights that p21AA forms a highly anisotropic, layered morphology. Figure 3.3A highlights the primary and higher order acid peak positions, where at high strains the primary acid peak, *q*=2.5nm^{-1}/*d*=2.5nm, approaches the all-*trans* length of 21 carbons (*d*=2.66nm). This indicates a mostly extended conformation of the PE backbone between the acid groups, which is consistent with the semi-crystalline structure coexisting with layered morphology. During deformation the higher order reflections increase in intensity in the parallel direction (Figure 3.3A) with only a slight change in the q^* demonstrating an increase in the structural alignment along the deformation direction. In the perpendicular direction, Figure 3.3F, the low-*q* peaks fade while the scattering of the amorphous halo increases indicating backbone alignment along the fiber axis. These data are consistent

with the reorientation of a layered structure, particularly at the onset of strain hardening (~50% strain).

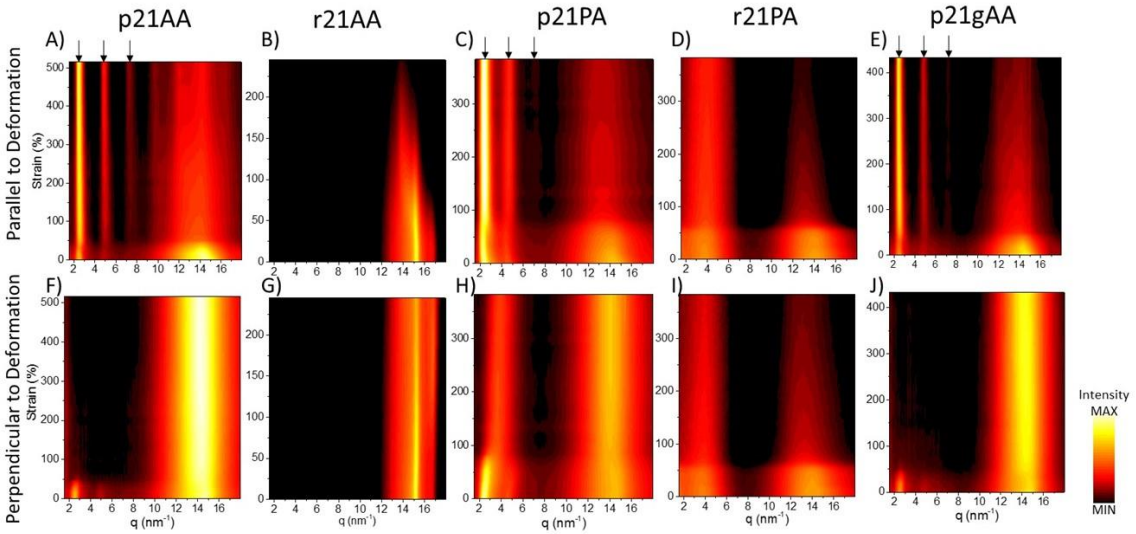

Figure 3.3. X-ray scattering intensities as a function of *q* and strain are plotted for X-ray scattering parallel to deformation in the top row and perpendicular to deformation in the bottom row. The *I(q)* data is averaged over ±15 degrees from the specified direction. Scattering intensity units are arbitrary counts with the color black equivalent to background. Arrows indicate multiple reflections (*q*/q* of 1:2:3), corresponding to layered morphologies.

In contrast r21AA is a semi-crystalline polymer with non-periodic pendant acid groups and fails to exhibit an acid-acid correlation peak at low-*q*, Figure 3.1B, 3B, and 3G. The amorphous halo and crystalline reflection are present at high *q* and the crystalline reflection in r21AA is better defined with higher peak intensity and narrower peak breadth than the precise p21AA, Figure 3.4B. The better defined crystalline peaks are consistent with DSC results indicating both a higher T_m and percent crystallinity in r21AA,

Table 3.1. The difference in the X-ray scattering between two compositionally equivalent polymers (p21AA and r21AA) highlights the impact of acid precision on the initial

morphology.[30] A strongly scattering acid peak with higher order reflections in p21AA and the lack of an acid peak in r21AA indicate a very different distribution of acid groups at the nanoscale between these two polymers, schematically represented in Figure 3.5, left. The precise p21AA polymer exhibits substantial ordering of the H-bonded acid groups forming hierarchical layers at the expense of less perfect or smaller PE lamellae, as seen by weaker and broader crystalline scattering, Figure 3.4A. In contrast, the r21AA has no acid-acid scattering peak and sharper PE crystalline scattering at high *q* (Figure 3.4B), similar to highly branched and low acid content commercial materials.[14] The precise chemical structure with regular acid groups along the backbone forces the AA groups to be evenly distributed throughout the matrix, whereas the r21AA polymer has some longer PE segments that produce larger and more perfect crystallites.

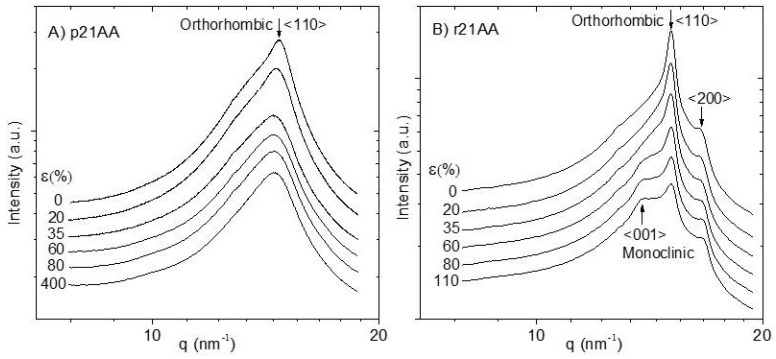

Figure 3.4. Comparison of wide angle X-ray scattering intensities (*I* vs *q*) integrated over all azimuthal angles for p21AA and r21AA. Strains specified in figure. The curves are shifted vertically for clarity.

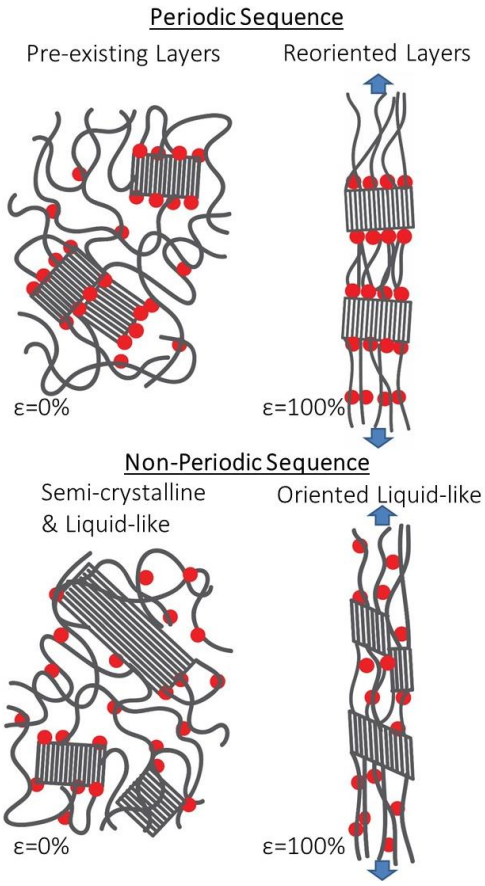

Figure 3.5. Schematics of the structural evolution for polyethylenes with periodic and non-periodic acid placement. Red dots represent acid aggregates. Periodic acid placement produces layered acid aggregate morphologies that reorient and align during deformation in precise polymers. Pseudo-random polymers have liquid-like distribution of aggregates and large crystallites. During deformation r21AA exhibits fine slip within the PE lamellae.

The implications of acid distribution and PE crystallite perfection on deformation are evident from the *in situ* experiments. A schematic representing the structural evolution is shown for the periodic and non-periodic case in Figure 3.5. The pseudo-random r21AA polymer which is identical in molar acid composition to p21AA, shows the quintessential fine slip transformation of the PE lamellae, Figure 3.1B. Upon yielding r21AA exhibits the monoclinic [001] peak at lower *q* than the [110] orthorhombic peak, Figure 3.4B. At higher

strain, many of the backbone chains align in the deformation direction and the 4-point pattern evolves toward a two-point pattern corresponding to the backbone–backbone scattering of highly aligned PE chains.[8-10, 43] This type of deformation has also been reported for random, highly branched PE-based acid polymers (2.1-7.1 mol% acid).[14-17] In contrast, p21AA shows no evidence of monoclinic structure during deformation, Figure 3.4A. Both precise and pseudo-random polymer backbones align in the deformation direction, although, the p21AA deformation mechanism is dominated by the reinforced lamellae and acid layers, whereas r21AA exhibits lamellae fine slip, fragmentation and reorientation typical of pure PE.

The impact of acid periodicity on mechanical properties is evident in Figure 3.2A: p21AA exhibits yielding, necking, and significant strain hardening while r21AA simply yields and only modestly strain hardens. With engineering stress-strain data the strain hardening slopes cannot be compared, nevertheless, we can conclude that the strain hardening slope from ε=50%-300% is substantially higher in p21AA indicating that the aligned layered morphology improves polymer strength. The absence of necking in r21AA is consistent with deformation seen in other non-precise acid-containing polyethylenes, particularly at low strain rates or elevated temperatures.[14] Molecular weight influences strain hardening due to entanglements and tie molecules,[5, 6, 12, 44] but p21AA has a lower M_w (18.3kg/mol) and still displays enhanced stain hardening relative to r21AA (85.4kg/mol). Furthermore, these polymers are identical in composition and therefore have the same number of H-bonding constituents. Therefore, the difference in mechanical properties apparently arises from the ability of precise polymers to form acid-rich layers. Above the yield point, the highly anisotropic morphology in p21AA possess layers of H-bonded acids adjacent to the crystallites that provide reinforcement. This mechanism for strengthening the lamellae is absent in r21AA because the acid aggregates are not

correlated to the PE crystallites. The precise, semi-crystalline polymer, p21AA, suggests a new strategy for strengthening semi-crystalline polymers by reinforcing the lamellae crystallites with layers of secondary bonding. Unlike nylons that incorporate the functional group into the crystallite, here we demonstrate that the functional groups need only be spatially correlated to the crystals.

The Effect of Acid Placement in Equimolar Phosphonic Acid Polymers (p21PA vs r21PA). This section examines another set of equimolar acid-containing polyethylenes with precise and pseudo-random acid periodicity, but now considering phosphonic acid. The effect of acid group periodicity in polyethylene is similar for the AA and PA chemistries. In comparison to acrylic acid, phosphonic acid has the ability to hydrogen bond with 3 rather than 2 acid groups, is a stronger acid (pK_a=2 vs 5 in AA), and is a larger side group (acid volume fraction ~16% vs ~10%).[27] Note that the electron density is higher for PO_3H_2 than COOH, such that the low-*q* peaks have higher intensity in p21PA than p21AA. Nonetheless, undeformed p21PA has a morphology similar to p21AA: semi-crystalline with acid-rich layers, Figure 3.1C.[23, 24, 28] In r21PA no acid-rich layer morphology was observed in 2D X-ray scattering (Figure 3.1D) although a single, broad peak at q=3.8nm^{-1} indicates a broad distribution in length scales between acid-rich aggregates. The presence of an acid peak in r21PA, whereas r21AA does not, is simply attributed to the greater electron density contrast between the acid group types.

Upon deformation p21PA exhibits a morphological evolution (Figures 1C, 3C, 3H) similar to p21AA, highlighting that the precision in acid group placement plays a key role on the morphology evolution. Specifically, p21PA develops an anisotropic acid-rich layered morphology. Interestingly, upon tensile deformation an elliptical shape in the PA acid peak is observed prior to necking, Figure 3.1C ε=16%. The acid peak moves to slightly lower *q* in parallel direction to deformation (Figure 3.3C) and to slightly higher *q* in

the perpendicular direction (Figure 3.3H), consistent with affine deformation indicating that acid aggregates are long lived. Substantial reorientation of the morphology occurs just after necking, most visible in the perpendicular direction, Figure 3.3H, where the layered morphology disappears at ε~75%. After necking a broad peak centered at q=3.8nm^{-1} remains along the perpendicular direction with a correlation distance (1.65nm) that is smaller than the acid layer spacing evident along the parallel direction (2.59nm). This low-angle, broad peak is evidence of PA aggregates in the amorphous microdomains. The persistence of this low-angle peak in PA materials and its absence in the AA materials is likely due to the enhanced electron density contrast of the PA groups. This low-q peak perpendicular to deformation also exists in r21PA (Figure 3.3I) and p15PA (Figure 3.8E). For these reasons it was concluded that p21PA evolves from an isotropic layered morphology to an oriented layered morphology.

The X-ray scattering of r21PA indicates that backbones align, but the acid aggregate morphology maintains a liquid-like acid-aggregate morphology, Figure 3.1D. The single, broad acid peak at low q scatters strongly in both parallel and perpendicular directions throughout deformation (Figure 3.3D, 3I). While in p21AA and p21PA higher order reflections appear in the parallel direction, the r21PA shows only a single acid-acid correlation distance that remains at a constant q^* during deformation indicating no layered or hierarchical morphology (Figure 3.3D). In the perpendicular direction the acid peak shifts slightly to higher q^*, indicating a contraction of the acid group spacing in the perpendicular direction, Figure 3.3E. Consistent with the alignment of polymer backbone under tensile deformation the amorphous halo aligns toward the equator and decreases in intensity suggesting an orientated liquid-like morphology in r21PA at high strains.

As seen in Figure 3.2B, semi-crystalline p21PA with a hierarchical layered morphology exhibits enhanced strain hardening relative to semi-crystalline r21PA, in

which acid groups assemble into aggregates with liquid-like order. This precision-induced enhancement of strain hardening is more apparent in the PA polymers than AA polymers. This might be unexpected because the difference between the M_w and T_m between the precise and pseudo-random polymers is greater in the AA than the PA polymers. The key attribute for enhanced strain hardening is the location of acid groups along the polymer. Precise placement produces the hierarchical layered morphology with interchain H-bonding networks in spatial registry with the polyethylene crystallites and thereby cooperatively resist deformation.

The Effect of Precise Geminal Acid Substitution (p21AA vs p21gAA). Both p21AA and the geminal form, p21gAA, contain acrylic acid groups precisely every 21 carbons along a linear PE backbone. Although the geminal form has two pendant acid groups instead of one, therefore doubling the acid content from 9.5 mol% to 19 mol%, the initial morphology of p21gAA is very similar to p21AA exhibiting an isotopic layered morphology. Perhaps more surprising is that p21AA and p21gAA have nearly identical morphology evolution as acid-rich layers reorient and polymer chains align in the deformation direction, Figure 3.1A and 1E. The morphological evolution parallel to deformation (Figure 3.3E) clearly highlights that p21gAA forms a layered morphology (black arrows) with the primary acid peak at q=2.48nm^{-1} corresponding to d=2.53nm. During deformation the peak position is nominally constant as the higher order reflections increase in intensity along the parallel direction. This is consistent with the reorientation of the layered structures during tensile deformation, as discussed above for the other precise polyethylenes, p21AA and p21PA.

The tensile behavior of the three semi-crystalline precise polymers with layered morphologies (p21AA, p21PA, and p21gAA) show similarly significant strain hardening, Figure 3.2C. These polymers have comparable molecular weights and PDIs, and different

volume fractions of acid (acid volume fractions ~10%, ~16%, ~18%, respectively).[27] These precise polyethylenes exhibit similar yield strain and strain hardening slopes after necking when the oriented layered morphology develops. p21PA displays the highest mechanical strength likely due to the stronger hydrogen bonds of phosphonic acid relative to acrylic acid and the amorphous component likely has a higher T_g. The second highest tensile strength is the p21AA polymer, which has a similar T_m to p21gAA, but higher percent crystallinity.[22, 28] Moreover, the p21AA has better defined layered morphology in X-ray scattering as seen by narrower scattering peaks and a greater number of measurable higher order reflections. These attributes are consistent with p21AA having improved mechanical properties relative to p21gAA.

Overall, relating the mechanical properties with morphological evolution, the semi-crystalline precise polyethylenes with 21-carbon spacers form layered morphologies and orient upon deformation. This morphological transformation correlates with significant strain hardening. Contrarily, the pseudo-random acid polymers (r21AA and r21PA) fail to form anisotropic layered structures during deformation and correspondingly exhibit less strain hardening.

Amorphous Polymers with Initially Liquid-like Acid Aggregate Morphologies. When PE spacers are shorter than 21 carbons these acid-containing polyethylenes are amorphous. The 2D X-ray scattering data for p15AA, p15PA and p9AA are presented in Figure 3.6A-C. The scattering patterns are shown at select strains (columns) that coincide with regions of interest in the tensile deformation curves, Figure 3.7. In the undeformed state, ε=0%, the 2D X-ray scattering for p15AA, p15PA and p9AA indicate amorphous morphologies with liquid-like distributions of acid aggregates.[28] These morphologies persist at elevated temperature (150°C)[27], and comparisons with atomistic molecular dynamics of p15AA and p9AA at 150°C demonstrate that these polymers have discrete,

isolated acid aggregates.[36] Simulations of a precise sulfonic acid polyethylene (p21SA) and p21AA[32] also displays isolated acid aggregate morphologies. Therefore it is expected that at room temperature p15AA, p15PA and p9AA possess discrete isolated acid aggregates prior to deformation.

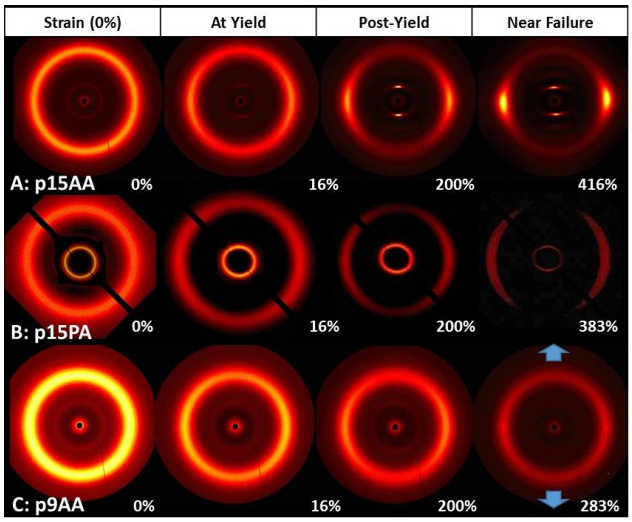

Figure 3.6. *In situ* 2D X-ray scattering overview for three amorphous, precise polymers (p15AA, p15PA and p9AA) undergoing tensile deformation at $\dot{\varepsilon}$ = 1.7 s^{-1}. Columns correspond to initial state, at yield, post-yield and near failure and the strains are specified in each image. The tensile deformation direction in all images is along the vertical axis as indicated by the blue arrows. The intensity is adjusted for clarity in each image.

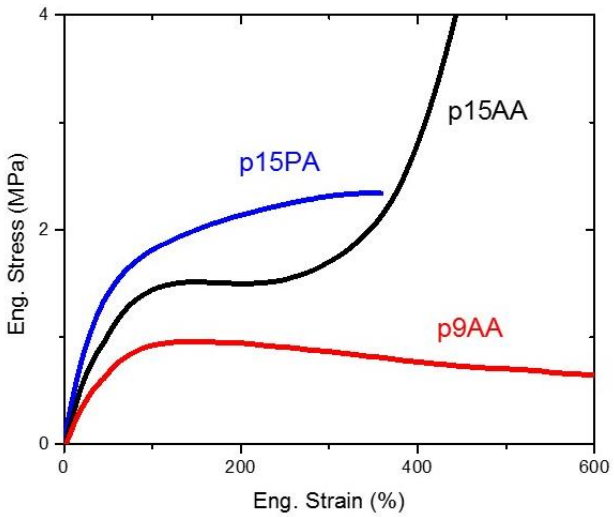

Figure 3.7. *In situ* engineering stress–strain data for three amorphous, precise polymers undergoing tensile deformation at a strain rate of $\dot{\varepsilon} = 1.7\ s^{-1}$.

Figure 3.6A, Figure 3.8A, and 8D show the liquid-like to layered morphology transformation of p15AA during tensile deformation. As was reported previously, the p15AA acid peak and amorphous halo align continuously during deformation until a layered morphology develops at ε~300%, which coincides with significant strain hardening (Figure 3.7).[38] There is a shift in the low-*q* peak to lower *q*, or larger real-space acid-acid distances, which approaches the all-*trans* distance of a 15-carbon segment. Additionally higher order reflections appear, black arrows in Figure 3.8A. The morphology evolution perpendicular to the deformation direction (Figure 3.8D) shows the acid peak shifting to slightly higher *q* and disappearing. This indicates the decreasing inter-acid distance and loss of acid group ordering in the direction perpendicular to deformation. The amorphous halo, at high *q*, increases in scattering along the perpendicular direction throughout elongation, confirming that the polymer backbones align in the deformation direction. In contrast to the structural reorientation in semi-crystalline p21AA, p21PA and p21gAA, the

morphological evolution of amorphous p15AA is a structural transformation from a liquid-like arrangement of nominally spherical acid aggregates to a layered morphology.

Another type of morphology evolution is evident in both p15PA and p9AA, which are initially amorphous polymers with nominally spherical aggregates with liquid-like order. As reported previously, p9AA maintains this liquid-like morphology to high strains (Figure 3.6C, Figure 3.8C, F).[38] The absence of the formation of a layered morphology is consistent with the absence of strain hardening (Figure 3.7). The facile nature of the acid aggregates during deformation of p9AA is evident in the sensitivity of the mechanical properties to strain rate and high strain-at-break (>1,000%).

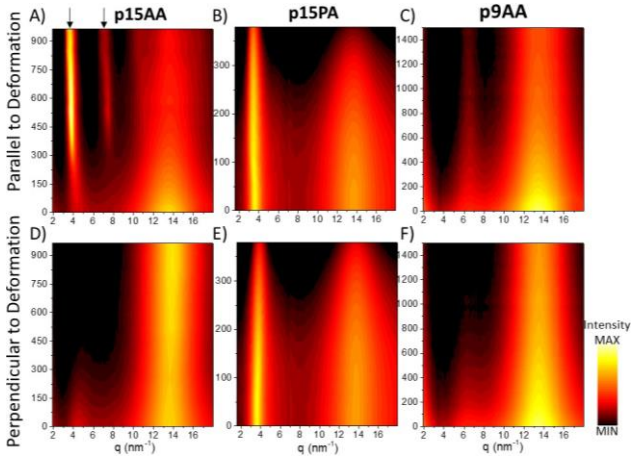

Figure 3.8. *In situ* X-ray scattering intensities as a function of *q* and strain are plotted for X-ray scattering parallel (top row) and perpendicular (bottom row) to deformation. The *I(q)* data is averaged over ±15 degrees from the specified direction. Scattering intensity units are arbitrary counts with the color black equivalent to background.

The higher electron density contrast afforded in p15PA provides additional insights as to how the liquid-like morphologies evolve during elongation. At 0% strain there is a liquid-like distribution of acid aggregates, similar to the amorphous acrylic acid polymer (p15AA, p9AA), although with stronger acid peak intensities (Figure 3.6, first column).

Upon deformation but prior to the yield point, p15PA shows an ellipse in the 2D X-ray scattering corresponding to affine deformation where inter-acid scattering distances increase in the deformation direction and contract in the normal direction, Figure 3.6B. After the yield point the low angle peak is only slightly stronger along the meridian than the equator (perpendicular to the elongation). As with p9AA, p15PA does not evolve into a layered morphology before failure at ~350% strain.

If the precision in acid placement along the polymer backbone enables the formation of the layered morphology, then why does p15PA maintain a liquid-like morphology? Recall that p15AA (T_g=3°C) forms AA layers during room temperature deformation when strain exceeded ~300%. However, p15PA (T_g=46°C) fails near 350% strain; notice the different strain scales in Figure 3.8A, 8B. The transformation from a liquid-like morphology to a layered morphology requires substantial chain mobility, namely deformation above T_g. Similarly, the importance of strain rate was previously reported in the precise acrylic acid polymers where faster deformation aligned and extended the conformation of chains during deformation, whereas slow deformation allowed chains to disentangle and relax through H-bond breaking.[38] To test whether p15PA forms layers above T_g, p15PA was heated ($T=T_g$+ ~5°C = ~50°C), stretched by hand (ε~500%) and immediately removed from the heat source to cool below T_g in air. The glassy sample morphology was examined by *ex situ* X-ray scattering, Figure 3.9. A narrower primary acid peak and a weak higher order peak (black triangles) suggest a layered morphology in p15PA when deformed above T_g. This confirms that p15PA can form layered morphologies under the correct conditions, namely, having sufficient chain mobility to orient chains at high strains, but not so much mobility that the chains can relax and disentangle faster than the applied deformation. This morphology evolution from liquid-like to layers is expected to correlate to substantial strain hardening in p15PA.

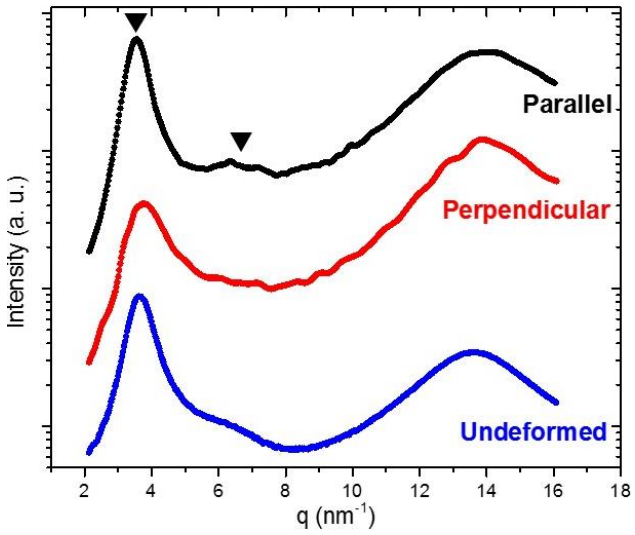

Figure 3.9. X-ray scattering integrated parallel (black) to the tensile deformation direction, perpendicular (red) to the deformation direction and full azimuthal integration of an undeformed sample (blue). These *ex situ* scattering data were collected at room temperature.

Conclusions

The morphology evolution during tensile deformation was investigated for various linear polyethylenes containing acid groups. The effect of pendant acid group periodicity (precise vs pseudo-random placement along the backbone), the effect of acid group chemistry, and the role of spacing between acid groups along the backbone (acid concentration) were examined. *In situ* X-ray scattering during room temperature tensile deformation captured the morphological evolution continuously from the initial isotropic state to failure.

Polymer backbone architecture is the primary factor that dictates the equilibrium morphology and the morphology evolution under deformation. Both regularity in acid group placement along the backbone (precision) and sufficiently long and mobile PE spacer between acid groups are required to form the anisotropic acid-rich layered morphologies

that are commensurate with strain hardening. Pseudo-random placement of the acid groups show aligned morphologies under deformation but without the hierarchical layers. The pendant acid chemistries (acrylic acid, phosphonic acid, and geminal acrylic acid) strongly modulate the thermal (T_g, T_m, percent crystallinity) and mechanical (E, σ_{max} , ε_{max}) properties.

The hierarchical acid-rich layered morphology forms by one of two routes. The first route occurs in p21AA, p21PA, and p21gAA and involves crystallization of the PE backbone and the simultaneous self-assembly of the acid groups into layers. These acid layers align during deformation. The second route involves initially liquid-like distribution of acid groups in amorphous polymers (p15AA and p15PA) transforming into layered morphologies. This route is exhibited in precise polymers with shorter carbon spacing between acid groups, because the frequent placement of bulky acid side groups frustrates chain packing and prevents crystallization. A sufficient temperature, tensile strain rate, and strain (~300% strain or greater) are required to strongly orient the backbone chains. Due to interchain H-bonding and the precise location of acid groups along polymers, acid-rich layered morphologies form. The formation of the layered acid morphology by either route coincides with significant tensile strain hardening because the aligned layered morphology cooperatively resists chain displacement. These layered structures require periodic placement of the associating groups.

This study indicates that H-bonded networks with layered morphologies form and dramatically enhance mechanical properties of polyethylene when the functional groups are periodic. The atactic H-bonding acid groups are unlikely to be incorporated into a crystalline structure, in contrast to the H-bonding amide groups in nylons. Nonetheless, these precise polyethylenes with layered morphologies have commensurate H-bonding sites between chains that enable the formation of a more uniform network and

cooperatively impede chain displacement. These findings encourage the pursuit of synthetic routes for polymers with periodic associating groups to enhance mechanical properties in performance polymers.

References

1. Isaacson, S. G.; Lionti, K.; Volksen, W.; Magbitang, T. P.; Matsuda, Y.; Dauskardt, R. H.; Dubois, G. *Nature materials* **2015,** advance online publication.

2. Hageman, J. C. L.; de Wijs, G. A.; de Groot, R. A.; Meier, R. J. *Macromolecules* **2000,** 33, (24), 9098-9108.

3. Prevorsek, D. C., Ultimate Properties, uniaxial systems. In *Encyclopedia of Polymer Science and Engineering*, Wiley: Ney York, 1989; pp 803-821.

4. Sawai, D.; Nagai, K.; Kubota, M.; Ohama, T.; Kanamoto, T. *Journal of Polymer Science Part B: Polymer Physics* **2006,** 44, (1), 153-161.

5. Young, R. J.; Lovell, P. A., *Introduction to polymers*. 3 ed.; CRC press: 2011.

6. Landel, R. F.; Nielsen, L. E., *Mechanical properties of polymers and composites*. 2 ed.; CRC Press: 1993.

7. Schrauwen, B. A. G.; Janssen, R. P. M.; Govaert, L. E.; Meijer, H. E. H. *Macromolecules* **2004,** 37, (16), 6069-6078.

8. Butler, M. F.; Donald, A. M.; Bras, W.; Mant, G. R.; Derbyshire, G. E.; Ryan, A. J. *Macromolecules* **1995,** 28, (19), 6383-6393.

9. Butler, M. F.; Donald, A. M.; Ryan, A. J. *Polymer* **1997,** 38, (22), 5521-5538.

10. Butler, M. F.; Donald, A. M.; Ryan, A. J. *Polymer* **1998,** 39, (1), 39-52.

11. Zhou, D.; Yang, S.-G.; Lei, J.; Hsiao, B. S.; Li, Z.-M. *Macromolecules* **2015**.

12. Kennedy, M. A.; Peacock, A. J.; Mandelkern, L. *Macromolecules* **1994,** 27, (19), 5297-5310.

13. Adi Eisenberg, J.-S. K., *Introduction to Ionomers*. 1st ed.; Wiley: New York, 1998; p 326.

14. Scogna, R. C.; Register, R. A. *Journal of Polymer Science Part B: Polymer Physics* **2009,** 47, (16), 1588-1598.

15. Scogna, R. C.; Register, R. A. *Polymer* **2009,** 50, (2), 585-590.

16. Wakabayashi, K.; Register, R. A. *Abstr. Pap. Am. Chem. Soc.* **2004,** 228, U446-U447.

17. Wakabayashi, K.; Register, R. A. *Polymer* **2005,** 46, (20), 8838-8845.

18. Lee, L.-B. W.; Register, R. A.; Dean, D. M. *Journal of Polymer Science Part B: Polymer Physics* **2005,** 43, (1), 97-106.

19. Scogna, R. C.; Register, R. A. *Polymer* **2008,** 49, (4), 992-998.

20. Tierney, N. K.; Register, R. A. *Macromolecules* **2002,** 35, (6), 2358-2364.

21. Vanhoorne, P.; Register, R. A. *Macromolecules* **1996,** 29, (2), 598-604.

22. Baughman, T. W.; Chan, C. D.; Winey, K. I.; Wagener, K. B. *Macromolecules* **2007,** 40, (18), 6564-6571.

23. Opper, K. L.; Fassbender, B.; Brunklaus, G.; Spiess, H. W.; Wagener, K. B. *Macromolecules* **2009,** 42, (13), 4407-4409.

24. Opper, K. L.; Markova, D.; Klapper, M.; Müllen, K.; Wagener, K. B. *Macromolecules* **2010,** 43, (8), 3690-3698.

25. Aitken, B. S.; Buitrago, C. F.; Heffley, J. D.; Lee, M.; Gibson, H. W.; Winey, K. I.; Wagener, K. B. *Macromolecules* **2012,** 45, (2), 681-687.

26. Alam, T. M.; Jenkins, J. E.; Bolintineanu, D. S.; Stevens, M. J.; Frischknecht, A. L.; Buitrago, C. F.; Winey, K. I.; Opper, K. L.; Wagener, K. B. *Materials* **2012,** 5, (12), 1508-1527.

27. Buitrago, C. F.; Alam, T. M.; Opper, K. L.; Aitken, B. S.; Wagener, K. B.; Winey, K. I. *Macromolecules* **2013,** 46, (22), 8995-9002.

28. Buitrago, C. F.; Jenkins, J. E.; Opper, K. L.; Aitken, B. S.; Wagener, K. B.; Alam, T. M.; Winey, K. I. *Macromolecules* **2013,** 46, (22), 9003-9012.

29. Jenkins, J. E.; Seitz, M. E.; Buitrago, C. F.; Winey, K. I.; Opper, K. L.; Baughman, T. W.; Wagener, K. B.; Alam, T. M. *Polymer* **2012,** 53, (18), 3917-3927.

30. Seitz, M. E.; Chan, C. D.; Opper, K. L.; Baughman, T. W.; Wagener, K. B.; Winey, K. I. *Journal of the American Chemical Society* **2010,** 132, (23), 8165-8174.

31. Todd, M. A.; Janelle, E. J.; Michelle, E. S.; Buitrago, C. F.; Karen, I. W.; Kathleen, L. O.; Travis, W. B.; Kenneth, B. W., H1 MAS NMR Spectroscopy of Polyethylene Acrylic Acid Copolymers and Ionomers. In *NMR Spectroscopy of Polymers: Innovative Strategies for Complex Macromolecules*, American Chemical Society: 2011; Vol. 1077, pp 115-131.

32. Lueth, C. A.; Bolintineanu, D. S.; Stevens, M. J.; Frischknecht, A. L. *J Chem Phys* **2014,** 140, (5), 054902.

33. Hall, L. M.; Seitz, M. E.; Winey, K. I.; Opper, K. L.; Wagener, K. B.; Stevens, M. J.; Frischknecht, A. L. *Journal of the American Chemical Society* **2012,** 134, (1), 574-87.

34. Hall, L. M.; Stevens, M. J.; Frischknecht, A. L. *Macromolecules* **2012,** 45, (19), 8097-8108.

35. Choi, U. H.; Middleton, L. R.; Soccio, M.; Buitrago, C. F.; Aitken, B. S.; Masser, H.; Wagener, K. B.; Winey, K. I.; Runt, J. *Macromolecules* **2015,** 48, (2), 410-420.

36. Buitrago, C. F.; Bolintineanu, D. S.; Seitz, M. E.; Opper, K. L.; Wagener, K. B.; Stevens, M. J.; Frischknecht, A. L.; Winey, K. I. *Macromolecules* **2015,** 48, (4), 1210-1220.

37. Hall, L. M.; Stevens, M. J.; Frischknecht, A. L. *Physical Review Letters* **2011,** 106, (12).

38. Middleton, L. R.; Szewczyk, S.; Azoulay, J.; Murtagh, D.; Rojas, G.; Wagener, K. B.; Cordaro, J.; Winey, K. I. *Macromolecules* **2015,** 48, (11), 3713-3724.

39. Opper, K. L. Polyethylene Functionalized with Highly Polar Groups. University of Florida, 2010.

40. Heiney, P. *Commission on Powder Diffraction Newsletter* **2005**, (32), 9-11.

41. Burger, C.; Hsiao, B. S.; Chu, B. *Polymer Reviews* **2010,** 50, (1), 91-111.

42. Che, J.; Locker, C. R.; Lee, S.; Rutledge, G. C.; Hsiao, B. S.; Tsou, A. H. *Macromolecules* **2013,** 46, (13), 5279-5289.

43. Addiego, F.; Dahoun, A.; G'Sell, C.; Hiver, J.-M. *Polymer* **2006,** 47, (12), 4387-4399.

44. Kennedy, M. A.; Peacock, A. J.; Failla, M. D.; Lucas, J. C.; Mandelkern, L. *Macromolecules* **1995,** 28, (5), 1407-1421.

CHAPTER 4

Deformation Induced Morphological Evolution of Precise Ionomers

INTRODUCTION

Neutralization of acid-functionalized polymers with metal ions causes nanoscale aggregation of the ionic and acid groups within the low dielectric polymer matrix. The aggregates behave as thermo-reversible crosslinks with tremendous impact on the bulk properties of the acid- and ion-containing polymers. For example viscosity in the melt state is increased due to the long-lived ionic attractions between polymer chains and in some cases can increase viscosity by 7 orders of magnitude relative to the unneutralized acid copolymer.[1] The mole fraction of acid and ion content can therefore be used to tune the ionomer properties in the melt state, even without knowledge of the nanoscale morphology.

Investigations of how ionomers deform have utilized bulk property characterization such as mechanical testing[2-6] or rheology[7-14] and coupled it with small length scale structural or dynamic characterization such as X-rays[15-17], TEM[18-21], FTIR[22, 23], and dielectric measurements[22-27]. Correlating properties and structure in ionomers remains difficult due to the nano-scale dimensions of the aggregates, limitations in characterization techniques at these length scales, and difficulty quantifying heterogeneous morphologies.[28-30] The effect of ionic aggregation on deformation, however, can easily be observed through mechanical testing and much of the literature relies upon indirect or inferred conclusions between these measured properties and the nanoscale morphology. The inability to correlate properties with well characterized morphologies have lead to varied and even contradictory theories of ionomer deformation.[1] In particular, the

morphology during deformation can be transient or undergo morphological evolution necessitating *in situ* experimental observation. Historically *in situ* deformation of ionomers found that average inter-aggregate distances ($1/q^*$) of the broad aggregate peak (q^*) observed in X-ray scattering increases in deformation direction.[2, 15, 16, 31] Further interpretation of the peak shift is limited particularly for commercial ionomers which are polydisperse in chemical composition and chain architecture. The thermal history can also obscure the structure-property correlation because aggregation dramatically slows chain dynamics which can kinetically trap the system after cooling from melt. The result is that semicrystalline ionomers can have significant aging effects and decreased crystallization kinetics.[11, 12, 32-34]

Recent studies on material systems with better control of the chemical structure have given insight into the rheological behavior of ionomers.[8, 13, 14, 35-38] Qiao *et al.* observed the significant changes to the sulfonated polystyrene (SPS) ionomer mechanical response when the aggregate-based physical network was deformed through non-linear shear.[35] The structural characterization of the ionic aggregates remains a challenge due to the nano-scale dimensions of the aggregates, the heterogeneous structures which lead to broader experimentally observed data, and difficulty in separating the impact of neutralization on the simultaneous changes of structure and properties.

An exciting direction is in joint experimental and computer simulations studies which have begun to characterize the nanoscale aggregate morphology under applied fields and relate them to bulk properties.[39-41]

Precise polymers enable the investigation of deformation in ionomers without some of the historical challenges. Precise polymers have a more homogenous polymer

structure than those polymerized through free radical synthesis methods, namely, strictly linear polyethylene backbones and perfectly periodic spacings between pendant acid groups.[42-44] This uniform placement of acid groups along the chain leads to a narrower and more intense interaggregate scattering peak highlighting even small changes in the aggregate peak positions or shape.[45] Furthermore, the effect of neutralization on the equilibrium morphologies have been well investigated through experiments and simulations.[28-30, 46-52]

In a previous study it was shown that associating acrylic acid groups in precise polyethylenes play a key role in a strain-hardening mechanism observed during tensile deformation.[53] Furthermore, it was found that acid group placement along the chain, periodic or random, significantly changed the morphology evolution and tensile properties in the various unneutralized, acid polymers at room temperature.[54] The understanding of acid form deformation establishes a baseline to investigate the role of neutralization on morphology evolution during deformation.

Here we present a follow-up study to the investigation on the role of acid periodicity and placement in acid functionalized linear polyethylenes. In this study the role of partial neutralization (<40%) of the acid groups is examined. Thus, the effect of neutralization on the morphology evolution during tensile deformation is presented. Room temperature deformation, which is below T_g or T_m of the ionomers, resulted in brittle failure without significant morphology evolution. Therefore the deformation and morphology evolution at elevated temperature is the primary focus of this study. These studies show that ionomers in the melt state can have sufficient chain mobility resulting in significant morphological evolution during deformation. Moreover, the morphology evolution is similar to the unneutralized acid forms deformed at lower temperatures. Namely, the polymer chains

align and hierarchical aggregate morphologies develop along the deformation direction. The similarity in deformation behavior of unneutralized acid forms and ionomer forms suggest the polymer structure determines the possible morphologies, while the ion content impacts the thermal conditions necessary to access or produce these morphologies.

EXPERIMENTAL SECTION

Materials. The synthesis methods of precise poly(ethylene-*co*-acrylic acid) were reported previously.[42, 53] A symmetric diene was synthesized with a protected acid group, these macromonomers were polymerized using acyclic diene metathesis (ADMET), and then the double bonds were hydrogenated and the acid group deprotected to yield a linear precise polymer. The sample notation (p*x*AA-*y*%M^+) provides the precise number of backbone carbons (*x* = 9, 15, 21) between pendant acrylic acid (AA) groups along the polyethylene chain, and neutralization level (*y%*) indicating what percentage of AA groups are neutralized with a metal cation, M^+ (lithium (Li), sodium (Na), or cesium (Cs)).

The neutralization procedure was based on a previously reported method.[45] The precise acid-containing polymers were dissolved at a concentration of 10% w/w in a 75/25 v/v solvent mixture of 1,4 dioxane and 1-butanol at 70 ºC. A stoichiometric amount of dried metal salts (lithium acetate, sodium acetate, or cesium acetate) was dissolved in a 75/25 dioxane/1-butanol mixture at less than 0.1% w/w concentration. The metal salt solution was added drop wise into the polymer solution. The solution was stirred for 3 h and cooled to room temperature overnight. Ionomer samples were recovered via precipitating with methanol, filtered and washed three times in succession between fresh methanol and fresh dioxane to remove any unreacted metal salts at 50 ºC. The sample was then dried under vacuum at 80 °C for a minimum of 3 days. The extent of neutralization achieved from the solution neutralization procedure was determined by inductively coupled plasma

elemental analysis performed by Galbraith Laboratories (Knoxville, TN) on samples with masses ranging from 30 – 50 mg. The error is estimated at +/- 0.5 wt% which corresponds to approximately +/- 5% in the reported mol % neutralization.

Table 4.1. Polymer nomenclature, composition, thermal characterization (DSC), and molecular weight characterization (GPC) of the polymers studied.

Material	T_g (C°)	T_m (C°) (ΔH_m in J/g)	M_n (kg/mol)	PDI (M_w/M_n)
p9AA	7	-	27.6	1.44
p9AA-35Li%	69	-	27.9	1.44
p15AA	3	-	62.7	1.78
p15AA-38%Li	53	-	63.3	1.78
p21AA	13	46.0 (ΔH_m=60.5)	18.3	1.9
p21AA-38%Li		47.9 (ΔH_m=25.2)	13.9	2.16

Sample Preparation. Samples were prepared for both X-ray scattering characterization and tensile testing with the same procedure. Films were melt-pressed in a Carver 4122 hot press at 130°C, which is above the T_g and T_m, for 20 min. The films are then rapidly cooled to room temperature (~15°C/min). The tensile samples (10mm x 3mm x 0.13mm) were then cut from the films into a rectangular sample to fit within the Linkam

TST350 tensile system. All films were aged a minimum of 3 days in an evacuated desiccator at room temperature before conducting experiments.

In situ X-ray Scattering and Uniaxial Deformation. *In situ* synchrotron X-ray scattering was conducted at beamline 5ID-D (DND-CAT) of the Advanced Photon Source (APS) at Argonne National Laboratory. Room temperature tensile tests were conducted on a Linkam TST350 Tensile System, which has lead screws that drive the grips in opposite directions to maintain the sample center in the X-ray beam throughout the *in situ* experiment with strain rates of $1.7s^{-1}$. The semi-crystalline samples exhibit necking and the scattering data was collected from within the necked region either by shifting the sample vertically to position the necked region in the beam path, or by adding a small notch in the sample gage length to initiate necking near the incident beam.

Engineering stress-strain values were calculated based on the initial dimensions of the sample and the force-displacement measurements from the tensile instrument. Simultaneously with sample deformation, two-dimensional X-ray scattering data was collected. Two detector configurations were used. First, a single MAR-CCD detector used a sample-to-detector distance of 0.32 m and the X-ray energy was 17 keV (λ=0.73Å). This experimental setup provides X-ray scattering information with a q-range of $1.54\text{-}17.98nm^{-1}$ to capture information from length scales of d = 0.3-6.5 nm. Exposure times of 1 s obtained sufficient counting statistics, while minimizing collection time to provide good time resolution during continuous deformation. Additionally, a 6 s delay between exposures was necessary to refresh the detector. The second detector configuration used three MAR-CCD detectors with sample-to-detector distances of 0.2m, 0.14m and 8.5m to provide overlapping q-ranges. The X-ray energy was 17 keV (λ=0.73Å) and the full q-range was $0.0256\text{-}34.4nm^{-1}$ corresponding to length scales of d = 0.18-245nm. Exposure

times were 1 s with a 3.5 s delay between exposures. In both detector configurations silver behenate and amorphous carbon were used to calibrate the scattering angle and normalize detector counts, respectively. The scattering signals were corrected for beam intensity fluctuations, dark counts and Kapton window background scattering. Two-dimensional data reduction and analysis were performed using the Datasqueeze software.[55]

DISCUSSION

Initial Morphologies. The effect of lithium neutralization on the equilibrium morphologies of the precise ionomers is shown in Figure 4.1. The room temperature, isotropic morphologies for the precise acid functionalized polymers matched those of previously reported values, namely that p21AA is semi-crystalline with an acid-rich layered morphology and ordering of the methylene spacers between acid-layers. When the spacers between acid groups are shorter the polymers are amorphous, such that p15AA and p9AA both exhibit a liquid-like distribution of discrete aggregates.[47-49]

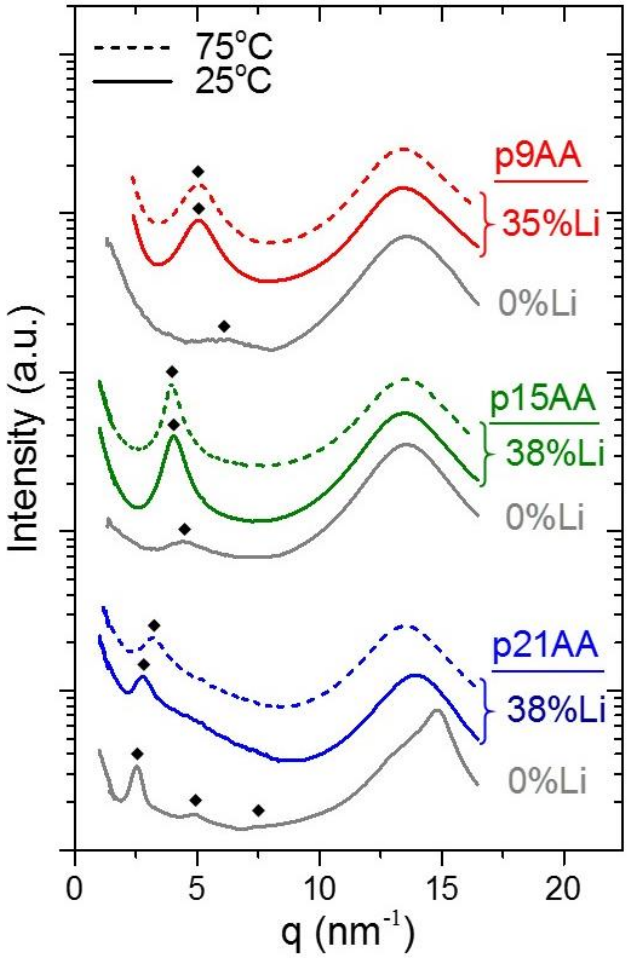

Figure 4.1. X-ray scattering data of the unneutralized and neutralized polymer prior to tensile deformation at 25°C (solid lines) and 75°C (dashed lines). Scattering intensities were azimuthally (360°) integrated and shifted vertically for clarity. Diamonds highlight interaggregate scattering.

Upon partial neutralization (~38%) aggregates consist of both ionic and acid groups. X-ray scattering of p21AA, bottommost curve in Figure 4.1, exhibits isotropically oriented acid-rich layers: an acid peak at low-*q* corresponding to inter-acid distances (*d* = 2.5nm) of nearly the all-*trans* 21 methylene units (2.6nm), higher order reflections of this ionic peak indicating a layered morphology (*q*=1q:2q:3q*), and at higher *q* the amorphous

halo and a crystalline reflection at a *q*-value consistent with orthorhombic [110] PE (*q* = 14.9nm^{-1}).[42, 45] Upon partial neutralization with lithium, p21AA-38%Li shows nominally the same layered morphology. The ionomer form has a similar layer spacing, (*d* = 2.3nm), but the primary peak is slightly broader in *q*, has weaker higher order reflections, and the loss of the crystalline reflection at *q* = 14.9nm^{-1}. Figure 4.2, below, demonstrates the gradual loss of the well-defined layer morphology at a series of increasing Li-ion contents given the same thermal treatment. In p21AA a lamellar peak at low *q* is present, acid layer peak with higher order reflections, and ordered methylene peak at high *q*. All of these features become less ordered with increasing ion content given the same thermal treatment to the samples, namely, cooling from the melt and aging at room temperature.

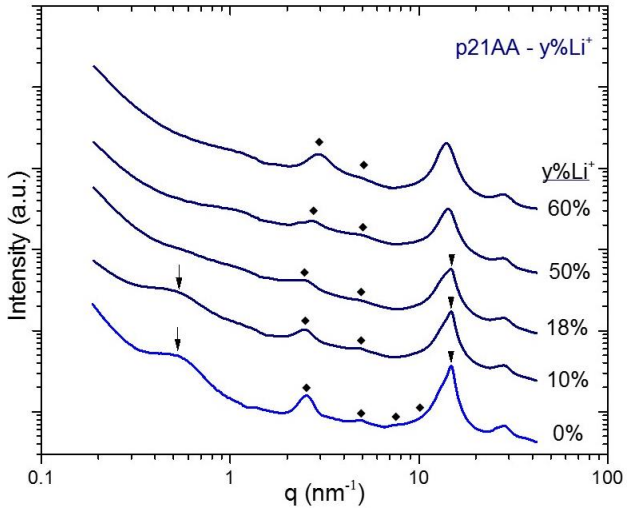

Figure 4.2. X-ray scattering data at 25°C from unoriented p21AA with 0-100% lithium neutralization. Arrows at low *q* highlight the lamellae peak, diamonds indicate the layered acid morphology, and triangles indicate the crystalline peak at high *q*. The *I* vs *q* data were integrated from 360° azimuthal angles. The curves were shifted vertically for clarity.

The p15AA acid-containing polymer shows a peak at low *q* corresponding to the interaggregate distance (1.4nm) and an amorphous halo at higher *q*. Upon neutralization, p15AA-38%Li, the low-*q* peak increases significantly in intensity and shifts to lower *q* corresponding to a longer interaggregate distance (1.6nm). These changes in morphology of amorphous ionomers matches the trends reported previously at 150°C in precise PE-based ionomers.[49] Figure 4.1 shows the room temperature (lines) and morphologies at 75°C (dashed lines). While morphology type is unchanged by heating above T_g, the interaggregate peak and amorphous halo shift slightly to lower *q* due to thermal expansion.[45]

The p9AA acid-containing polymer shows a low-*q* peak and an amorphous halo at high *q* consistent with previous reports and indicating a liquid-like arrangement of discrete aggregates with an interaggregate distance of 1nm. Upon neutralization the interaggregate spacing increases (1.25nm) and peak intensity increases significantly. The amorphous halo has minor changes to the breadth but the peak position remains unchanged. The morphology above the T_g, similar to the behavior of the p15AA ionomer, shows no change beyond the effect of thermal expansion. All acid- and ion-containing polymers with nanoscale aggregation exhibit a low *q* upturn that increases with higher acid and ion content.

In Situ Tensile Data. Figure 4.3 shows the *in situ* tensile data for the unneutralized (25°C) and neutralized (75°C) precise polymers. The partial neutralization of p21AA with lithium increases the glass transition, and thereby increases the yield strength and ultimate strength of p21AA-38%Li at 25°C relative to p21AA. The increased T_g also results in a more brittle sample with failure at significantly lower strains than the acid form. At 75°C

(>T_m) p21AA-38%Li is substantially weaker in the melt state and interestingly exhibits strain hardening when deformed to large strains (≥500%).

In amorphous p15AA the effect of partial neutralization enhances the glass transition to above room temperature. As a result p15AA-38%Li is glassy with a high elastic moduli and brittle failure at relatively low strains. At 75°C (>T_g), the melt state ionomer exhibits strain hardening as previously observed in the acid form at 25°C. Neutralization introduces electrostatic interactions between functional groups, which are stronger than H-bonds and necessitate elevated temperature for sufficient chain mobility to rearrange under deformation. The long-lived ionic aggregates in the melt state lead to tensile strain-hardening and, as will be detailed below, a morphological transformation from isotropic discrete aggregates to aligned layered aggregates.

At 25°C, the mechanical response of the p9AA acid-containing polymer goes from viscous flow capable to deformation to >1500% strain to a glassy response with brittle yielding and failure for p9AA-35%Li. At elevated temperature p9AA-35%Li deforms to substantial strains (~1000%) and demonstrates significant tensile strain-hardening. While p9AA had the lowest mechanical properties of the acid-containing polymers tested at room temperature, when deformed above the T_g (75°C), p9AA-35%Li is the strongest precise ionomer tested. The melt-state strength coincided with the highest ion content and indicative of the long-lived ionic aggregates providing mechanical stability in the melt state.

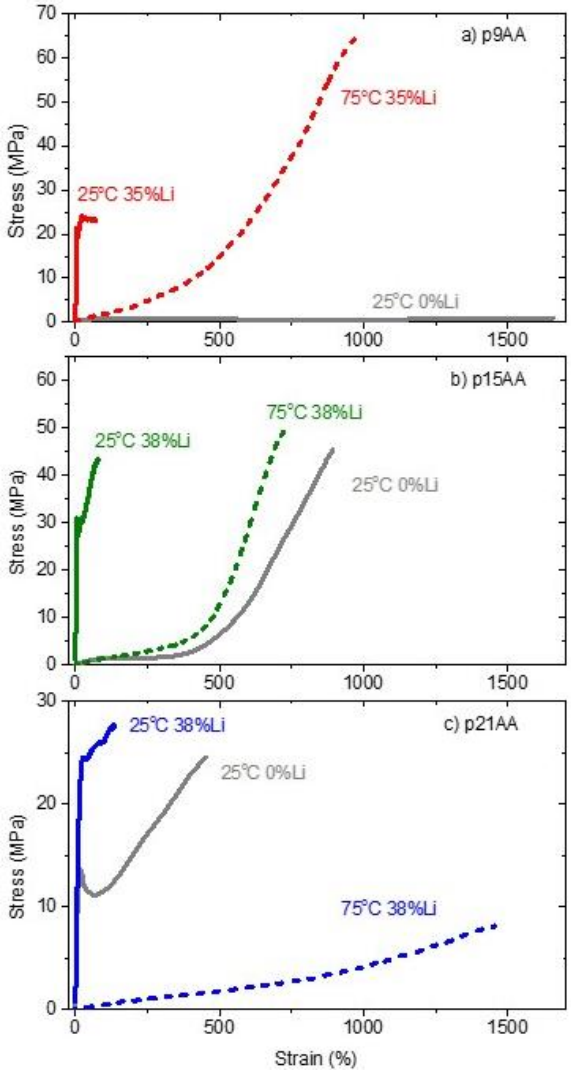

Figure 4.3. *In situ* engineering stress-strain tensile data for unneutralized (25°C, grey[53]) and partially neutralized (25°C solid, 75°C dashed) precise polymers a) p9AA b) p15AA c) p21AA. The tensile deformation strain rate was $\dot{\varepsilon}=1.7s^{-1}$.

Morphology Evolution. The melt state morphology of the precise ionomers deformed at 75°C are shown in Figure 4.4. Initially all three precise ionomer have an isotropic morphologies indicated by a uniform intensity for all azimuthal angles. After the

yield point the polymer chains begin to strongly align such that the amorphous halo orients perpendicular to the draw direction (along equator) indicating that the polymer chains have aligned along the deformation direction. The ionomer peak simultaneously orients parallel to the deformation direction (along the meridian). At large strains nearing the point of failure of the sample, the highly anisotropic morphologies develop wherein the ionomer peak has high intensity and the peak shape in the 2D data adopts a crescent-shape (aggregate peak *q* position is not constant with azimuthal angle), consistent with the layered morphology observed in the acid forms. This morphology evolution is identical to that observed in the p21AA acid form when deformed at 25°C.[53, 54]

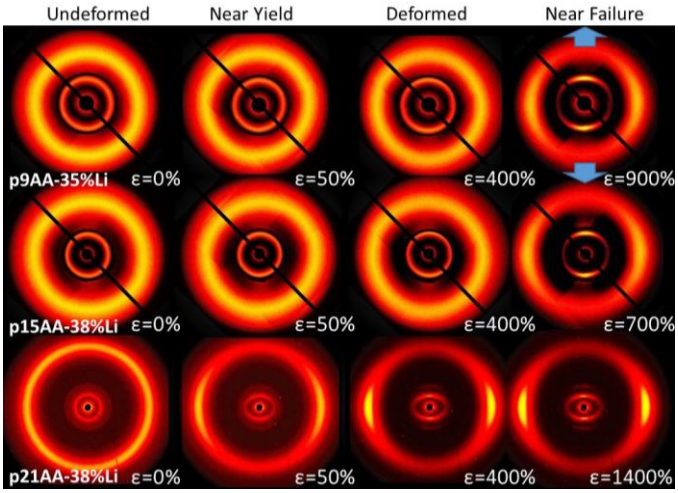

Figure 4.4. *In situ* 2D X-ray scattering overview for the precise Li-ionomers at selected strains and 75°C. Data collected by multiple detectors were stitched together (top 2 rows) while data collected on a single detector is also shown (bottom row). The tensile deformation is applied at $\dot{\varepsilon}$=1.7 s^{-1}.The linear intensity scale is adjusted for each scattering pattern. The blue arrows indicate the deformation direction.

The shifting in *q* and changes in intensity of the X-ray scattering data parallel and perpendicular to deformation are shown in Figure 4.5. p21AA-38%Li is in the melt state at

75°C, and upon deformation the ionomer peak parallel to deformation shifts slightly towards the all-*trans* methylene spacer distance. The ionomer peak does not change substantially in intensity. These two observations of the ionomer peak coincide with the relatively weak strain-hardening properties when compared with the other precise ionomers. In the equilibrium melt-state p21AA does not form layers due to the melting of the crystallites. Deformation in the melt-state is, however, able to orient chains and develop a weak layered morphology, see Figure 4.6. Given that p21AA has the lowest acid- and ion-content of the precise ionomers, it is expected to have the lowest mechanical properties in the melt state and exhibits the least chain alignment given the same temperature and strain rate.

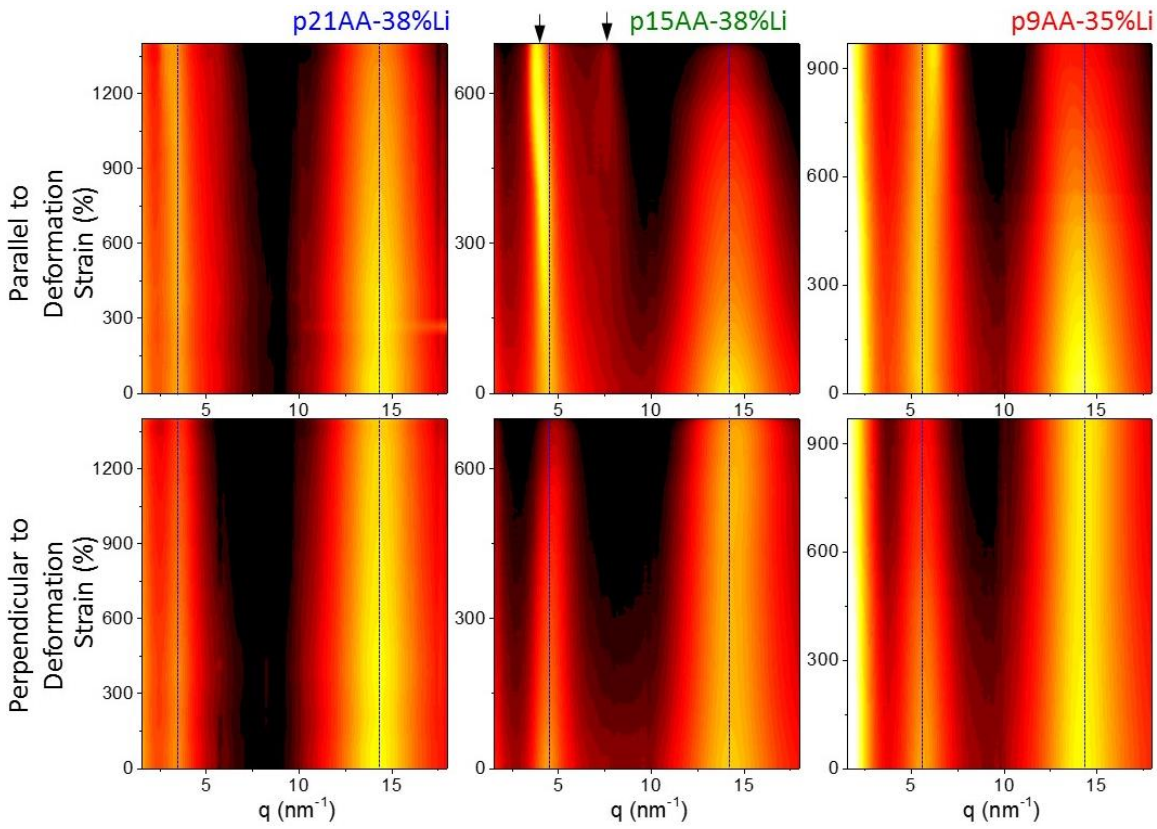

Figure 4.5. *In situ* X-ray scattering intensities as a function of *q* and strain (ε) are plotted for X-ray scattering parallel to deformation (top row) and perpendicular to deformation (bottom row). The dashed lines indicate the undeformed peak positions in *q*. The log *I(q)* data is averaged over ±15 degrees from the specified direction. Scattering intensity units are arbitrary counts with the color black equivalent to background. Arrows indicate multiple reflections (*q*/q* of 1:2:3), corresponding to layered morphologies.

p15AA ionomer exhibits morphology evolution at 75°C of liquid-like to layered morphology transformation, Figure 4.5 middle. This is the same mechanism observed in the p15AA unneutralized acid form during deformation at 25°C, namely that the layered morphology formation coincided with the strain hardening. The ionomer peak shifts to lower *q* (*q* = 4.5 to 3.8nm^{-1}), approaching the all-*trans* distance of the PE spacer (*q* = 3.3nm^{-1}). The ionomer peak increases in intensity. A higher order reflection indicative of

the layered morphology also appears (q = 7.6nm^{-1}), see Figure 4.6. In the perpendicular direction the ionomer peak moves to slightly higher q, as expected when ionic aggregates act the long-lived crosslinks, but does not maintain affine deformation at these high strains and elevated temperatures suggesting that aggregates can break and reform throughout deformation.

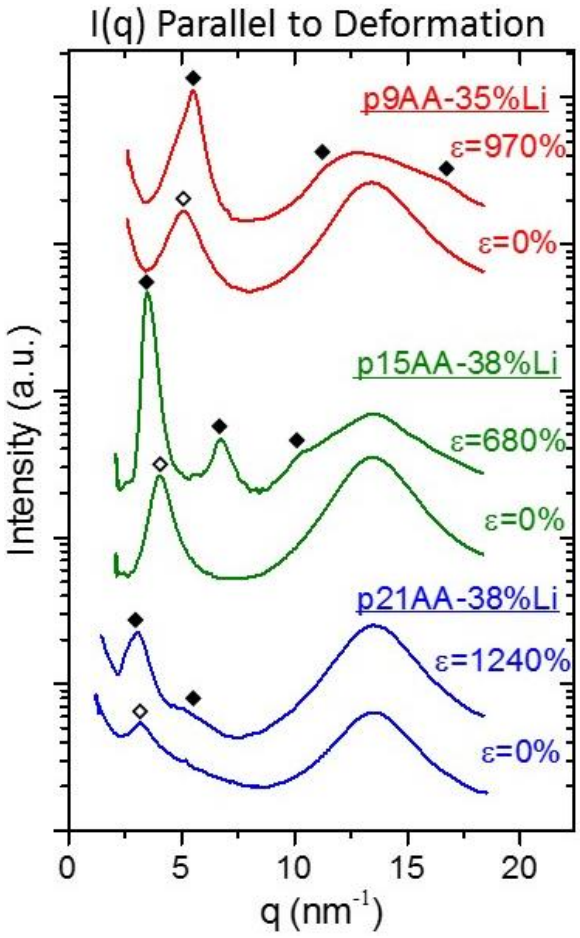

Figure 4.6. *In situ* X-ray scattering parallel to deformation in a 10° azimuthal integration at 75°C. *In situ* X-ray scattering parallel to deformation of precise ionomers at 75°C. A single scattering peak (open diamond) in the undeformed samples evolves into multiple

higher order reflections (filled diamonds) corresponding to a layered morphologies at high strains. The curves are shifted vertically for clarity.

The most unusual morphological behavior is observed in the sample with the highest ion content, p9AA-35%Li. The ionomer peak in the parallel direction shifts to *higher q* in the parallel direction (unlike previous observations of the aggregate peak) and increases in intensity. Additionally the ionomer peak becomes asymmetric at high strains. The high *q* side of the aggregate peak appears to have a peak whose *q*-position coincides with a layered morphology which suggests heterogeneity in the distribution of inter-aggregate length scales. The ionomer peak in the perpendicular direction does not change in *q* but decreases in intensity throughout deformation. Furthermore, the amorphous halo forms an unusual breadth in intensity above 300% strain in the parallel direction, as seen in Figure 4.6. It was found that this is due to the formation of a layered morphology in p9AA ionomer, and the higher order reflections overlap with the amorphous halo (*q*=1q:2q:3q*). Figure 4.7, below, shows *I(q)* across a series of strain values for more detailed view of the layer morphology formation. Prior to deformation at q = 10-18nm^{-1} a typical PE-like amorphous halo is observed. Upon deformation, however, the p9AA-35%Li ionomer amorphous halo developed an unusual shape. This is a result of the overlap with the higher order reflections of the aggregate peak at lower *q*. The black diamonds highlight the q-positions for higher order reflections of the primary aggregate peak at lower *q*.

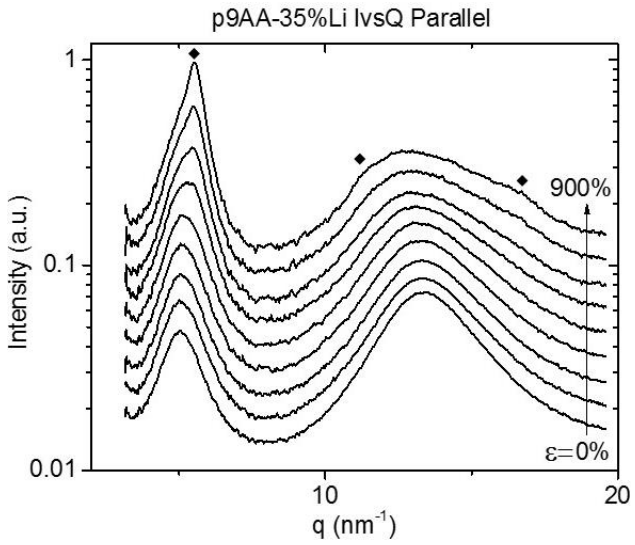

Figure 4.7. *In situ* X-ray scattering parallel to deformation of p9AA-35%Li at 75°C. The curves are in 100% strain increments and shifted vertically for clarity. *The I(q)* data were integrated ± 5degrees from the meridian.

The aggregate peak position parallel and perpendicular to deformation is plotted as a function of strain in Figure 4.8. p21AA-38%Li, p15AA-38%Li as well as previous reports on p21AA, p15AA and p9AA have had the aggregate peak parallel to deformation shift to lower q with tensile deformation. This change in aggregate q-position coincided with substantial anisotropy in the 2D X-ray scattering data indicating both chain orientation and chain alignment in the deformation direction. In all these cases the inter-aggregate peak position tends towards the all-trans methylene spacer length consistent with chain alignment. p9AA-35%Li, however, initially starts with aggregate peak q position lower than the all-trans PE distance (q_{agg} = 5.57 nm^{-1} , $q_{all\text{-}trans\ c\text{-}c}$ = 5.5nm^{-1}). In this case the aggregate peak in the parallel direction also tends towards the all-trans length of the PE spacer length, resulting in the peak motion in opposite that of the other polymers tested.

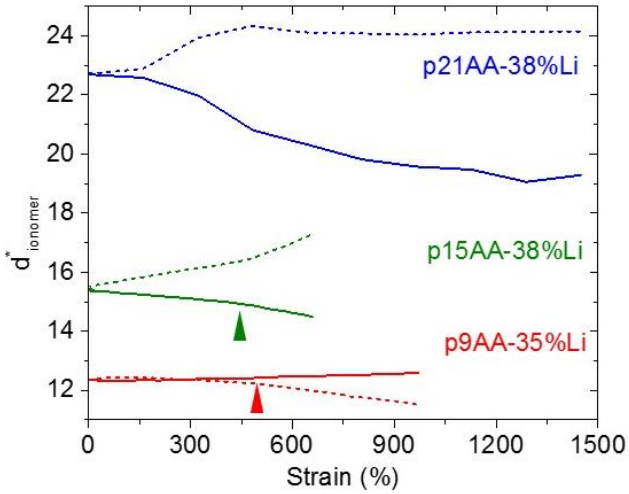

Figure 4.8. The interaggregate ionomer peak $d^*_{ionomer}$ as a function of strain from in situ scattering data of the precise ionomers at 75°C. The ionomer peak $d^*=2\pi/q^*$ parallel (solid) and perpendicular (dashed) to the applied strain are shown. Substantial anisotropy develops in the 2D scattering data and layered morphology formation occurs at the colored arrows. These strain coincide with tensile strain hardening in p9AA-35%Li and p15AA-38%Li, whereas p21AA-38%Li doesn't substantially strain harden.

CONCLUSIONS

The morphology evolution during tensile deformation was investigated for a series of precise ionomers. The role of spacing between acid groups along the linear PE backbone (the number of carbons between pendant groups), fraction of neutralized acid groups, and effect of temperature were examined. *In situ* X-ray scattering during room and elevated temperature tensile deformation captured the morphological evolution continuously from the initial isotropic state until failure.

The neutralization of ~35% of the acid groups with Li^+ significantly changes the thermal transitions, tensile properties and morphology evolution through formation of ionic aggregates. The unneutralized precise acid polymers exhibit H-bonded aggregates, which

upon neutralization, form larger aggregates comprised of both ionic and H-bonds and are long-lived at elevated temperatures. Consequently, neutralization of the acids lead to an increase in T_g as measured by DSC in the amorphous polymers, as well as decreased crystallization in the semi-crystalline polymers given the same thermal treatment. Additionally, the morphology measured through X-ray scatting indicates an increase in the low-*q* aggregate peak intensity and a shift towards lower *q*-position indicating larger inter-aggregate distances.

The morphology evolution under tensile deformation of the precise ionomers at 75°C, in the melt state, leads to morphology evolution similar to that of the unneutralized acid-containing polymers when deformed at lower temperatures. Specifically, the precise polymers form an anisotropic oriented layered morphology, coinciding with strain hardening. Additionally, the highest acid and ionic content lead to the highest mechanical properties while in the melt state due to the long-lived ionic aggregates. At the same strain rate and temperature, the lowest acid and ion content ionomer, p21AA-38%Li, showed the least strain hardening and orientation of the layered morphology confirming the impact of the long-lived ionic aggregates on morphology evolution while in the melt state. The precise ionomers did not exhibit significant morphology evolution at room temperature due to the glassy response of the polymer and insufficient chain mobility needed to form the hierarchical layered morphology.

This study indicates that the neutralization of the acid-functionalized precise polymers significantly impacts the thermal transitions and mechanical properties, however, the accessible morphologies remain controlled by the polymer structure. The effect of longer-lived ionic aggregation, relative to H-bonded aggregates, impacts the

conditions under which anisotropic layered morphologies can form due to changes in the chain mobility through facile aggregate exchange.

REFERENCES

1. Adi Eisenberg, J.-S. K., *Introduction to Ionomers*. 1st ed.; Wiley: New York, 1998; p 326.

2. Roche, E. J.; Stein, R. S.; Russell, T. P.; Macknight, W. J. Small-angle x-ray scattering study of ionomer deformation. *Journal of Polymer Science: Polymer Physics Edition* **1980,** 18, (7), 1497-1512.

3. Lantman, C. W.; MacKnight, W. J.; Lundberg, R. D. Structural Properties of Ionomers. *Annual Review of Materials Science* **1989,** 19, (1), 295-317.

4. Ma, X.; Sauer, J. A.; Hara, M. Deformation modes of poly(styrene-co-sodium methacrylate) ionomers. *Polymer* **1996,** 37, (21), 4739-4745.

5. Scogna, R. C.; Register, R. A. Plastic deformation of ethylene/methacrylic acid copolymers and ionomers. *Journal of Polymer Science Part B: Polymer Physics* **2009,** 47, (16), 1588-1598.

6. Scogna, R. C.; Register, R. A. Yielding in ethylene/methacrylic acid ionomers. *Polymer* **2009,** 50, (2), 585-590.

7. Vanhoorne, P.; Register, R. A. Low-Shear Melt Rheology of Partially-Neutralized Ethylene−Methacrylic Acid Ionomers. *Macromolecules* **1996,** 29, (2), 598-604.

8. Colby, R. H.; Zheng, X.; Rafailovich, M. H.; Sokolov, J.; Peiffer, D. G.; Schwarz, S. A.; Strzhemechny, Y.; Nguyen, D. Dynamics of Lightly Sulfonated Polystyrene Ionomers. *Physical Review Letters* **1998,** 81, (18), 3876-3879.

9. Takahashi, T.; Watanabe, J.; Minagawa, K.; Koyama, K. Effect of ionic interaction on elongational viscosity of ethylene-based ionomer melts. *Polymer* **1994,** 35, (26), 5722-5728.

10. Tierney, N. K.; Register, R. A. The Role of Excess Acid Groups in the Dynamics of Ethylene−Methacrylic Acid Ionomer Melts. *Macromolecules* **2002,** 35, (16), 6284-6290.

11. Loo, Y.-L.; Wakabayashi, K.; Huang, Y. E.; Register, R. A.; Hsiao, B. S. Thin crystal melting produces the low-temperature endotherm in ethylene/methacrylic acid ionomers. *Polymer* **2005,** 46, (14), 5118-5124.

12. Wakabayashi, K.; Register, R. A. Micromechanical interpretation of the modulus of ethylene-(meth)acrylic acid copolymers. *Polymer* **2005,** 46, (20), 8838-8845.

13. Weiss, R. A.; Zhao, H. Rheological behavior of oligomeric ionomers. *Journal of Rheology* **2009,** 53, (1), 191-213.

14. Chen, Q.; Tudryn, G. J.; Colby, R. H. Ionomer dynamics and the sticky Rouse model. *Journal of Rheology* **2013,** 57, (5), 1441-1462.

15. Eisenberg, A.; Hird, B.; Moore, R. B. A New Multiplet-Cluster Model for the Morphology of Random Ionomers. *Macromolecules* **1990,** 23, (18), 4098-4107.

16. Yarusso, D. J.; Cooper, S. L. Analysis of SAXS data from ionomer systems. *Polymer* **1985,** 26, (3), 371-378.

17. Moore, R. B.; Bittencourt, D.; Gauthier, M.; Williams, C. E.; Eisenberg, A. Small-angle x-ray scattering investigations of ionomers with variable-length side chains. *Macromolecules* **1991,** 24, (6), 1376-1382.

18. Li, C.; Register, R. A.; Cooper, S. L. Direct observation of ionic aggregates in sulphonated polystyrene ionomers. *Polymer* **1989,** 30, (7), 1227-1233.

19. Benetatos, N. M.; Heiney, P. A.; Winey, K. I. Reconciling STEM and X-ray Scattering Data from a Poly(styrene-ran-methacrylic acid) Ionomer: Ionic Aggregate Size. *Macromolecules* **2006,** 39, (16), 5174-5176.

20. Benetatos, N. M.; Chan, C. D.; Winey, K. I. Quantitative Morphology Study of Cu-Neutralized Poly(styrene-ran-methacrylic acid) Ionomers: STEM Imaging, X-ray Scattering, and Real-Space Structural Modeling. *Macromolecules* **2007,** 40, (4), 1081-1088.

21. Benetatos, N. M.; Winey, K. I. Nanoscale Morphology of Poly(styrene-ran-methacrylic acid) Ionomers: The Role of Preparation Method, Thermal Treatment, and Acid Copolymer Structure. *Macromolecules* **2007,** 40, (9), 3223-3228.

22. Lu, M.; Runt, J.; Painter, P. An Infrared Spectrocopic Study of a Polyester Copolymer Ionomer Based on Poly(ethylene oxide). *Macromolecules* **2009,** 42, (17), 6581-6587.

23. Chen, Q.; Masser, H.; Shiau, H.-S.; Liang, S.; Runt, J.; Painter, P. C.; Colby, R. H. Linear Viscoelasticity and Fourier Transform Infrared Spectroscopy of Polyether–Ester–Sulfonate Copolymer Ionomers. *Macromolecules* **2014,** 47, (11), 3635-3644.

24. Yano, S.; Tadano, K.; Nagao, N.; Kutsumizu, S.; Tachino, H.; Hirasawa, E. Dielectric relaxation studies on water absorption of ethylene ionomers. *Macromolecules* **1992,** 25, (26), 7168-7171.

25. Castagna, A. M.; Wang, W.; Winey, K. I.; Runt, J. Influence of the Degree of Sulfonation on the Structure and Dynamics of Sulfonated Polystyrene Copolymers. *Macromolecules* **2010,** 43, (24), 10498-10504.

26. Castagna, A. M.; Wang, W.; Winey, K. I.; Runt, J. Structure and Dynamics of Zinc-Neutralized Sulfonated Polystyrene Ionomers. *Macromolecules* **2011,** 44, (8), 2791-2798.

27. O'Reilly, M. V.; Masser, H.; King, D. R.; Painter, P. C.; Colby, R. H.; Winey, K. I.; Runt, J. Ionic aggregate dissolution and conduction in a plasticized single-ion polymer conductor. *Polymer* **2015,** 59, 133-143.

28. Hall, L. M.; Seitz, M. E.; Winey, K. I.; Opper, K. L.; Wagener, K. B.; Stevens, M. J.; Frischknecht, A. L. Ionic aggregate structure in ionomer melts: effect of molecular architecture on aggregates and the ionomer peak. *Journal of the American Chemical Society* **2012,** 134, (1), 574-87.

29. Bolintineanu, D. S.; Stevens, M. J.; Frischknecht, A. L. Atomistic Simulations Predict a Surprising Variety of Morphologies in Precise Ionomers. *ACS Macro Letters* **2013,** 2, (3), 206-210.

30. Bolintineanu, D. S.; Stevens, M. J.; Frischknecht, A. L. Influence of Cation Type on Ionic Aggregates in Precise Ionomers. *Macromolecules* **2013,** 46, (13), 5381-5392.

31. Yarusso, D. J.; Cooper, S. L. Microstructure of ionomers: interpretation of small-angle x-ray scattering data. *Macromolecules* **1983,** 16, (12), 1871-1880.

32. Ruan, D.; Simmons, D. S. Glass Formation near Covalently Grafted Interfaces: Ionomers as a Model Case. *Macromolecules* **2015,** 48, (7), 2313-2323.

33. Ruan, D.; Simmons, D. S. Roles of chain stiffness and segmental rattling in ionomer glass formation. *Journal of Polymer Science Part B: Polymer Physics* **2015,** 53, (20), 1458-1469.

34. Wakabayashi, K.; Register, R. A. Morphological origin of the multistep relaxation behavior in semicrystalline ethylene/methacrylic acid ionomers. *Macromolecules* **2006,** 39, (3), 1079-1086.

35. Qiao, X.; Weiss, R. A. Nonlinear Rheology of Lightly Sulfonated Polystyrene Ionomers. *Macromolecules* **2013,** 46, (6), 2417-2424.

36. Chen, Q.; Huang, C.; Weiss, R. A.; Colby, R. H. Viscoelasticity of Reversible Gelation for Ionomers. *Macromolecules* **2015,** 48, (4), 1221-1230.

37. Huang, C.; Wang, C.; Chen, Q.; Colby, R. H.; Weiss, R. A. Reversible Gelation Model Predictions of the Linear Viscoelasticity of Oligomeric Sulfonated Polystyrene Ionomer Blends. *Macromolecules* **2016,** 49, (10), 3936-3947.

38. Leibler, L.; Rubinstein, M.; Colby, R. H. Dynamics of reversible networks. *Macromolecules* **1991,** 24, (16), 4701-4707.

39. Agrawal, A.; Perahia, D.; Grest, G. S. Clustering effects in ionic polymers: Molecular dynamics simulations. *Physical Review E* **2015,** 92, (2), 022601.

40. Agrawal, A.; Perahia, D.; Grest, G. S. Cluster Morphology-Polymer Dynamics Correlations in Sulfonated Polystyrene Melts: Computational Study. *Physical Review Letters* **2016,** 116, (15), 158001.

41. Ting, C. L.; Stevens, M. J.; Frischknecht, A. L. Structure and Dynamics of Coarse-Grained Ionomer Melts in an External Electric Field. *Macromolecules* **2015,** 48, (3), 809-818.

42. Baughman, T. W.; Chan, C. D.; Winey, K. I.; Wagener, K. B. Synthesis and Morphology of Well-Defined Poly(ethylene-co-acrylic acid) Copolymers. *Macromolecules* **2007,** 40, (18), 6564-6571.

43. Opper, K. L.; Fassbender, B.; Brunklaus, G.; Spiess, H. W.; Wagener, K. B. Polyethylene Functionalized with Precisely Spaced Phosphonic Acid Groups. *Macromolecules* **2009,** 42, (13), 4407-4409.

44. Choi, U. H.; Middleton, L. R.; Soccio, M.; Buitrago, C. F.; Aitken, B. S.; Masser, H.; Wagener, K. B.; Winey, K. I.; Runt, J. Dynamics of Precise Ethylene Ionomers Containing Ionic Liquid Functionality. *Macromolecules* **2015,** 48, (2), 410-420.

45. Seitz, M. E.; Chan, C. D.; Opper, K. L.; Baughman, T. W.; Wagener, K. B.; Winey, K. I. Nanoscale Morphology in Precisely Sequenced Poly(ethylene-co-acrylic acid) Zinc Ionomers. *Journal of the American Chemical Society* **2010,** 132, (23), 8165-8174.

46. Jenkins, J. E.; Seitz, M. E.; Buitrago, C. F.; Winey, K. I.; Opper, K. L.; Baughman, T. W.; Wagener, K. B.; Alam, T. M. The impact of zinc neutralization on the structure and dynamics of precise polyethylene acrylic acid ionomers: A solid-state 13C NMR study. *Polymer* **2012,** 53, (18), 3917-3927.

47. Buitrago, C. F.; Alam, T. M.; Opper, K. L.; Aitken, B. S.; Wagener, K. B.; Winey, K. I. Morphological Trends in Precise Acid- and Ion-Containing Polyethylenes at Elevated Temperature. *Macromolecules* **2013,** 46, (22), 8995-9002.

48. Buitrago, C. F.; Jenkins, J. E.; Opper, K. L.; Aitken, B. S.; Wagener, K. B.; Alam, T. M.; Winey, K. I. Room Temperature Morphologies of Precise Acid- and Ion-Containing Polyethylenes. *Macromolecules* **2013,** 46, (22), 9003-9012.

49. Buitrago, C. F.; Bolintineanu, D. S.; Seitz, M. E.; Opper, K. L.; Wagener, K. B.; Stevens, M. J.; Frischknecht, A. L.; Winey, K. I. Direct Comparisons of X-ray Scattering and Atomistic Molecular Dynamics Simulations for Precise Acid Copolymers and Ionomers. *Macromolecules* **2015,** 48, (4), 1210-1220.

50. Hall, L. M.; Stevens, M. J.; Frischknecht, A. L. Effect of Polymer Architecture and Ionic Aggregation on the Scattering Peak in Model Ionomers. *Physical Review Letters* **2011,** 106, (12).

51. Hall, L. M.; Stevens, M. J.; Frischknecht, A. L. Dynamics of Model Ionomer Melts of Various Architectures. *Macromolecules* **2012,** 45, (19), 8097-8108.

52. Lueth, C. A.; Bolintineanu, D. S.; Stevens, M. J.; Frischknecht, A. L. Hydrogen-bonded aggregates in precise acid copolymers. *J Chem Phys* **2014,** 140, (5), 054902.

53. Middleton, L. R.; Szewczyk, S.; Azoulay, J.; Murtagh, D.; Rojas, G.; Wagener, K. B.; Cordaro, J.; Winey, K. I. Hierarchical Acrylic Acid Aggregate Morphologies Produce Strain-Hardening in Precise Polyethylene-Based Copolymers. *Macromolecules* **2015,** 48, (11), 3713-3724.

54. Middleton, L. R.; Trigg, E. B.; Schwartz, E.; Opper, K. L.; Travis, W. B.; Wagener, K. B.; Winey, K. I. Role of Acid Chemistry and Periodicity on the Morphological Evolution and Strength in Precise Polyethylenes. *Macromolecules* **Submitted**.

55. Heiney, P. Datasqueeze: A Software Tool for Powder and Small-Angle X-Ray Diffraction Analysis. *Commission on Powder Diffraction Newsletter* **2005**, (32), 9-11.

CHAPTER 5

Heterogeneous Chain Dynamics in Precise Acid-Containing Polyethylenes: Experiment and Simulations

Introduction

Predicting and controlling polymer dynamics remains a key challenge in technologically important applications including solid polymer electrolytes (SPEs), water desalination, ion exchange membranes and the chemically amplified photoresists used in the microelectronics industry.[1] These are all applications where function depends upon a coupling of the polymer dynamics to the transport of small molecules or ions through the polymer film. However, polymer dynamics in associating polymers are inherently complex due to the variety of relevant length and time scales, thermally activated processes, chemically heterogeneous morphologies and hierarchical structures. Bulk properties, such as rheology or ion conduction, are the result of the culmination of numerous nanoscale motions at nanosecond timescales, which motivates fundamental studies of polymer dynamics at the nanometer and nanosecond scales.[2-5] Moreover, experimental measurements that quantify polymer dynamics at the nanosecond and even picosecond time scales are critical to validate modeling parameters, so that modeling can then predict the functional properties of new polymeric materials.[6]

The nanoscale dynamics of melt state polyethelyne (PE) include the α-process associated with the structural relaxation of the polymer chain, and faster motions often lumped together into the β-process that includes dynamics restricted in length scale such as caged motion, torsional motion of the main chain, or libration motions of the hydrogens along the PE backbone.[7-13] These dynamics are often described by the empirical stretched

exponential decay Kohlrausch-Williams-Watts (KWW) function. The α-process is stretched (β_{KWW}<1) whereas the β-processes typically exhibit Debye-like dynamics (β_{KWW} ~ 1). The α-process is typically slower by an order of magnitude relative to the β-processes, but at sufficiently high temperatures these dynamics overlap complicating analysis of polymer dynamics.[10] Furthermore, any chemical heterogeneity leads to additional dynamical processes such as side group rotation, chain end dynamics, or multiple α-processes. When polymer chains have associating groups (H-bonding or ionic attraction) the polymer dynamics are substantially altered leading to coupling of segmental dynamics.[14-19] Using a combination of quasi-elastic neutron scattering (QENS) and united-atom molecular dynamics (MD) simulations Lin *et al.* demonstrated that ionic aggregates in PEO based-ionomers act as “anchors”, leading to slower dynamics for :anchor” atoms near the ionic groups and to faster dynamics in backbone atoms further from ionic groups, termed “bridge” atoms.[20, 21] Using coarse-grained simulations of ionomers, Ruan *et al.* showed an increase in the cooperativity of dynamics as temperature approached T_g.[16] Confirming the nanoscale dynamics in associating polymers with the extension to fully atomistic MD and QENS is an important validation in polymer dynamics and a goal of this paper.

Precise acid-functionalized polyethylenes are model systems with well-defined chain architectures that provide an opportunity to study the dynamics of associating polymers. The polymer backbone is strictly linear polyethylene (PE) with pendant acrylic acid (AA) groups located along the backbone on exactly every 9th, 15th, or 21st carbon along the PE backbone, hence the name *precise* acid polyethylenes.[22] Extensive joint experimental-simulation work previously determined the melt-state morphology of the precise acrylic acid-functionalized polyethylenes and the ionomers neutralized with

various cations, at varying levels of neutralization, and temperature.[23-27] The simulations were performed on both coarse-grained[26-29] and fully atomistic[24, 30-32] models, and extensive comparisons between X-ray scattering profiles were made with scattering profiles calculated from MD simulations. Through this approach we were able to develop a molecular level understanding of the static structure through correlations between the real-space distances between aggregates and the experimentally observed ionomer peak often seen at low wavevector for these nanoscale associating polymers.

This study extends these initial comparisons of the static structure into the dynamical regime by examining the effect of associating side groups on the polymer backbone dynamics. The combination of model materials with advanced characterization techniques enables fundamental studies of the nanoscale motion of polymers. Fully atomistic molecular dynamics simulations with the LOPLS force field[33] are in excellent agreement with experimentally measured quasi-elastic neutron scattering data. Large differences in the dynamics along the chain were observed within four methylene groups of H-bonded acrylic acid groups for times less than 2 ns. The time scales of structural relaxation of the “bridge” atoms along the polymer backbone and far from acid groups are significantly faster than those near acid groups, but the chains remain restricted in translation motion until a characteristic timescale for aggregate rearrangement occurs. These observations are seminal because ion transfer between aggregates is believed to be critical for ion conduction. Looking forward, this foundational work provides a baseline to compare with the neutralized, single-ion conducting ionomer systems to reveal mechanisms of ion transport in SPEs.

Experimental Section

Materials. The synthesis methods and morphologies of poly(ethylene-*co*-acrylic acid) precise polymers were reported previously.[22, 34, 35] In brief, a symmetric diene was synthesized with a protected acrylic acid group, these macromonomers were polymerized using acyclic diene metathesis (ADMET), and then the double bonds were hydrogenated and the acid group deprotected. The sample nomenclature is p*x*AA, where p indicates a precise polymer and *x* is the carbon spacing length (*x* = 9, 15 or 21) between pendant acrylic acid (AA) groups. The details of the materials properties are described in Table **5.1**. For comparison, linear PE was synthesized using ADMET and an unfunctionalized macromonomer diene.[36]

Table 5.1. Polymer nomenclature, composition, thermal transitions (T_g and T_m from DSC[35]) and molecular characterization (M_n and PDI from GPC[35]) of the precise polymers used in QENS.

Name	Acid Content (mol%)	T_g (°C)	T_m (°C)	M_n (g/mol)	PDI
PE	0%		129	44,900	1.8
p21AA	9.5%	14	46.0	18,300	1.9
p15AA	13.3%	5	-	62,700	1.8
p9AA	22.2%	12	-	41,500	1.9

X-ray Scattering. Samples were prepared for X-ray scattering characterization through drying in a vacuum oven, above T_g or T_m, for 3 days. The samples were then

loaded into a 1.0mm diameter glass capillary (Charles Supper Co. Special Glass 10-SG[1]) and subsequently flame-sealed. X-ray scattering was performed in the Multi-angle X-ray Scattering (MAXS) Facility at the University of Pennsylvania using a Nonius FR591 rotating-anode generator operated at 40 kV and 85 mA. A bright, highly collimated beam was obtained via Osmic Max-Flux optics and triple pinhole collimation under vacuum. The scattering data were collected for 30 min using a Bruker Hi-Star multiwire two-dimensional detector at a sample-to-detector distance of 11 cm. The sample temperature was controlled by a Linkam TMS 94 temperature controller. The samples were heated to 150 °C and allowed to reach thermal equilibrium for 5 min prior to data collection. Two-dimensional data reduction and analysis of data were performed using the Datasqueeze software.[37]

Quasielastic Neutron Scattering. The QENS experiments were performed using a time-of-flight spectrometer, the disc chopper spectrometer (DCS), at the NIST Center for Neutron Research. Solid polymer films were melt-pressed in a Carver 4122 hot press above the T_g or T_m, for 20 min. The films were then cooled to room temperature at a rate of ~15°C/min through a heat exchanger with circulating tap water. The samples were prepared with a thickness of ~0.15 mm to achieve a transmission of approximately 90% of the incident neutron bean and thereby minimize the contribution of multiple scattering; it is safe to assume that each neutron reaching the detectors has only scattered once. Samples were wrapped in a thin aluminum foil having the same inner circumference as

[1] Certain commercial equipment, instruments, or materials are identified in this paper in order to specify the experimental procedure adequately. Such identification is not intended to imply recommendation or endorsement by the National Institute of Standards and Technology, nor is it intended to imply that the materials or equipment identified are necessarily the best available for the purpose.

the sample holder, and sealed into cylindrical aluminum sample holders under helium gas in a glove box.

Two incident neutron energies were used in the DCS, 5.665meV and 13.089meV (= 3.8 and 2.5 Å, respectively), yielding two energy resolution settings (full width at half-maximum of the elastic peak) of ΔE =229.1 μeV and 772.6 μeV, respectively. The instrumental resolution was collected on p9AA at 20 °K and assumed to be the same for all other samples. Background from a blank aluminum sample holder, dark counts of the detector, and a vanadium calibration standard were accounted for during data reduction. The accessible *Q*-ranges were 0.144 $Å^{-1}$ < *Q* < 3.108 $Å^{-1}$, and 0.219 $Å^{-1}$ < *Q* < 4.723 $Å^{-1}$, for the low and high incident energies, respectively. The raw data were reduced and Fourier transformed using the Data Analysis and Visualization Environment (DAVE) software developed by NIST.[38]

Information of the dynamics on the sample is obtained by analyzing the change in energy of the scattered neutrons (*ħω*). In these samples, the incoherent scattering cross-section of hydrogen is approximately an order of magnitude greater than its coherent counterpart and than the total cross-sections of carbon and oxygen. The collected scattering is therefore dominated by incoherent scattering from the hydrogens of the PE backbone and from the single hydrogen associated with the acrylic acid. The momentum and energy transfer dependence of the incoherent scattering $I_{exp}(Q,)$ is related via Fourier transformation to the intermediate scattering function *S(Q,t)*, taking into account the instrumental resolution effects through the measured instrument resolution function *R(Q,):*

$$S(Q,t) = \frac{\int I_{exp}(Q,\omega) e^{i\omega t} d\omega}{\int R(Q,\omega) e^{i\omega t} d\omega} \quad (1)$$

The *S(Q, t)* data were normalized by *S(Q, t=0)*, however, a small vertical shift factor (<10%) was used to match the simulation dynamics. It should be noted that complete analysis of the QENS data was performed in the energy domain, *S(Q,ω),* and the fits extracted comparable timescales as those found in the time-domain (discussed in Appendix E). We chose to present the time domain analysis here to facilitate comparison with the results from the MD simulations.

Molecular Dynamics Simulations. Our previous atomistic MD simulations of precise acid-functionalized polyethylenes and precise ionomers, neutralized to varying degrees with metal cations (Li, Na, Cs, and Zn), were performed at two temperatures (120 and 150 °C) using the all-atom optimized potentials for liquid simulations (OPLS-AA) fully atomistic force field[39, 40] in LAMMPS.[24, 30-32] For this paper, similar simulations were performed with the recent LOPLS-AA fully atomistic force field, which was developed by Siu *et al.* in 2012 to improve properties of long alkanes.[33, 41] We further tested the LOPLS force field by performing MD simulations on hexadecane and polyethylene (PE), and compared the simulated intermediate scattering function for those systems with QENS data from the literature. Overall we found good agreement as shown in the Appendix E Figures E.2 and E.3. We also found that the dynamics for the precise acid-functionalized polymers generated from simulations using the LOPLS force field agreed much better with QENS data than simulations using the original OPLS force field, which lead to overly slow dynamics (see Appendix E for further details on the force field and Figure E4).

The simulations were performed on oligomers to focus on the effects of the functional group on the structure and dynamics of the polymer near acid aggregates, and to avoid slow dynamics due to polymer entanglements. The dynamics in systems with different acid contents were compared for chains with similar backbone lengths; previously

we performed simulations using a fixed number of acid groups per chain to probe aggregate structure.[24, 30, 31] Thus, in the new simulations presented here the p9AA systems contained 80 chains each with 9 acid groups per chain and 81 backbone carbons (M_n = 1,356 g/mol), the p15AA systems had 82 chains each with 6 acid groups per chain and 90 backbone carbons (M_n = 1,529 g/mol), and the p21AA systems had 80 chains each with 4 acid groups per chain and 84 backbone carbons (M_n = 1,534 g/mol). The simulation of PE used 80 chains each with 84 carbons per chain (M_n = 1,180 g/mol). The average dynamics predicted by simulations were found to be sensitive to the enhanced dynamics of chain ends in these oligomer systems, and therefore the dynamics of the chain ends were excluded from the calculations of dynamics.

All simulations used the LAMMPS software package, with a real-space nonbonded cutoff of 12 Å and the particle−particle particle-mesh (PPPM) solver for electrostatics.[42] A Nosé-Hoover thermostat with a 100.0 fs damping parameter was used to maintain the temperature at 150 °C. Interestingly, simulations run with a Langevin thermostat exhibited markedly slower dynamics; for further details see Appendix E. The integration time step was set to 1.0 fs in all cases. Initial states for each system were created by a configurational-bias Monte Carlo simulation[43, 44], which builds the system near the desired density. Each system was then simulated in the NPT ensemble at 1 atm pressure and 150 °C for 0.5 ns to allow the system to reach its equilibrium density. Typical system sizes were ~60 Å per side. The systems were then run in the NVT ensemble at 150 °C for 15 ns to equilibrate further. At this point, short time dynamics were captured by saving configurations every 0.1 ps over 200 ps. Production runs were carried out for at least a further 26 ns, saving configurations every 0.02 ns. Final dynamical properties were

calculated for 10 ns of simulation, averaged over the 26 ns production runs using a moving time origin.

The time-dependent radial distribution function $G(r,t)$ for the hydrogens, i.e. the self-part of the van Hove correlation function $G_s(r,t)$, was calculated directly from the MD simulations. The intermediate scattering function $S(Q,t)$ was calculated by Fourier transformation of $G_s(r,t)$:

$$S(Q,t) = \int_0^\infty dr\, G_s(r,t)\, r\sin(Qr)/Q \qquad (2)$$

$S(Q,t)$ was normalized to $S(Q,0) = 1.0$ at high Q.

Results and Discussion

Melt-State Morphology. The temperature-resolved X-ray scattering profiles, the calculated scattering profiles from the MD simulations, and real-space visualizations from the simulations for the three acid-containing polymers are shown in Figure 5.1. Morphological comparisons between experimental and atomistic simulations were made previously[24, 31, 32] with the OPLS force field. Here, the static structure factors $S(q)$ were recalculated from the LOPLS simulations and the results are within the error of the previous OPLS results, confirming the results of the previous studies. The X-ray scattering $I(Q)$ data collected for the three acid-containing polymers in the melt at 150 °C exhibit 2 peaks that demonstrate the nanoscale separation between hydrogen-bonded acid aggregates and the PE matrix. The amorphous halo, centered at $Q \sim 1.35$ Å^{-1}, corresponds to the distribution of PE backbone-backbone distances in the melt. The peak at lower Q corresponds to acid aggregate-aggregate correlation distances and systematically shifts to lower Q with longer PE spacers between acid groups. Figure **5.1** also shows the scattering profiles calculated from the steady-state radial distribution functions in MD

simulations with the LOPLS force field, which exhibits excellent agreement with the X-ray scattering profiles in peak position, relative intensity and peak breadth. Static real-space visualizations (Figure 5.1, right) show only the atoms present in acid aggregates consisting of at least two acid groups, and the different colors represent distinct aggregates. All oxygens and carboxyl hydrogens that are within a certain cutoff distance from each other are considered to belong to the same aggregate. The real space inter-aggregate distances confirm that the low Q peak in $I(Q)$ arises from the spatial separation of the discrete, isolated acid aggregates (aggregate morphology of Type 1 in the nomenclature of our previous work).[24]

The structural heterogeneity of these systems are important to consider when analyzing the dynamics.[5] The dynamic behavior of a polymer changes across different length scales, from very local dynamics including vibrational and rotational motion near the amorphous halo (Q ~ 1.35Å^{-1}), to structural relaxation of the polymer at larger length scales that coincide with those of acid aggregate-aggregate distances (Q ~ 0.3-0.6 Å^{-1}). Therefore, the dynamics across these longer length scales are expected to be correlated with the aggregate morphology.

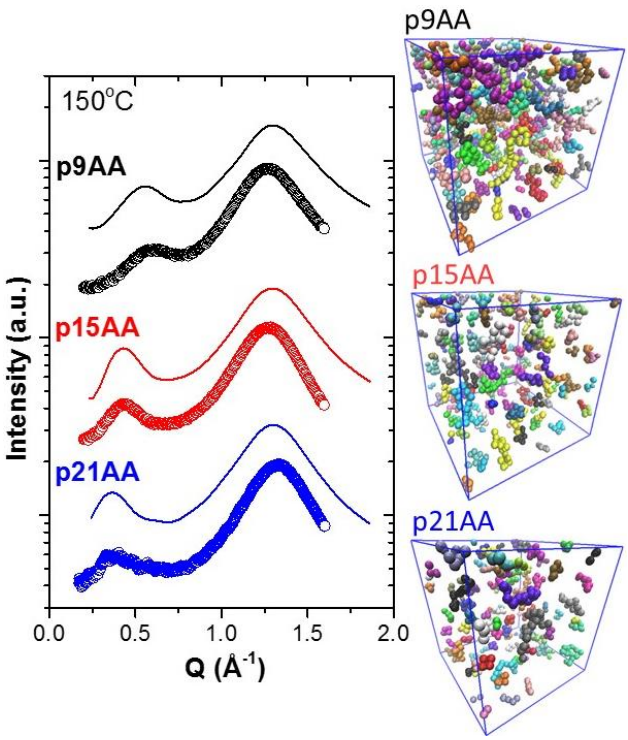

Figure 5.1. Comparisons of morphology from X-ray scattering profiles and atomistic molecular dynamics simulations for precise acid polymers. Left: The scattering profiles collected in the melt state 150°C (points) and the scattering profiles calculated from MD simulations (lines) are plotted. The curves are shifted vertically for clarity. Right: The static real-space visualizations showing only the OOH atoms present in acid aggregates and color distinguishes discrete aggregates.

Dynamics. The normalized intermediate scattering function *S(Q,t)* obtained from the QENS DCS data (points) and the fully atomistic MD simulations (lines) are shown in Figure 5.2. This is the self-motion of hydrogens as a function of time across a large range of length scales (Q = 0.4-2.0 Å^{-1}). The results for both QENS and MD were nearly identical for PE, with only a small deviation at the low-Q values and fast timescales (below 1 ps). Increased acid content leads to slightly more deviation between experiments and simulations at low-Q values. The agreement is excellent at higher-Q values, where both

QENS and atomistic MD capture the presence of a two-step decay and the timescales of these dynamics.

Before fitting *S(Q,t)* to facilitate quantitative analysis, note that there is a systematic trend in *S(Q,t)* as a function of increasing acid content in both the QENS and MD results. The dynamics for all *Q (*0.4-2.0 $Å^{-1}$) become slower and the relaxation profiles become more stretched as the acid content increases from 0% to 9.5% to 22.2 mol% acid. Because the MD data has less noise, captures five orders of magnitude in timescale with the complete decay of *S(Q,t) to ~0*, and exhibits excellent agreement with experimental QENS data, the atomistic MD results will be the focus of our quantitative analysis that follows.

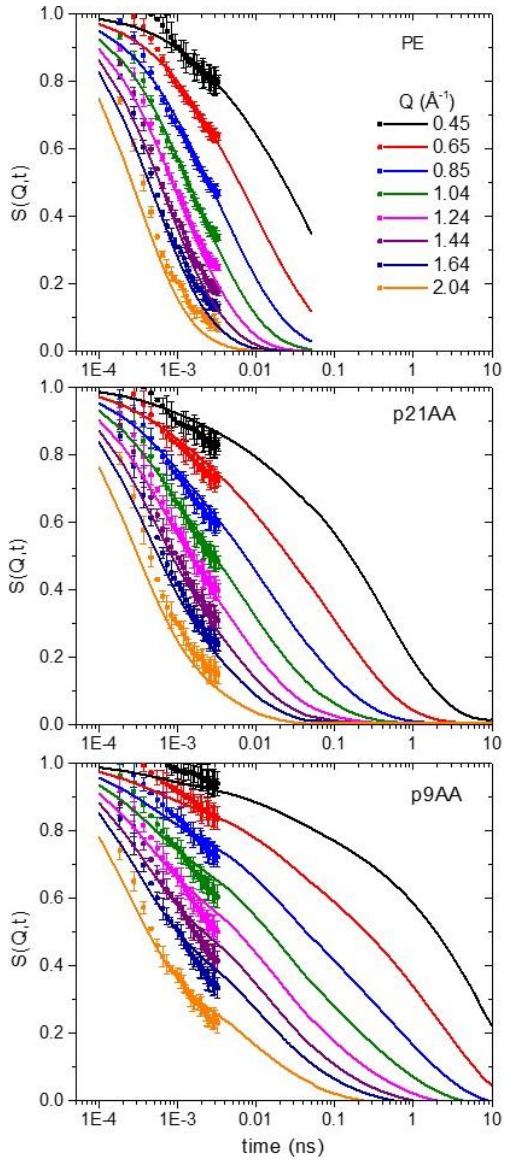

Figure 5.2. The normalized intermediate scattering function *S(Q,t)* calculated for neutron scattering QENS DCS data (points) and MD simulations (lines) for Q= 0.45 – 2.04Å^{-1}. The QENS points were shifted vertically for PE, p21AA and p9AA by 0.05, 0.05 and 0.1, respectively.

KWW Fitting. Previous studies of polymers, including linear polyethylene[10], have shown that their dynamics do not decay exponentially with time and instead can be represented with a stretched exponential such as the Kohlrausch-Williams-Watts (KWW) function. The experimental and simulation *S(Q,t)* data (Figure 5.3) were fit to a single KWW function and it was found that a single decay could not capture the full data set. Therefore we have elected to use two KWW functions (KWW_{slow} and KWW_{fast},) to capture the hydrogen self-dynamics:

$$S(Q,t) = \varphi_{slow} * e^{-\left(\frac{t}{\tau_{slow}}\right)^{\beta_{slow}}} + (1-\varphi_{slow}) * e^{-\left(\frac{t}{\tau_{fast}}\right)^{\beta_{fast}}} \quad (3)$$

Note that two KWW's were needed to capture either the QENS or MD simulation *S(Q,t)* data for PE and all three acid-functionalized polymers (see Appendix E Figure E.5). As mentioned in the methods section the chain ends are omitted in calculating self-dynamics from the simulations and therefore aren't responsible for a second dynamic process.

The fits of Equation 3 to the *S(Q,t)* data from the MD simulations across length scales from the polymer backbone-backbone distances to inter-aggregate distances, and across five orders of magnitude in time scale are shown in Figure 5.3 for p21AA at 150°C. Figure 5.3b illustrates the need to fit the data with two KWW functions, where the fast KWW (red dashes), slow KWW (blue dots), and the total fit (black) are shown. The total fits for all four polymers are shown in Appendix E Figure E.6.

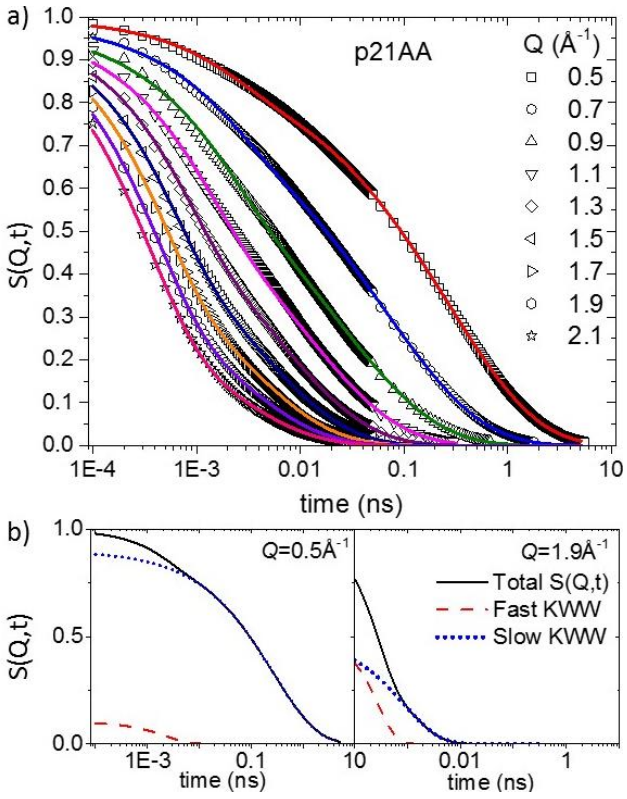

Figure 5.3. a) Representative fits of Equation 3 to simulation-calculated hydrogen *S(Q,t)*. b) Representative contributions of the fast KWW (red dashes) and slow KWW (blue dots) to the total *S(Q,t)* fit (black) for two *Q* values.

Two dynamic processes were confirmed in PE by comparing their time and length scale dependencies. The contribution of slow dynamics, φ_{slow}, to the total dynamics is plotted as a function of length scale (*Q*), in Figure 5.4a. For PE near the amorphous halo (*Q* ~ 1.35 Å^{-1}), the dynamics are dominated by the fast motions while the slow process contributes only ~30%. As longer and longer length scales are considered (smaller *Q*), the slow process contributes more to the total dynamics of the system, reaching ~85% of the dynamics at *Q* ~ 0.4 Å^{-1}. The characteristic timescales (τ_{fast}, τ_{slow}) extracted from the KWW fits are plotted in Figure 5.4b and the stretching parameter (β_{fast}) in Figure 5.4c. The fast

process dominates near the amorphous halo (Q ~ 1.35 Å^{-1}), is weakly Q-dependent, and the stretching parameter (β_{fast}) approaches β~1; these attributes are consistent with the β-process.[7, 8] The slow process was identified as the α-process which dominates at smaller Q-values, has an approximately order of magnitude slower timescale than the β-process, and typically exhibits $\tau \sim Q^{-2/\beta}$ dependency, consistent with the structural relaxation of the chain.[7, 13] Furthermore, the PE KWW fit parameters (τ_{slow} , β_{slow}) compare favorably with previous studies of PE and PE-like oligomers[7, 8, 10, 12, 45, 46] which confirm that the slow process is the structural relaxation of the polymer chain.

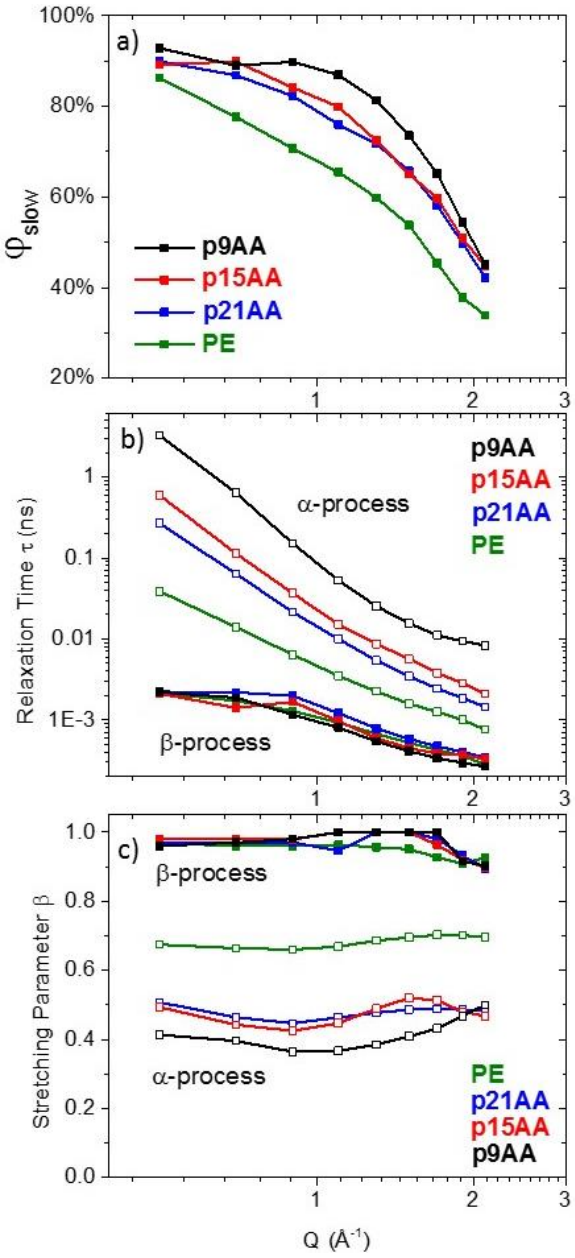

Figure 5.4. Identification of two dynamic processes through the *Q*-dependency of Equation 3 fits to the MD data, namely the α–process (open symbols) and the β–process (closed symbols). a) shows the weight fraction φ_{slow} of slow KWW, b) shows the characteristic timescales and c) shows the stretching parameter as a function of *Q*.

What effect do associating acid groups have on the dynamics of the faster β-process and the slower α-process? It is clear from Figure 5.4a that increasing acid content increases the slow fraction, φ_{slow}, of hydrogen motion at a given *Q*. Selecting an intermediate length scale of Q=1.5Å^{-1}, φ_{slow} for PE (0 mol% AA) is 55% whereas p9AA (22.2 mol% AA) has 85% slow dynamics. At very low-*Q*, near the inter-acid aggregate length scales, all four compositions approach ~90% slow dynamics, indicating that fast, local dynamics continue to contribute ~10% to the total measured dynamics independent of composition at 150°C. As seen in Figure 5.4b, the presence of acid groups slows the α-process timescale (τ_{slow}) of the backbone by up to 2 orders of magnitude relative to PE of similar M_w. τ_{fast} is nearly identical for all four polymers, consistent with dynamics without correlation effects. Furthermore, the stretching parameter, β_{slow}, an indication for heterogeneity in the timescale of relaxation dynamics, decreases with higher acid content, Figure 5.4c. Decreased β_{slow} indicates that the H-bonded groups lead to greater diversity in the timescale of the α-process. It should be noted that Rouse-like motion is only beginning at these timescales at low-*Q* indicated through higher power-law dependence ($\tau \sim Q^{-4}$, $\beta \sim 1$).[10] The polymers have not entered the Fickian diffusion regime yet as confirmed by the mean square displacement (MSD) of hydrogens in Figure 5.5; the fastest polymer is PE PE with an MSD ≈ $t^{0.65}$ at the longest times shown.

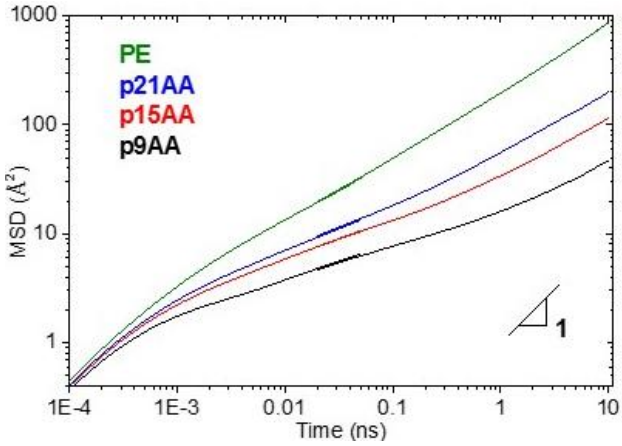

Figure 5.5. The MSD for hydrogens between acid groups (hydrogens at chain ends are omitted) at T = 150°C. The MSD slopes confirm pre-diffusive dynamics for all 4 polymers at these timescales. Acid functionalized polymers show suppressed MSD slopes relative to PE below 1 ns.

Overall, the H-bonding acid groups perturb the chain dynamics through increased fractions of slow-moving polymer, extending the timescale of the α-process by up to 2 orders of magnitude in time at smaller *Q*, and increased dynamical heterogeneity of the α-process. Meanwhile, the faster β-process is weakly *Q*-dependent and is consistent with local motions of the hydrogen along PE backbone.

The Effect of Structural Heterogeneity on Chain Dynamics. Figure 5.5 shows the average hydrogen MSD for each of the four polymers, and demonstrates the overall slowing effect of acid content on polymer dynamics. The dynamics of specific hydrogens along the linear PE backbone were also directly calculated from the simulations, Figure 5.6. Figure 5.6a indicates our numbering scheme, where the hydrogens bonded to the backbone carbon with the pendant AA group are termed H-type #1, the hydrogens on

the adjacent backbone carbons are labeled #2, and forth with the H-type numbers increasing until the midpoint of the alkyl spacer is reached. Therefore the hydrogens furthest from the acid group in p9AA, p15AA and p21AA are H-types 5, 8 and 11, respectively. Figure **5.6**b shows the MSD for each of the different hydrogen types for three timescales.

The hydrogens nearest the acid groups have the lowest MSDs while hydrogens toward the middle of the alkyl spacer have larger MSDs.[20, 21] This effect is proportionately largest at time scales below those of the α-process, where the four hydrogens nearest the pendant acid group are significantly impacted (τ = 0.01 and 0.1 ns). At longer timescales of 2 ns, the MSD for all hydrogen types along the chain become nearly identical (within +/- 5% of average). The acid aggregates exist at all times, as confirmed through structural characterization, however after ~2 ns the acid aggregates have moved in space and have exchanged acid groups between aggregates. Figure 5.6c shows this rearrangement of the OOH atoms in aggregates in p21AA, where at *t* = 0 ns each aggregate is a separate color and after the simulation runs 0.1 ns a slight degree of aggregate motion and acid group exchange is observed (the atoms maintain the original *t* = 0 ns color). At *t* = 2 ns significant aggregate motion and acid group exchange is observed. This implies that the dynamics of atoms in the middle of the spacers (“bridge atoms”) can be substantially faster than the dynamics of the hydrogens near the acid groups (“anchors”), but all the hydrogens remain restricted in translational motion until acid aggregates rearrange. The dynamics are most strongly affected for the four H-types nearest the acid groups, with decreased impact on MSD when acid aggregates begin to rearrange (~2 ns). The effect of acid mole fraction, however, plays a large role in the magnitudes of the MSDs. At 2 ns in p21AA, having approximately half the acid content than that of p9AA (22.2 mol% vs 9.5 mol%,

respectively), hydrogens have traveled ~4x further than those of p9AA. From the KWW fitting at Q = 0.5 Å^{-1}, the characteristic timescales for the α-process in p21AA and p9AA are 0.27 ns and 3.28 ns, respectively, over 10x faster for the longer spacer. The effect of varied spacer length and the onset of acid-aggregate rearrangement are notably different than those reported in PEO-Na ionomers at ~70 °C, which continued to have strong anchored dynamics near ionic aggregates even at longer timescales (50 ns), longer bridge sections (38 atoms) and with more flexible carbon-oxygen bonding within the chain.[20, 47, 48]

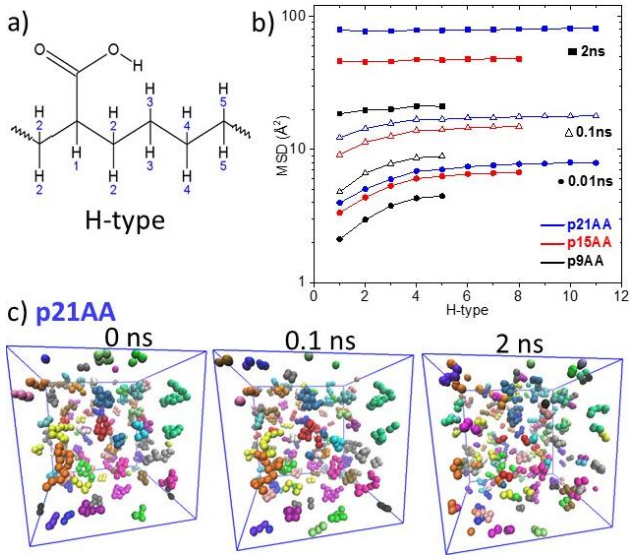

Figure 5.6. a) Schematic indicating the naming scheme for hydrogen location along the backbone. b) The MSD shows the α-process is “anchored” near acid groups while bridge atoms have higher mobility. c) Real-space snapshots of the acid aggregates in p21AA at three time points. At 0 ns all OOH atoms in each aggregate are color coded. At later time points the rearrangement of these atoms can be observed indicated through mixing of the colored acidic groups.

How do hydrogens, as a function of proximity to an acid group, contribute to the α–process? The intermediate scattering function *S(Q,t)* is shown for p21AA and p9AA at four *Q* values in Figure 5.7a. The solid line is the average hydrogen motion <H>, as shown previously in Figure 5.2. The *S(Q,t)* were also calculated for H1 atoms and for the hydrogen furthest from an acid group, H11 and H5, respectively. The data were fit with two dynamic processes as before (the slower α-process and the faster, localized motion of the β-process) and a comparison of the KWW fitting parameters are shown in Figure 5.7b, c, and d.

The average hydrogen self-dynamics <H>, as expected, fall in-between the near-anchor H1 and the faster bridge hydrogens H11/H5. The *S(Q,t)* data for the anchors are significantly different than the average, with a larger effect in p9AA than p21AA. The fraction of dynamics arising from the α-process, φ_{slow} seen in Figure 5.7b, shows a similar trend for all H-types suggesting acid content has a minor effect on the length scale at which the α-process begins to contribute strongly to the dynamics and at large length scales the α-process contributes ~90% of the total dynamics. Near the amorphous halo (Q ~ 1.35Å^{-1}) both bridge and anchor H-types behave similarly, where these dynamics are dominated by the β-process.

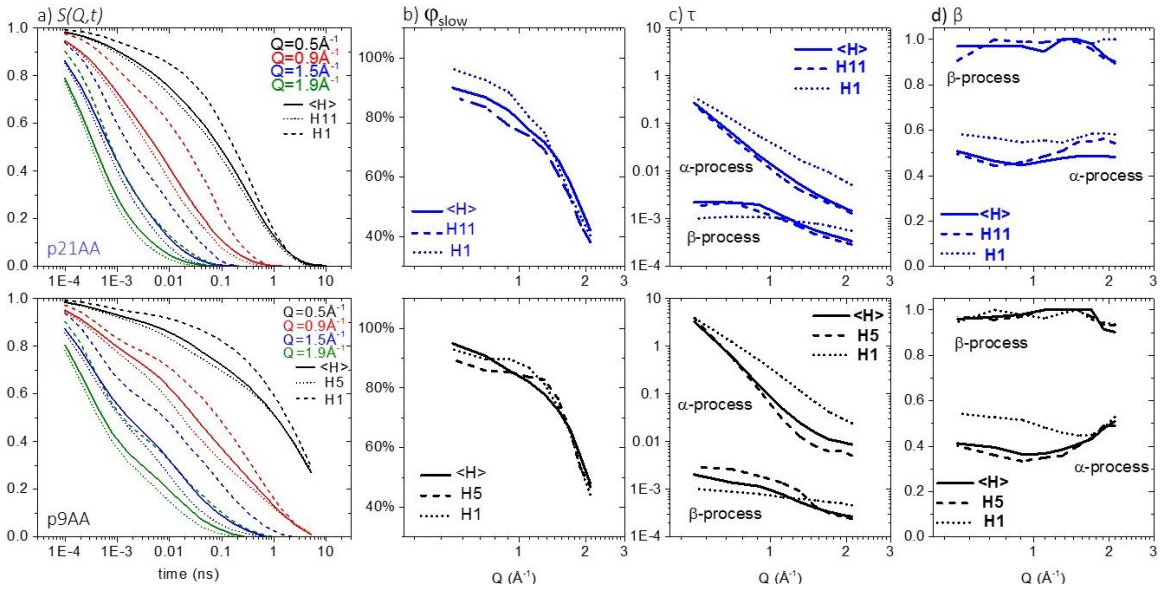

Figure 5.7. a) Comparison of the average <H>, near-acid and bridge H-Type dynamics for p21AA (top row) and p9AA (bottom row). b, c and d show the extracted fit parameters to Equation 3.

Figure 5.7c shows the characteristic relaxation time scales for the α-process. The <H> dynamics closely resemble the faster and more numerous bridge atoms. The time scales for all three H-types converge at low-*Q* where acid aggregate lifetime likely plays a role, as was the case in the MSDs (Figure 5.6b). The relaxation times for H1 at high *Q* are nearly an order of magnitude slower than other H-types located just 4 carbons away on the same backbone, which suggests strong coupling of these hydrogens with the dynamics of the acid aggregate rearrangement. An interesting note is that the heterogeneity, represented through the stretching parameter β in Figure 5.7d, indicates that the faster <H> and H5 type hydrogens are more heterogeneous (lower β) than the slow H1 type in p9AA. All H-types in the acid polymers exhibit more dynamical

heterogeneity than that of linear PE, but the slower H1 type, whose dynamics is coupled to the acid aggregates, has the least stretched relaxation function.

Note that some variability in fitting φ_{slow} can be observed at lower *Q* in p9AA Figure 5.7b, where the <H> does not always fall in-between the bridge and anchor H-types. This is due to less-perfect fitting of the *S(Q,t)* data for p9AA H1 type in Figure 5.7a. The authors speculate the inability to fit two KWW functions is due to the presence of another dynamic process in this high acid content sample, similar to the appearance of the α_2-process in ionomer systems. While this observation may suggest the need for another relaxation mechanism to perfectly fit the data, for comparison among all the systems, only two dynamic processes were used here.

Conclusions

The melt state dynamics for a series of acid-containing polymers were investigated as a function of precise spacing between pendant acid groups on a linear polyethylene (PE) chain. The pendant acid groups form hydrogen-bonded acid aggregates that nanoscale phase separate from the PE matrix. The melt-state morphology found through X-ray scattering experiments and fully atomistic MD simulations are in good agreement across large length scales. The dynamics of this nanoscale heterogeneous system were investigated through both quasi-elastic neutron scattering (QENS) experiments and fully atomistic molecular dynamics (MD) simulations. The experimental and simulated dynamics, as compared using the intermediate scattering function *S(Q,t)*, were found to be in excellent agreement.

The dynamics from picosecond to nanosecond timescales reveal two dynamic processes with dependence on composition and length scale (*Q*). The faster dynamics

were indicative of spatially-restricted motions, suggestive of the β-process corresponding to bond rotations and hydrogen vibrations, whereas the slower dynamics were identified as the α-process corresponding to structural relaxation and segmental motion of the polymer backbone. Increased acid content, or shorter PE spacers between side groups, slows the characteristic structural relaxation timescale (τ_α increases by 100X relative to PE at Q = 0.5 $Å^{-1}$), and introduces greater dynamic heterogeneity (β_α decreases from ~0.7 to ~0.4 for PE and p9AA). The role of proximity of hydrogen atoms in the backbone to an acid group revealed significant dynamic heterogeneity between bridge and anchor regions of the chain, even when the spacer possesses only 9 carbons. The near-aggregate anchored segments display self-dynamics of up to an order of magnitude slower than the bridge regions, just four methylene groups away. Despite significant dynamical heterogeneity at the nanoscale, the average structural relaxation dynamics, the α-process, were still able to be fit with a single stretched exponential form.

This study has shown that the structural heterogeneity imposed by associating pendant groups leads to dynamic heterogeneity of the polymer backbone, specifically with slower dynamics near the anchored H-bonding acid groups. Confirming that the acid-functionalized polymer dynamics were accurately captured by atomistic MD simulations builds the foundation on which to study the dynamics of ion-containing polymers, which are associated more strongly.

References

1. Soles, C. L.; Douglas, J. F.; Lin, E. K.; Lenhart, J. L.; Jones, R. L.; Wu, W.-L.; Goldfarb, D. o. L.; Angelopoulos, M. Incoherent neutron scattering and the dynamics of thin film photoresist polymers. *Journal of Applied Physics* **2003,** 93, (4), 1978-1986.

2. Rubinstein, M.; Colby, R. H.; Dobrynin, A. V. Dynamics of Semidilute Polyelectrolyte Solutions. *Physical Review Letters* **1994,** 73, (20), 2776-2779.

3. Semenov, A. N.; Rubinstein, M. Dynamics of Entangled Associating Polymers with Large Aggregates. *Macromolecules* **2002,** 35, (12), 4821-4837.

4. Ratner, M. A.; Shriver, D. F. Ion transport in solvent-free polymers. *Chemical Reviews* **1988,** 88, (1), 109-124.

5. Agrawal, A.; Perahia, D.; Grest, G. S. Cluster Morphology-Polymer Dynamics Correlations in Sulfonated Polystyrene Melts: Computational Study. *Physical Review Letters* **2016,** 116, (15), 158001.

6. Materials Genome Initiative for Global Competitiveness. *Materials Genome Initiative for Global Competitiveness* **2011**.

7. Smith, G. D.; Paul, W.; Monkenbusch, M.; Richter, D. A comparison of neutron scattering studies and computer simulations of polymer melts. *Chemical Physics* **2000,** 261, (1–2), 61-74.

8. Morhenn, H.; Busch, S.; Unruh, T. Chain dynamics in a hexadecane melt as seen by neutron scattering and identified by molecular dynamics simulations. *Journal of physics. Condensed matter : an Institute of Physics journal* **2012,** 24, (37), 375108.

9. Smith, G. D.; Bedrov, D. Relationship between the α- and β-relaxation processes in amorphous polymers: Insight from atomistic molecular dynamics simulations of 1,4-polybutadiene melts and blends. *Journal of Polymer Science Part B: Polymer Physics* **2007,** 45, (6), 627-643.

10. Arbe, A.; Colmenero, J. Characterization of the “simple-liquid” state in a polymeric system: Coherent and incoherent scattering functions. *Physical Review E* **2009,** 80, (4).

11. Arialdi, G.; Ryckaert, J.-P.; Theodorou, D. N. On the separation between torsion–vibration and conformational relaxation processes in the incoherent intermediate scattering function of polyethylene. *Chemical Physics* **2003,** 292, (2-3), 371-382.

12. Smith, G. D.; Paul, W.; Yoon, D. Y.; Zirkel, A.; Hendricks, J.; Richter, D.; Schober, H. Local dynamics in a long-chain alkane melt from molecular dynamics simulations and neutron scattering experiments. *The Journal of Chemical Physics* **1997,** 107, (12), 4751.

13. Boyd, R. H.; Gee, R. H.; Han, J.; Jin, Y. Conformational dynamics in bulk polyethylene: A molecular dynamics simulation study. *The Journal of Chemical Physics* **1994,** 101, (1), 788-797.

14. Genix, A. C.; Arbe, A.; Colmenero, J.; Wuttke, J.; Richter, D. Neutron Scattering and X-ray Investigation of the Structure and Dynamics of Poly(ethyl methacrylate). *Macromolecules* **2012,** 45, (5), 2522-2536.

15. Agrawal, A.; Perahia, D.; Grest, G. S. Clustering effects in ionic polymers: Molecular dynamics simulations. *Physical Review E* **2015,** 92, (2), 022601.

16. Ruan, D.; Simmons, D. S. Glass Formation near Covalently Grafted Interfaces: Ionomers as a Model Case. *Macromolecules* **2015,** 48, (7), 2313-2323.

17. Triolo, A.; Arrighi, V.; Triolo, R.; Passerini, S.; Mastragostino, M.; Lechner, R. E.; Ferguson, R.; Borodin, O.; Smith, G. D. Dynamic heterogeneity in polymer electrolytes. Comparison between QENS data and MD simulations. *Physica B: Condensed Matter* **2001,** 301, (1–2), 163-167.

18. Choi, U. H.; Middleton, L. R.; Soccio, M.; Buitrago, C. F.; Aitken, B. S.; Masser, H.; Wagener, K. B.; Winey, K. I.; Runt, J. Dynamics of Precise Ethylene Ionomers Containing Ionic Liquid Functionality. *Macromolecules* **2015,** 48, (2), 410-420.

19. Liu, H.; Paddison, S. J. Direct Comparison of Atomistic Molecular Dynamics Simulations and X-ray Scattering of Polymerized Ionic Liquids. *ACS Macro Letters* **2016,** 5, (4), 537-543.

20. Lin, K.-J.; Maranas, J. K. Cation Coordination and Motion in a Poly(ethylene oxide)-Based Single Ion Conductor. *Macromolecules* **2012,** 45, (15), 6230-6240.

21. Lin, K.-J.; Maranas, J. K. Does decreasing ion-ion association improve cation mobility in single ion conductors? *Physical Chemistry Chemical Physics* **2013,** 15, (38), 16143-16151.

22. Baughman, T. W.; Chan, C. D.; Winey, K. I.; Wagener, K. B. Synthesis and Morphology of Well-Defined Poly(ethylene-co-acrylic acid) Copolymers. *Macromolecules* **2007,** 40, (18), 6564-6571.

23. Buitrago, C. F.; Alam, T. M.; Opper, K. L.; Aitken, B. S.; Wagener, K. B.; Winey, K. I. Morphological Trends in Precise Acid- and Ion-Containing Polyethylenes at Elevated Temperature. *Macromolecules* **2013,** 46, (22), 8995-9002.

24. Buitrago, C. F.; Bolintineanu, D. S.; Seitz, M. E.; Opper, K. L.; Wagener, K. B.; Stevens, M. J.; Frischknecht, A. L.; Winey, K. I. Direct Comparisons of X-ray Scattering and Atomistic Molecular Dynamics Simulations for Precise Acid Copolymers and Ionomers. *Macromolecules* **2015,** 48, (4), 1210-1220.

25. Buitrago, C. F.; Jenkins, J. E.; Opper, K. L.; Aitken, B. S.; Wagener, K. B.; Alam, T. M.; Winey, K. I. Room Temperature Morphologies of Precise Acid- and Ion-Containing Polyethylenes. *Macromolecules* **2013,** 46, (22), 9003-9012.

26. Hall, L. M.; Seitz, M. E.; Winey, K. I.; Opper, K. L.; Wagener, K. B.; Stevens, M. J.; Frischknecht, A. L. Ionic aggregate structure in ionomer melts: effect of molecular architecture on aggregates and the ionomer peak. *Journal of the American Chemical Society* **2012,** 134, (1), 574-87.

27. Hall, L. M.; Stevens, M. J.; Frischknecht, A. L. Effect of Polymer Architecture and Ionic Aggregation on the Scattering Peak in Model Ionomers. *Physical Review Letters* **2011,** 106, (12).

28. Hall, L. M.; Stevens, M. J.; Frischknecht, A. L. Dynamics of Model Ionomer Melts of Various Architectures. *Macromolecules* **2012,** 45, (19), 8097-8108.

29. Ting, C. L.; Stevens, M. J.; Frischknecht, A. L. Structure and Dynamics of Coarse-Grained Ionomer Melts in an External Electric Field. *Macromolecules* **2015,** 48, (3), 809-818.

30. Bolintineanu, D. S.; Stevens, M. J.; Frischknecht, A. L. Atomistic Simulations Predict a Surprising Variety of Morphologies in Precise Ionomers. *ACS Macro Letters* **2013,** 2, (3), 206-210.

31. Bolintineanu, D. S.; Stevens, M. J.; Frischknecht, A. L. Influence of Cation Type on Ionic Aggregates in Precise Ionomers. *Macromolecules* **2013,** 46, (13), 5381-5392.

32. Lueth, C. A.; Bolintineanu, D. S.; Stevens, M. J.; Frischknecht, A. L. Hydrogen-bonded aggregates in precise acid copolymers. *J Chem Phys* **2014,** 140, (5), 054902.

33. Siu, S. W. I.; Pluhackova, K.; Böckmann, R. A. Optimization of the OPLS-AA Force Field for Long Hydrocarbons. *Journal of Chemical Theory and Computation* **2012,** 8, (4), 1459-1470.

34. Frischknecht, A. L.; Todd, M. A.; Azoulay, J.; Bolintineanu, D. S.; Cordaro, J. G.; Hall, L. M.; Jenkins, J. E.; Lueth, C. A.; Murtagh, D.; Rempe, S. L. B.; Stevens, M. J.

Effects of Morphology on Ion Transport in Ionomers for Energy Storage; SAND2012-8304; Sandia National Laboratories: Sandia Rerport, 2012.

35. Middleton, L. R.; Szewczyk, S.; Azoulay, J.; Murtagh, D.; Rojas, G.; Wagener, K. B.; Cordaro, J.; Winey, K. I. Hierarchical Acrylic Acid Aggregate Morphologies Produce Strain-Hardening in Precise Polyethylene-Based Copolymers. *Macromolecules* **2015,** 48, (11), 3713-3724.

36. O'Gara, J. E.; Wagener, K. B.; Hahn, S. F. Acyclic diene metathesis (ADMET) polymerization. Synthesis of perfectly linear polyethylene. *Die Makromolekulare Chemie, Rapid Communications* **1993,** 14, (10), 657-662.

37. Heiney, P. Datasqueeze: A Software Tool for Powder and Small-Angle X-Ray Diffraction Analysis. *Commission on Powder Diffraction Newsletter* **2005**, (32), 9-11.

38. Azuah, R. T.; Kneller, L. R.; Qiu, Y.; Tregenna-Piggott, P. L. W.; Brown, C. M.; Copley, J. R. D.; Dimeo, R. M. DAVE: A comprehensive software suite for the reduction, visualization, and analysis of low energy neutron spectroscopic data. *Journal of Research of the National Institute of Standards and Technology* **2009,** 114, (6), 341-358.

39. Jorgensen, W. L.; Maxwell, D. S.; TiradoRives, J. Development and testing of the OPLS all-atom force field on conformational energetics and properties of organic liquids. *Journal of the American Chemical Society* **1996,** 118, (45), 11225-11236.

40. Price, M. L. P.; Ostrovsky, D.; Jorgensen, W. L. Gas-phase and liquid-state properties of esters, nitriles, and nitro compounds with the OPLS-AA force field. *J Comput Chem* **2001,** 22, (13), 1340-1352.

41. Pluhackova, K.; Morhenn, H.; Lautner, L.; Lohstroh, W.; Nemkovski, K. S.; Unruh, T.; Böckmann, R. A. Extension of the LOPLS-AA Force Field for Alcohols, Esters, and Monoolein Bilayers and its Validation by Neutron Scattering Experiments. *The Journal of Physical Chemistry B* **2015,** 119, (49), 15287-15299.

42. Plimpton, S. Fast parallel algorithms for short-range molecular dynamics. *J. Comp. Phys.* **1995,** 117, (1), 1-19.

43. in 't Veld, P. J.; Rutledge, G. C. Temperature-Dependent Elasticity of a Semicrystalline Interphase Composed of Freely Rotating Chains. *Macromolecules* **2003,** 36, (19), 7358-7365.

44. Clifford, S.; Bolton, K.; Ramjugernath, D. Monte Carlo simulation of carboxylic acid phase equilibria. *The Journal of Physical Chemistry B* **2006,** 110, (43), 21938-21943.

45. Arrighi, V.; Tanchawanich, J.; Telling, M. T. F. Molar Mass Dependence of Polyethylene Chain Dynamics. A Quasi-Elastic Neutron Scattering Investigation. *Macromolecules* **2013,** 46, (1), 216-225.

46. Unruh, T.; Smuda, C.; Busch, S.; Neuhaus, J.; Petry, W. Diffusive motions in liquid medium-chain n-alkanes as seen by quasielastic time-of-flight neutron spectroscopy. *J Chem Phys* **2008,** 129, (12), 121106.

47. Lin, K. J.; Maranas, J. K. Does decreasing ion-ion association improve cation mobility in single ion conductors? *Physical chemistry chemical physics : PCCP* **2013,** 15, (38), 16143-51.

48. Lin, K.-J.; Li, K.; Maranas, J. K. Differences between polymer/salt and single ion conductor solid polymer electrolytes. *RSC Advances* **2013,** 3, (5), 1564.

CHAPTER 6

Conclusions and Future Work

Conclusions

This thesis about precise polymers has furthered the understanding of the structure – processing – morphology - property relationships of acid and ionic functionalized polymers. Improvements in synthetic techniques and advancements in characterization methods have enabled new studies of acid- and ionic-functionalized, associating polymer systems. The precise polymers are entangled, high molecular weight, linear polyethylenes (PE) functionalized with interacting pendant groups (acidic or ionic) placed periodically along the polymer backbone. Connecting nano-scale morphologies to bulk properties, real-time X-ray scattering and tensile deformation at a range of temperatures captured transient morphologies and elucidated their relationship with strain hardening. At time scales and length scales of polymer and aggregate dynamics, foundational experimental and computer simulation studies extended the knowledge of the molecular-level morphology in aggregated polymer systems to dynamics, providing a baseline for future studies of ion-conduction associating polymer melts.

In Chapter 2 we report tensile testing and *in situ* X-ray scattering measurements of a homologous series of precise poly(ethylene-*co*-acrylic acid) copolymers (p*x*AA). The number of backbone carbons (*x*) between pendant acrylic acid groups along the polyethylene chain (*x* = 9, 15, 21) has a pronounced effect on both their tensile properties as well as their morphologies during deformation. The semi-crystalline precise copolymer (p21AA) displays yielding behavior similar to polyethylene. Also, strain hardening in p21AA coincides with the originally isotropic acid-rich layered morphologies strongly aligning with acid layers perpendicular to the strain direction, demonstrating the facile

nature of H-bonding within the acid aggregates. When the alkyl spacer is only nine carbons (p9AA), the precise copolymer withstands strains of > 1000% without failing, because the liquid-like assembly of acid aggregates permits the acid groups to exchange without developing substantial anisotropy in the structure. Both p21AA and p9AA maintain their morphology type during deformation with considerable plastic deformation and only modest increase in their interaggregate distances. In contrast, p15AA exhibits a structural transformation from nominally spherical to layered aggregate morphologies during tensile deformation as evidenced by higher order peaks at intermediate scattering angles and larger interaggregate spacing, coinciding with substantial strain hardening. This morphological change in p15AA is particularly sensitive to the strain rate, because the relaxation times of the PE segments and the acid aggregates are accessible at room temperature. This was the first report of an amorphous precise polymer forming a layered morphology. Commensurate with this morphology transformation, p15AA is the toughest of the precise poly(ethylene-*co*-acrylic acid) copolymers.

Chapter 3 is an extension of Chapter 2 wherein the role of acid periodicity and acid chemistry are examined. We report the morphology evolution under tensile deformation for strictly linear polyethylenes with associating functional groups with either precise or pseudo-random periodicity. *In situ* X-ray scattering measurements during elongation reveal that periodic acid group placement along the backbone is required to form hierarchical layered morphologies that coincides with strain hardening. This phenomenon was observed in both semi-crystalline (21 carbon spacer) and amorphous (15 carbon spacer) precise acid polyethylenes with acrylic, geminal acrylic and phosphonic acids. Polymers with non-periodic (pseudo-random) acid placement fail to form layered morphologies and instead retain a liquid-like distribution of nominally spherical acid

aggregates. These results broadly indicate that hierarchical acid-rich layered structures, commensurate with improved mechanical properties, form in polymers with strictly periodic chemical structures and sufficient chain mobility for chain alignment during elongation. This was the first report of p15PA exhibiting a layered morphology through elevated temperature deformation. Finally, precise polyethylenes with more strongly associating functional groups had higher modulus.

In Chapter 4 the morphology evolution during deformation was characterized for a series of partially lithium-neutralized, precise acrylic acid polyethylenes. *In situ* X-ray scattering measurements simultaneously captured the changes in the inter-aggregate peak and amorphous halo during uniaxial elongation. The role of spacing between acid groups along the linear PE backbone (the number of carbons between pendant groups), fraction of neutralized acid groups, and effect of temperature were examined. This study indicates that the neutralization of the acid-functionalized precise polymers with metal salts significantly increases the thermal transitions and mechanical properties, however, the morphologies remain controlled by the polymer structure. In the melt state the highest acid and ionic content lead to the largest tensile strength due to the long-lived ionic aggregates. Strain hardening was observed when significant chain orientation occurred corresponding with an anisotropic layered morphology, indicating some chain mobility through facile aggregate exchange at elevated temperature. Interestingly, even the ionomer with the shortest methylene spacer, p9AA-35%Li, forms a layered morphology during deformation at elevated temperature ($T > T_g$) when the ionic aggregates are long-lived.

In Chapter 5 melt state dynamics were investigated for a series of strictly linear polyethylenes with associating functional groups. The periodic pendant acrylic acid groups form hydrogen-bonded acid aggregates within the polyethylene (PE) matrix. The dynamics of these nanoscale heterogeneous morphologies were investigated from picosecond to nanosecond timescales by both quasi-elastic neutron scattering (QENS) experiments and fully atomistic molecular dynamics (MD) simulations. The faster dynamic processes are compositionally insensitive and indicative of spatially-restricted local motions, suggestive of the β-process in PE. The slower dynamic processes are highly composition dependent and indicate the structural relaxation of the polymer backbone. Higher acid contents, or shorter PE spacers between pendant acid groups, slow the structural relaxation timescale and introduce greater dynamic heterogeneity. Furthermore, the dynamics of specific hydrogen atom positions along the backbone correlate structural heterogeneity imposed by the acid aggregates with segmental dynamics. At short time intervals (< 2ns), the mean square displacements for the four methylene groups closest to the acid groups are up to ten times smaller than methylene groups further from the acid groups. At longer timescales acid aggregates translate and rearrange, and the dynamics of the hydrogens near and far from the acid groups converge. The characterization of the nanoscale chain dynamics in associating polymer systems has implications on our understanding of dynamic heterogeneity in polymers, validation of simulations force fields, and highlights the type of dynamics potentially missing in united-atom simulations.

Future Work

This thesis has focused on correlating the structure – morphology – properties in nano-aggregated associating polymer systems. Still, there remains a tremendous amount of work in characterizing and manipulating the ionic aggregates from both experimental

and theoretical viewpoints. The variety of aggregate shapes predicted in MD simulations have yet to be experimentally proven to exist. It is hypothesized that certain aggregate shapes, like block copolymer morphologies, will lead to anisotropic properties and can be predicted and controlled to improve mechanical or transport properties. The effect of ionic aggregates must be considered at a variety of length scales, time scales, temperatures, and external fields to understand how aggregate shapes impact properties. Here, we discuss several potential directions to extend the studies presented in this thesis towards characterizing and designing ionic aggregate shapes to tune bulk properties. First, is quantifying the nano-scale dynamics experimentally (QENS) and validating computer simulation force fields to understand the local polymer and cation dynamics in polymer melts. Secondly, rheological characterization in the linear and non-linear regime for a series of aggregate shapes is proposed. Finally, dielectric spectroscopy measurements would enable complementary viewpoints to the rheology with a focus on dipolar behavior rather than viscoelastic response. These three methods, combined, would access the response from glassy to melt state, and at a variety of length scales and time scales, which could elucidate how aggregate shape impacts properties in these specific polymers, and more generally identify mechanisms broadly applicable to associating polymers systems.

Characterization of polymer dynamics in precise Li^+ ionomers through QENS. Quasi-elastic neutron scattering (QENS) measurements were conducted in the melt state on lithium neutralized precise ionomers. These data can be compared with fully atomistic molecular dynamics simulations as demonstrated in Chapter 5 on the unneutralized acid-containing polymer forms. While the QENS data is almost exclusively sensitive to the polymer chain dynamics, the atomistic view from simulations provides real-space

observation of ion dynamics within and between aggregates in addition to the polymer dynamics.

Comparisons between the experimental data and the simulations are already underway. Figure 6.1, left, shows a comparison of the simulated intermediate scattering function *S(Q,t)* for an unneutralized polymer (shown in Chapter 5) compared with a partially Li-neutralized polymer. As expected from the increase in T_g observed in DSC, the addition of lithium ions decreases the polymer chain dynamics. Furthermore, the higher acid- and ion-content compositions shows a greater decrease in dynamics upon neutralization.

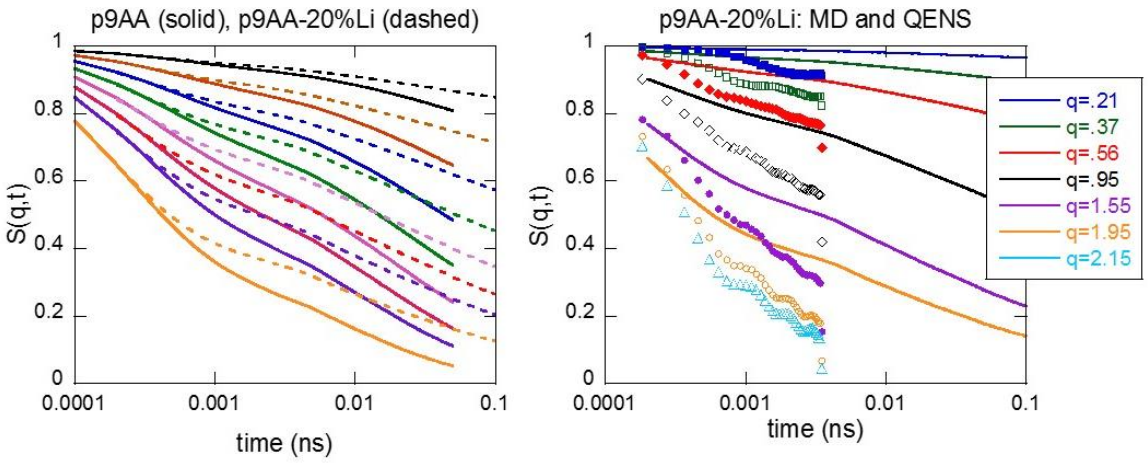

Figure 6.1. Left, S(Q,t) calculated from atomistic MD simulations for the acid (solid) and ionomer (dashed) forms at 150°C. Different lines indicate different Q-values, going from top to bottom: Q=0.45, 0.65, 0.85, 1.04, 1.24, 1.44, 1.64, 2.04 $Å^{-1}$. Right, S(Q,t) comparison between atomistic MD simulations LLOPLS force field (l*ines) and for the QENS (points)* at 150°C. Note that the oscillations in the experimental data are likely artifacts from non-optimized conditions during the Fourier transformation.

A comparison of the QENS experimental data with simulation results for ionomers reveal substantial discrepancies in the dynamic behavior, as seen in Figure 6.1 right. This suggests the force-field used in calculating the dynamics in the simulations may be inaccurate, or, that some of the dynamics captured in the QENS experiments are substantially faster than the polymer motions and enhancing the overall dynamics of the system. A recent publication showed a similar discrepancy where the dynamics in a PEO-sulfonated isophthalate ionomer was compared between QENS and course grained computer simulations.[7] The discrepancy between the dynamics of the two techniques indicated that reduced charges in simulations could improve the agreement with QENS.

Further work must be done to identify the origin of the discrepancy in the precise lithium and acrylic acid system prior to extracting the motions of the polymer or ions through KWW fitting methods. The importance of having a validated model is that a greater number of material systems and compositions can been investigated. Materials can be designed and evaluated to produce desired properties even before being synthesized, providing critical target points when synthesizing new materials.

Rheological characterization of precise acid polymers and ionomers. The viscoelastic properties of associating polymers are complex and remain poorly understood in both the linear (LVE) and non-linear viscoelastic response regimes. The time- and temperature- dependent transient networks formed through secondary bonding are further obfuscated by having poor or unknown distributions of the associating groups within the materials. Precise acid- and ion-containing polymers provide model materials to understand the viscoelastic response in associating polymers. Within the LVE region the various relaxations range from monomeric relaxations, to aggregate relaxations. Furthermore these data can be modeled with Rouse dynamics at low molecular weights, or compared to current models for associating polymers, especially the sticky-Rouse models, to test for validity in these systems.[1-5] Non-linear viscoelastic response enables substantial chain orientation, and might provide two opportunities. Firstly, the mechanical response of aggregates breaking and reforming might be different depending on aggregate shape. Secondly, within the steady state deformation regime, more exact analysis of chain orientation and morphology evolution may be accessed as a function of strain rate and temperature. These behaviors may be analogous to those measured in uniaxial tensile deformation discussed in Chapters 2-4. Furthermore, synchrotron techniques exist that enable morphological characterization *in situ*.

Preliminary investigations are already underway by Dr. Frank Snijkers (Solvay, France) on pseudo-random acid copolymers listed in Table 6.1. Oscillatory shear LVE rheology experiments were conducted on varied sample sizes (10-70 mg) and confirm reproducibility and accuracy of these small quantity rheology measurements. Small strain amplitude oscillatory shear measurements using a strain-controlled ARES-rheometer (TA Instruments, US) equipped with a parallel plate geometry showed repeatable test results and no evidence of degradation when run under nitrogen environment from the melting temperature T_m up to 180 °C.

Table 6.1. Molecular characteristics and summary of calorimetric analysis of the test samples. These copolymers were synthesized by T. Baughman in K. Wagener's group.

Sample Name	**Chemical structure**	**M_n (kg/mol) GPC**	**PDI GPC**	**T_g (°C) DSC**	**T_m (°C) DSC**
ADMET PE	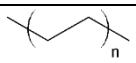	44.9	1.8	-	129
r45AA	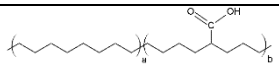	93.6	1.37	-	101
r21AA	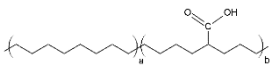	85.4	1.41	11	86
r15AA	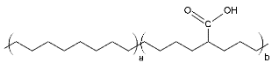	80.5	1.38	5	75
r9AA	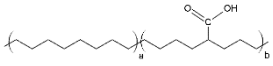	85.0	1.25	19	-

The preliminary results demonstrated feasibility of these rheology experiments on very small sample sizes (~20 mg) and enable the future study of precise acid polymers

and ionomers. A key limitation of previous measurements of the precise ionomers was the relatively few neutralization levels available for study. This was due to the combined difficulty of reaching high neutralization levels of the acid copolymer, as confirmed by elemental analysis post-neutralization, and the limited quantities of the unneutralized acid polymers to develop improved neutralization methods. The fabrication of a series of incrementally increasing ion-content samples combined with the ability to conduct rheological measurements on small samples sizes allows for a systematic study of how ionic aggregate morphology impacts the rheological properties.

Spectroscopy characterization of precise ionomers. In conjunction with rheological studies, spectroscopy techniques can be utilized to characterize local structure and dynamics. Dielectric relaxation spectroscopy (DRS), also known as broadband dielectric spectroscopy (BDS), is sensitive to the resonance of dipole moment reorientations with an applied oscillating electric field. Fourier-transform infrared spectroscopy (FTIR) is a non-destructive characterization technique that is also sensitive to the local environment of the polar pendant groups. The dielectric relaxation spectroscopy is expected to identify differences in the DC conductivity between Type 1 and Type 3 aggregates (isolated and percolated, respectively). Currently, DRS and FTIR measurements have been conducted on precise acid polymers and ionomers in collaboration with Prof. James Runt at the Pennsylvania State University. DRS measurements were conducted on precise acid-containing polymers that revealed an unacceptable level of residual protecting groups from an incomplete synthesis step. FTIR was able to confirm the presence of these residual ester groups, as seen in Figure 6.2 and discussed in further detail in Appendix C.

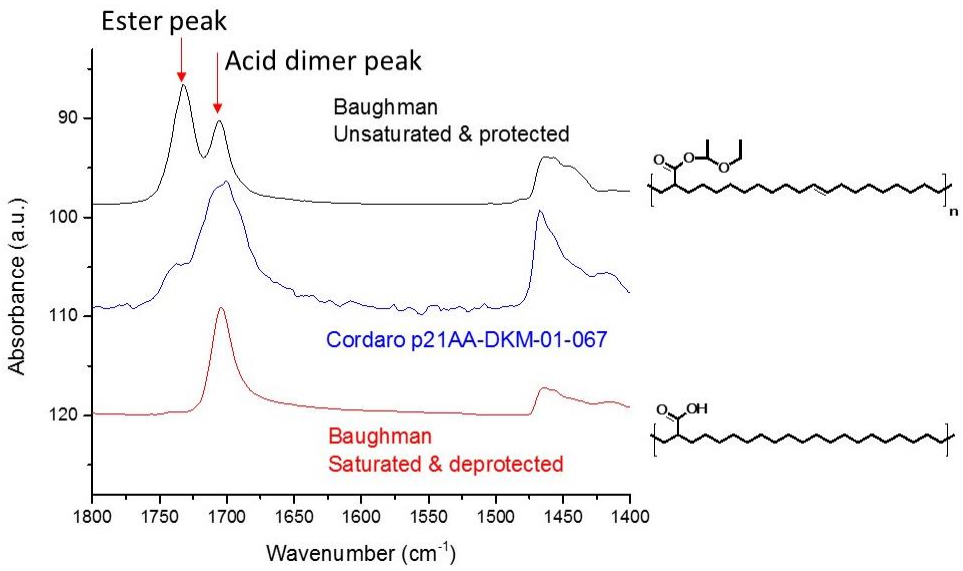

Figure 6.2. FITR measurements on p21AA-DKM-01-067 synthesized in large quantities by Dr. Joe Cordaro at Sandia National Laboratory. Comparisons are made with FTIR measurements conducted at the University of Florida before and after the saturation and deprotection step of the synthesis.

These FTIR data confirm that certain batches of precise acid-containing polymers and ionomers contain both protected and deprotected acid groups. The residual ester protecting groups exhibit a permanent dipole moment that significantly contributes to the DRS signal despite representing a small molar fraction (~2-5%). As such, DRS measurements should be repeated on an alternative batch of polymers with fewer residual esters present. It should be noted that these small fraction of ester group do not contribute as strongly to other forms of characterization, such as QENS which is dominated by the incoherent scattering of hydrogens.

Given the challenges of limited material quantities and some polymers containing residual protecting groups, an alternative synthetic route has been in development using a different protecting group by Drs. Dale Huber and Chet Simocko at Sandia National

Laboratories. Larger quantities have already been synthesized with rigorous confirmation that the deprotection step is complete and all residual benzyl groups were removed. Graduate student Lu Yan, of the Winey research group, is learning the polymerization, hydrogenation, and deprotection steps that will enable access to larger quantities of precise acrylic acid polymers.

The preliminary DRS and FTIR results demonstrate the value and feasibility of these techniques. Characterizing the local dynamics and structure of the acid and ionic groups will allow careful study of the differences in aggregate dynamics with the goal of understanding the impact of aggregate morphology on ion mobility. Potentially these data, through time-temperature superposition could be compared with computer simulations of ionomers in oscillatory electric fields which would be of interest to understanding dynamics in chemically heterogeneous systems with varied nanoscale morphologies, particularly Type 1 and Type 3 aggregates (isolated and percolated, respectively).[6]

Closing Remarks. The studies presented here investigated the impact of nanoscale aggregation on a variety of length and time scales with the goal of understanding bulk polymer properties. While this thesis has observed and correlated morphology to properties from local to bulk, these are largely phenomenological conclusions. Predicting a material property *a priori* remains a great challenge in the field of materials science and a thorough understanding of aggregation at the nanoscale remains a challenge. Improved material systems, experimental techniques, and computer aided simulations continue to expand our understanding of these important nanoscale features. Identifying and controlling the morphology, at all length scales, in polymer systems will advance the performance of these materials to the limitations of the very bonds that comprise the molecules.

References

1. Chen, Q.; Tudryn, G. J.; Colby, R. H. Ionomer dynamics and the sticky Rouse model. *Journal of Rheology* **2013,** 57, (5), 1441-1462.

2. Indei, T.; Takimoto, J. Linear viscoelastic properties of transient networks formed by associating polymers with multiple stickers. *J Chem Phys* **2010,** 133, (19), 194902.

3. Leibler, L.; Rubinstein, M.; Colby, R. H. Dynamics of reversible networks. *Macromolecules* **1991,** 24, (16), 4701-4707.

4. Chen, Q.; Huang, C.; Weiss, R. A.; Colby, R. H. Viscoelasticity of Reversible Gelation for Ionomers. *Macromolecules* **2015,** 48, (4), 1221-1230.

5. Huang, C.; Wang, C.; Chen, Q.; Colby, R. H.; Weiss, R. A. Reversible Gelation Model Predictions of the Linear Viscoelasticity of Oligomeric Sulfonated Polystyrene Ionomer Blends. *Macromolecules* **2016,** 49, (10), 3936-3947.

6. Ting, C. L.; Stevens, M. J.; Frischknecht, A. L. Structure and Dynamics of Coarse-Grained Ionomer Melts in an External Electric Field. *Macromolecules* **2015,** 48, (3), 809-818.

7. Lin, K.-J.; Maranas, J. K. Cation Coordination and Motion in a Poly(ethylene oxide)-Based Single Ion Conductor. *Macromolecules* **2012,** 45, (15), 6230-6240.

APPENDIX A

Dynamics of Precise Ethylene Ionomers Containing Ionic Liquid Functionality

A.1 Introduction

A molecular-level understanding of the dynamics of ionomers, polymers containing ionic functionality, is of considerable importance from both fundamental and applied points of view. The presence of ionic groups in, or pendant to, polymer chains is well known to significantly modify thermal, mechanical, and charge transport properties of the parent polymer due to various ionic interactions.[1, 2] As a result of the low dielectric constant of most organic polymers, ion dipoles tend to self-assemble into microphase-separated domains. Consequently, much of the fundamental research conducted on these materials has been devoted to determination of the structure of ion aggregates and the correlation between structure and the resulting properties.[3] Ionomers have been used commercially as separators, packaging materials and in molding applications,[4] and in recent years have been considered as candidate materials for energy storage devices (batteries and supercapacitors), in energy conversion (fuel cells) and for other electroactive materials applications.[5, 6]

Ionomers derived from copolymers of ethylene and methacrylic acid (MAA) have been well known since the 1960's, principally due to their versatile mechanical properties and chemical stability.[2-4, 7] Since these materials have relatively low MAA content and MAA units are randomly placed in the highly-branched polyethylene (PE) chains, long PE sequences exist and are capable of crystallization. The microstructure – property – processing relationships of these traditional ionomers have been the subject of many previous publications.[8-18]

The relatively recent discovery of a synthetic route for creating ethylene copolymers with precisely placed acid functionality along the chain has led to a remarkable new class of highly regular acid-functionalized (and cation-neutralized) ethylene copolymers.[19-24] Extensive morphological characterization of a growing number of precise acid copolymers and their ionomers has uncovered morphologies with considerably sharper X-ray scattering features (i.e., much less environmental heterogeneity) and unprecedented uniformity.[20, 25-28] Computer simulations have also been used to explore the ionic aggregation in PE-based precise ionomers and compact isolated aggregates, branched string-like aggregates, and percolated structures have been observed.[24, 29-32] However, despite recent advances in our understanding of the microphase-separated morphology of these unique copolymers and ionomers, there have been to date no reports on their molecular dynamics.

Herein, we focus on the investigation of polymer and ion dynamics of three precise (and one pseudorandom) PE-based ionomers, using dielectric relaxation spectroscopy (DRS). In a recent publication, acyclic diene metathesis (ADMET) polymerization in combination with post-polymerization functionalization was used to successfully produce linear high molecular weight PE with 1-methylimidazolium bromide (ImBr) units precisely substituted on every 9th, 15th, or 21st carbons along the chain, as shown in Figure A.1.[33] Dielectric spectroscopy is a particularly powerful tool for investigating the impact of associating ion pairs or aggregates on the motion of chain segments and substituent groups, over a broad range of frequencies and temperatures. In addition, the non-polar ethylene portions of the ionomers exhibit very low dielectric loss, allowing one to focus on the molecular motions of the ionic functionality. As there is an intimate connection between phase separated microstructure and molecular dynamics, the dynamics of the

precise ionomers cannot be well understood without microstructural insight. Consequently, our dielectric spectroscopy investigation is complemented by X-ray scattering and DSC measurements, as well as insight on local ionic interactions and ethylene spacer ordering from Fourier transform infrared spectroscopy.

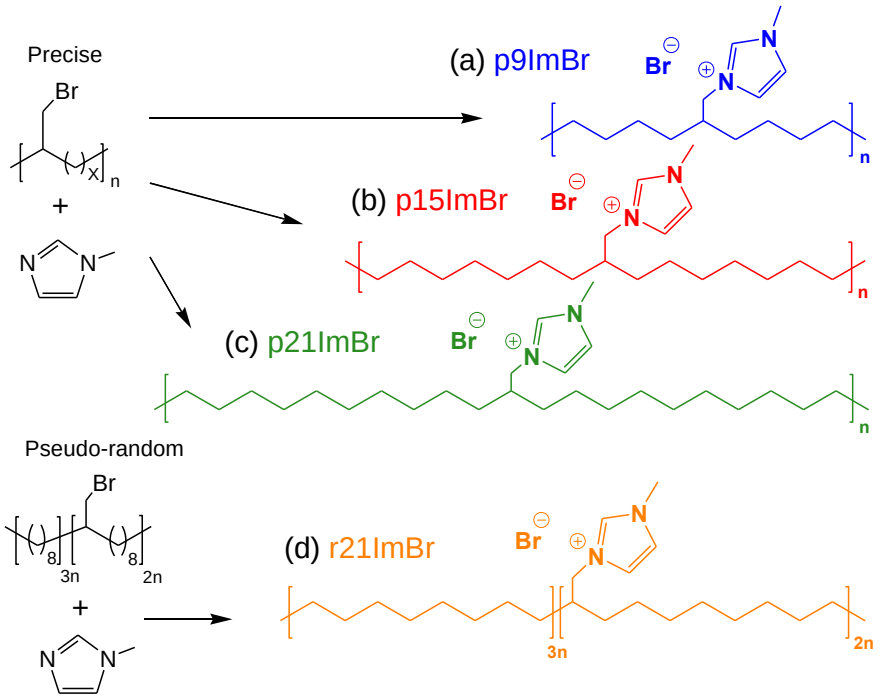

Figure A.1. The chemical structures of three polyethylene-based precise ionomers containing 1-methylimidazolium bromide groups on exactly every (a) 9th (p9ImBr), (b) 15th (p15ImBr), and (c) 21st (p21ImBr) carbon.[33] The findings on these precise ionomers are also compared with (d) a pseudorandom analogue (r21ImBr) that is compositionally identical to its precise counterpart (p21ImBr).[33]

A.2 Experimental

Figure A.**1**a-c show the molecular structures of the polyethylene (PE)-based ionomers containing 1-methylimidazolium bromide (ImBr) groups on exactly every 9th (referred to as p9ImBr), 15th (p15ImBr), and 21st (p21ImBr) carbon atom: the letter p indicates precise placement of ionic pendant groups along the polymer chain. These are linear high molecular weight materials with a polydispersity index of ~2.[33] The findings on these precise ionomers are also compared with those from one pseudorandom analogue (r21ImBr; its molecular structure is shown in Figure A.1d). The letter r indicates pseudorandom substitution and the number 21 denotes that, on average, there is one pendant per 21 carbon atoms, which makes this ionomer compositionally identical to its precise counterpart (p21ImBr).

Sample Preparation. For this study, the ionomer samples were prepared in the following manner. Films for FTIR, DSC, X-ray scattering, and dielectric measurements were melt-pressed at 150 °C for 20 min in a Carver 4122 hot press. Note that the thermal transitions (T_g, T_m) of all the ionomers are well below 150 °C (see Table 1A.1). The films were then subjected to rapid cooling (~15 °C/min) via a heat exchanger using tap water, and aged at room temperature in a vacuum dessicator for at least 3 days before data collection. Samples used in all experiments have the identical thermal history.

Fourier Transform Infrared Spectroscopy (FTIR). FTIR spectra were determined using a Nicolet 6700 FTIR spectrometer (Thermo Scientific) equipped with a diamond attenuated total reflectance (ATR) cell. The spectra were signal averaged from 200 scans with a resolution of 2 cm^{-1}.

Thermal Characterization. Differential scanning calorimetry (DSC) results were obtained on a TA Instruments Q2000 differential scanning calorimeter, with temperature and enthalpy calibrated using an indium standard. Samples weighed approximately 5 – 10 mg, and the thermograms were measured at a heating rate of 10 K/min under a helium purge. TA Instruments Universal Analysis 2000 Software was used to identify the phase transitions (T_g, T_m and ΔH_m).

X-ray Scattering. X-ray scattering was performed on a Multiangle X-ray Scattering (MAXS) system using a Nonius FR591 rotating-anode generator operated at 40 kV and 85 mA.[26, 27] A bright, highly collimated beam was obtained via Osmic Max-Flux optics and triple pinhole collimation under vacuum. Samples were loaded into 1.0 mm diameter glass capillaries (Charles Supper Co. Special Glass 10-SG), which were then flame-sealed. The scattering data were collected for 30 min using a Bruker Hi-Star multiwire two-dimensional detector at a sample-to-detector distance of 11 cm. The sample temperature was raised and maintained by a Linkam oven controlled via a Linkam TMS 94 temperature controller. The samples were heated to 120 °C and allowed to reach thermal equilibrium for 5 min prior to data collection. Two-dimensional data reduction and analysis of data were performed using the Datasqueeze software.[34]

Dielectric Relaxation Spectroscopy (DRS). Dielectric spectroscopy measurements were conducted on samples with thicknesses of 0.1 – 0.2 mm that were sandwiched between freshly polished brass electrodes with a top electrode diameter of 10 mm to form a parallel plate capacitor cell. The sample / electrode sandwiches were positioned in a Novocontrol GmbH Concept 40 broadband dielectric spectrometer. The dielectric permittivity was measured using a sinusoidal voltage with amplitude 0.1 V over

a 10^{-2} – 10^{7} Hz frequency range in all experiments. Data were collected in isothermal frequency sweeps every 5 K, from -50 to 150 ˚C.

A.3 Results and Discussion

ATR-FTIR. FTIR spectroscopy was used to augment earlier NMR characterization of the chemical structure of ImBr ionomers[33], as well as to provide insight on local ionic interactions and the nature of ethylene spacer ordering in the semi-crystalline ionomers. The important spectral regions of the four ionomers are displayed in Figure 1.2 with absorbance bands of particular interest highlighted. Above 2800 cm^{-1}, two intense absorbances are observed at ~2923 and 2850 cm^{-1}, which have been attributed to the alkyl C-H stretching modes of 1-methylimidazolium cations.[35, 36] The imidazolium cation can further be identified by spectral features in the 1600 – 700 cm^{-1} region. The bands at ~ 1570 and 1460 cm^{-1} are indicative of imidazole ring stretching, the peak at 1165 cm^{-1} has been assigned to imidazole H–C–C and H–C–N bending, and the broad band centered near 750 cm^{-1} is attributed to the out of plane C–H bending mode of the imidazole ring.[37-39]

The formation of hydrogen bonds between the aromatic protons and the Br anion is evidenced by the presence of a peak between 3050 and 3080 cm^{-1}. Upon formation of C-H•••Br hydrogen bonds, the C-H bond stretching located at ~3130 cm^{-1} is weakened and its vibration frequency decreases.[36] As expected, the peak at 3050-3080 cm^{-1}, related to the hydrogen bonds, and that at ~3130 cm^{-1}, attributed to the aromatic C-H not involved in hydrogen bonding, are relatively more intense for the ionomers containing a larger fraction of ImBr groups (p9ImBr). As the number of ImBr units decreases, the intensity of these peaks is also reduced (p15ImBr, p21ImBr and r21ImBr).

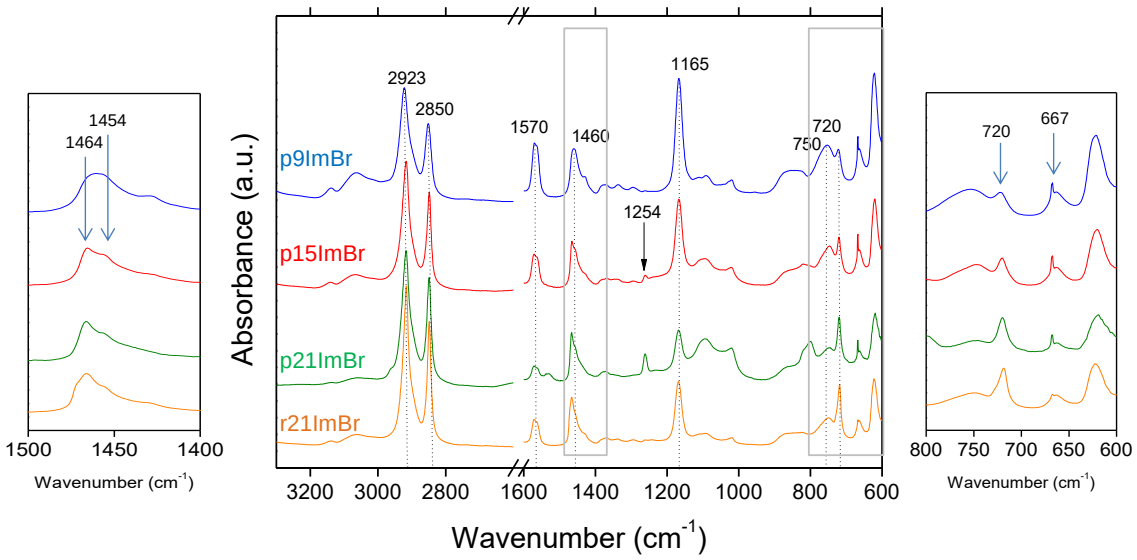

Figure 1.2. ATR-FTIR absorbance spectra of ImBr ionomers (p9ImBr, p15ImBr, p21ImBr and r21ImBr) in the region from 600 to 3300 cm^{-1} at room temperature. Data were shifted vertically for clarity. Scale expansion of the highlighted areas in the middle panel is provided in the left and right panels.

Another important spectral feature is the peak appearing at 720 cm^{-1}, corresponding to the CH_2 rocking vibrations, arising from both crystalline and amorphous segments of the PE spacers.[20, 40-42] The relative absorbance at 720 cm^{-1} with respect to the imidazolium ring mode at 750 cm^{-1} increases with the PE segment length between precisely-placed ImBr functionality. The CH_2 rocking vibration peak at 720 cm^{-1}, together with the band at 1462 cm^{-1} in the CH_2 bending region, can provide information on the crystalline unit cell. Based on previous results obtained by NMR and X-ray techniques on the same family of precise copolymers we would expect an orthorhombic crystalline phase.[27] Ethylene sequences in the typical orthorhombic PE unit cell display a doublet in the low frequency region that arises from long *trans* CH_2 sequences rocking at ~720 cm^{-1}

and sequences of 5 or more CH_2 rocking at 730 cm^{-1}.[43] The absence of splitting in the CH_2 rocking mode (see Figure 1.2- right panel), also not observed for other precise polyethylene-based copolymers,[20] may indicate some distortion of the orthorhombic unit cell in crystalline ImBr ionomers. In addition, Sworen, et al.[42] studied the evolution of the orthorhombic crystal of PE for random ethylene/propylene copolymers (characterized by a doublet at 719 and 730 cm^{-1} and single band at 1471 cm^{-1}) into a hexagonal unit cell, indicated by the appearance of methylene rocking (at 721 cm^{-1}) and scissoring (1466 cm^{-1}) modes. In the right panel of Figure 1.2 a single absorbance is observed at 720 cm^{-1}. At frequencies of ~1460 cm^{-1}, in addition to a contribution from the imidazolium rings, CH_2 scissoring is evidenced for the semi-crystalline samples, p15ImBr, p21ImBr and r21ImBr (Figure 1.2- left panel). In summary we conclude that for semi-crystalline ImBr ionomers, the presence of crystals having a hexagonal unit cell, together with the orthorhombic crystals, cannot be excluded.

Additional information on ordered ethylene sequences can be obtained from the region between 1350 and 1250 cm^{-1}. The absence of crystallinity in p9ImBr (see also DSC results in section 3B) is evidenced by the presence of bands in the region between 1330 and 1353 cm^{-1},[41] which are weaker in the semi-crystalline samples. These absorbances are related to the conformationally disordered ethylene sequences. A small peak is observed at 1254 cm^{-1} in p15ImBr and p21ImBr spectra, originating from conformationally ordered sequences, all-*trans*, composing the crystals. There is no detectable absorbance at 1254 cm^{-1} in the spectrum of the random ionomer r21ImBr, consistent with the proposal that precisely placed ionic groups favor order in the crystalline unit cells.[27]

FTIR spectroscopy also provides some insight on local conformations close to the ImBr pendant groups. The band at 622 cm^{-1} (Figure 1.2 - right panel) corresponds to the stretching of C−C side groups with vicinal C−C backbone carbons in an all-*trans* conformation, while the absorbance at 665 cm^{-1} corresponds to C−C stretching when the side group is adjacent to backbone carbons having *gauche* conformations.[35] The very narrow peak arising in the gauche conformation region for the precise ionomers may arise from rather ordered conformations at the ImBr aggregate interfaces, not evidenced in the spectrum of the random sample.

Thermal Analysis. Figure A.3 displays the DSC thermograms of the precise[27] and random ImBr copolymers. Table 1A.1 summarizes the glass transition temperatures (T_g), as well as melting temperatures (T_m) and enthalpies (ΔH_m) of the crystalline components in the ionomers. For p9ImBr the relatively large fraction of ionic pendants completely disrupts crystallization of the ethylene sequences, and this ionomer exhibits a single T_g with a midpoint of 15 ˚C. Clearly, aggregation of the ionic species (described in detail in section 3C) has a rather strong effect on the T_g of the matrix segments, whose motion is slowed significantly via their attachment to the ionic domains.

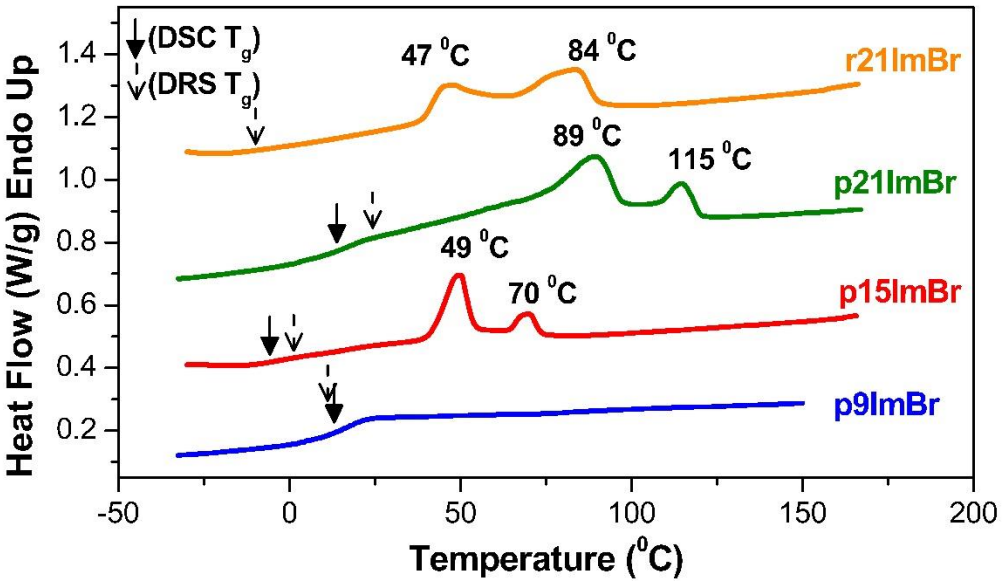

Figure A.3. DSC thermal analysis of the precise[27] and pseudorandom ionomers. The solid arrows indicate the DSC T_gs for p9ImBr, p15ImBr and p21ImBr. The dashed arrows represent the T_gs derived from dielectric spectroscopy by extrapolating the VFT fit of the segmental relaxation time to $\tau_\alpha(=1/\omega_\alpha)=100$ s (referred to as DRS T_g). For clarity, the thermograms have been shifted vertically.

The T_g s for the semi-crystalline ionomers are more difficult to detect by DSC, although their segmental relaxations (dynamic glass transition) are clearly evident in dielectric loss spectra (section 3D). For the semi-crystalline precise ionomers (p15ImBr, p21ImBr), we detect relatively broad T_g s from DSC, but T_g is absent in the DSC data from r21ImBr. The amorphous phase dynamics will be discussed in detail in section 3D.

Table 1A.1. Melting Points, Heats of Fusion, Degrees of Crystallinity, Glass Transition Temperatures, Total Ion Concentration and Refractive Indices of the Precise and Pseudorandom ImBr Ionomers.

	DSC				DRS		
	T_m (˚C)	ΔH_m [a] (J/g)	X_c [b] (%)	$T_g \pm 3$ (˚C)	$T_g \pm 10$ (˚C)	p_0 [c] (nm^{-3})	n [c]
p9ImBr	-	-	-	15	13	2.73	1.64
p15ImBr	49 & 70	15	6	-5	1	2.14	1.69
p21ImBr	89 & 115	26	9	13	25	1.75	1.72
r21ImBr	47 & 84	30	11	-	-9	1.75	1.72

a) ΔH_m is the total enthalpy of the melting endotherms.

b) $X_c = \Delta H_m / \Delta H_m^{PE}$ ($\Delta H_m^{PE} = 277$ J/g, the perfect crystal heat of fusion for orthorhombic PE).[44]

c) Total ion concentration p_0 and *n* were determined based on the molecular structure.

Note that although p15ImBr, p21ImBr, and r21ImBr display clear melting endotherms (Figure A.3), the degree of crystallinity under the crystallization conditions imposed here (Table 1A.1) is very small compared to linear PE (~70-80%), on the order of 10% or lower, and their T_ms (Table 1A.1) are well below that reported for linear PE synthesized by

ADMET polymerization (133 ˚C).[21] The presence of the polar ImBr side groups, even when precisely spaced, disrupts the ability of these materials to crystallize and slows crystallization considerably. As expected, ionomers with longer ethylene spacer lengths (decreasing ion content) lead to slightly higher degrees of crystallinity (X_c) and melting temperatures. Alamo, *et al.* have also observed an increase in T_m and X_c of PE with precision Cl placement as Cl content decreases.[21] In studies of other precise ethylene acid copolymers and ionomers, substitution of functional species (including acrylic acid and phosphonic acid with the mono or geminal substitution) on every 15th carbon atom has been found to completely suppress crystallization, in contrast to p15ImBr.[20, 25-27] ENREF 27 It has been proposed previously that the enhanced ordering of p15ImBr may arise from the relatively flexible CH_2 linkages between the ethylene backbone and ionic liquid pendant groups, as well as multiple hydrogen bonding sites in ionic liquids containing imidazolium bromide that facilitate ordering of the ionic species into sheet-like structures.[27, 36] In contrast, the acrylic acid and phosphonic acid groups are attached directly to the polymer backbone.

As noted earlier, the precise and pseudorandom ImBr ionomers were rapidly cooled from the melt to room temperature then aged for at least 3 days. As a consequence of the slow crystallization kinetics of these materials due to the limited mobility imposed by the strongly interacting ionic pendant groups,[22, 27, 33] only a portion of the crystallinity of these materials is developed on cooling from the melt (i.e., at comparatively low degrees of supercooling) and this fraction is assigned to the higher temperature melting endotherms. As their T_gs are below room temperature, limited crystallization continues on aging (larger degrees of supercooling), and this portion of the crystallinity is assigned to the lower temperature endotherms. Finally, the precise p21ImBr exhibits higher

temperature melting endotherms compared to the compositionally identical pseudorandom analog r21ImBr (although both have a similar degrees of crystallinity). This arises from enhanced ordering in p21ImBr due to the precise regularity of the substitution.

X-ray Scattering. Figure 1.4a compares the room temperature X-ray scattering profiles for the four ImBr ionomers with different PE segment lengths and ImBr placement (precise vs pseudorandom). The amorphous p9ImBr exhibits two broad scattering peaks: the higher angle peak at scattering wavevector $q \approx 15\text{nm}^{-1}$ corresponds to the amorphous halo and the low-angle peak at $q \approx 3.5\text{nm}^{-1}$ is associated with the mean interaggregate scattering arising from the segregation of ionic groups.[27] The semi-crystalline ionomers, p15ImBr, p21ImBr, and r21ImBr, exhibit a sharp X-ray scattering peak near $q \approx 15\text{nm}^{-1}$, corresponding to the (110) reflection for orthorhombic PE at $q \approx 15.3\ \text{nm}^{-1}$.[27] This confirms the semi-crystalline nature of the PE matrix observed in FTIR (Figure 1.2) and DSC (Figure A.3) measurements. p15ImBr and p21ImBr exhibit multiple scattering peaks (indicated by arrows in Figure 1.4a) at low angles that have positional ratios indicative of a layered morphology, indicating long-range order of the microphase-separated ion-containing layered aggregates.[27] The pseudorandom ionomer, r21ImBr, has a weak second peak that is consistent with a poorly-defined layered morphology. For the precise ionomers, the lowest-angle peak near $q \approx 3.5\text{nm}^{-1}$ shifts to lower q as the separation between ImBr functional groups in the chains increases, indicating as expected an increase in the average aggregate separation.[27]

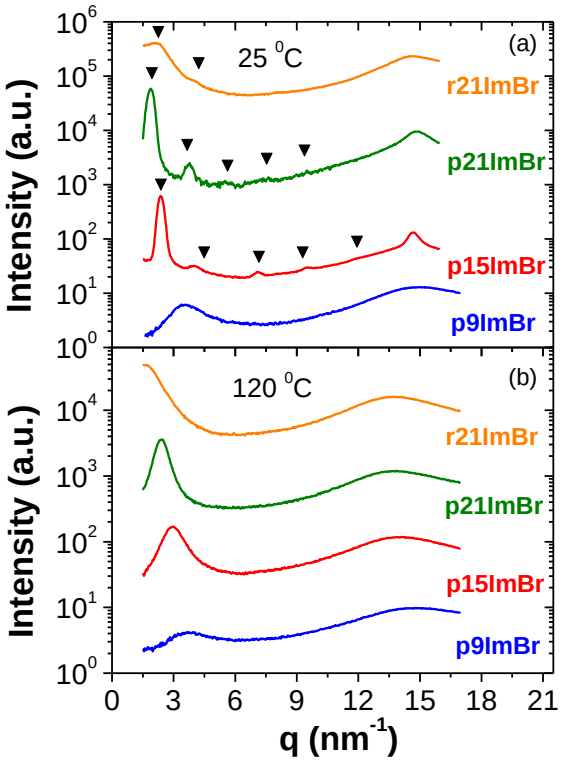

Figure 1.4. X-ray scattering intensity as a function of scattering wavevector q for the three precise and the pseudorandom ionomers at (a) 25 ˚C and (b) 120 ˚C.[26, 27]

From earlier X-ray scattering studies[26, 27] on precise ionomers, two morphologies have been identified based on the nature of the ionic aggregate resulting from microphase-separation of the ionic pendant groups and the PE matrix. When the PE segment is short (i.e., for p9ImBr) the material is amorphous and the ion pendants form aggregates that arrange with liquid-like order. When the PE segment length is longer (i.e., for p15ImBr and p21ImBr) and crystallizes, the precise ionomers exhibit layered morphologies at room temperature that contain ionic pendants arranged in sheets perpendicular to the PE spacers. At 120 ˚C (see Figure 1.4b), above the T_m of the semi-crystalline materials, all ionomers exhibit liquid-like morphologies and the scattering maximum at low angle

becomes broader and the higher order peaks are lost. Also at 120 ˚C the narrower, low-angle peak for p21ImBr broadens noticeably for the compositionally identical r21ImBr and is indicative of a more uniform distribution of interaggregate spacings in precise materials.[25]

Dielectric Relaxation. The segregated nature of ionic liquid pendant groups of the precise ImBr ionomers, as well as the crystallinity present for many of the materials, adds a degree of complexity to interpretation of the dielectric spectra. Although the ImBr ionomers do not exhibit high ionic conductivity per se (as shown later), conduction losses from ion motion are appreciable and can obscure loss peaks of interest, particularly at higher temperatures. Consequently, we use the derivative representation (ε_{der}),[45] which eliminates the conductivity contribution from dielectric loss spectra, to elucidate relaxation processes:[46-49]

$$\varepsilon_{der} = -\frac{\pi}{2}\frac{\partial \varepsilon'(\omega)}{\partial \ln \omega}. \quad (1)$$

where ω is the angular frequency. This method has been utilized to analyze dielectric loss spectra of other ion-containing polymers with notable success.[45-51] A representative example of the dielectric constant and loss along with ε_{der} are displayed as a function of frequency in Figure A.5 for p15ImBr at 80 ˚C. The real part of the conductivity (σ') is also displayed in this plot and illustrates the usual definition of the dc conductivity (σ_{DC}) from conductivity spectra.

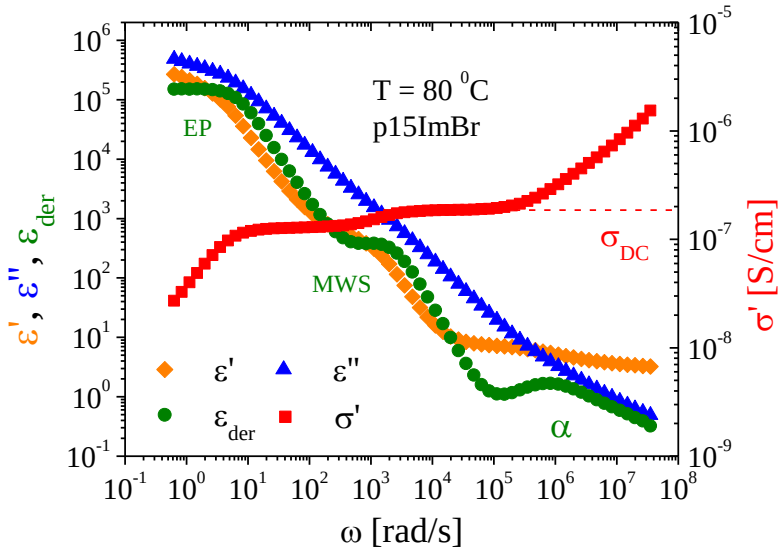

Figure A.5. Representative isothermal plot of the dielectric constant (ε'), the dielectric loss (ε''), the derivative spectra (ε_{der}) and the real part of the conductivity (σ') for p15ImBr at 80 ˚C. σ_{DC} is indicated by the dotted red line.

Figure 1.6 displays a representative example of the derivative dielectric loss spectrum as a function of frequency and temperature for p15ImBr. Spectra of all ImBr precise ionomers exhibit a single segmental α relaxation at lower temperatures and two slower but very strong processes at higher temperatures. The interpretation of the faster process as a segmental relaxation is supported by its VFT character, and the strength (~10^2 – 10^4) of the intermediate temperature – lower frequency process is much too large to be associated with dipole relaxation (even ion dipoles) and is clearly associated with Maxwell-Wagner-Sillars (MWS) interfacial polarization. Since electrode polarization (EP, the highest temperature process), a phenomenon where transporting ions accumulate at the blocking electrodes,[52] is not a characteristic relaxation of the materials, we focus our

discussion primarily on the segmental α relaxations and include some discussion of the MWS processes.

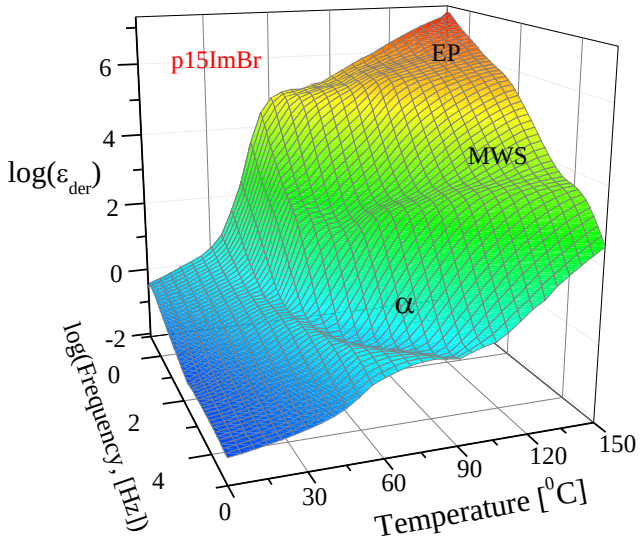

Figure 1.6. Representative conductivity-free dielectric derivative spectra ε_{der} as a function of frequency and temperature for p15ImBr.

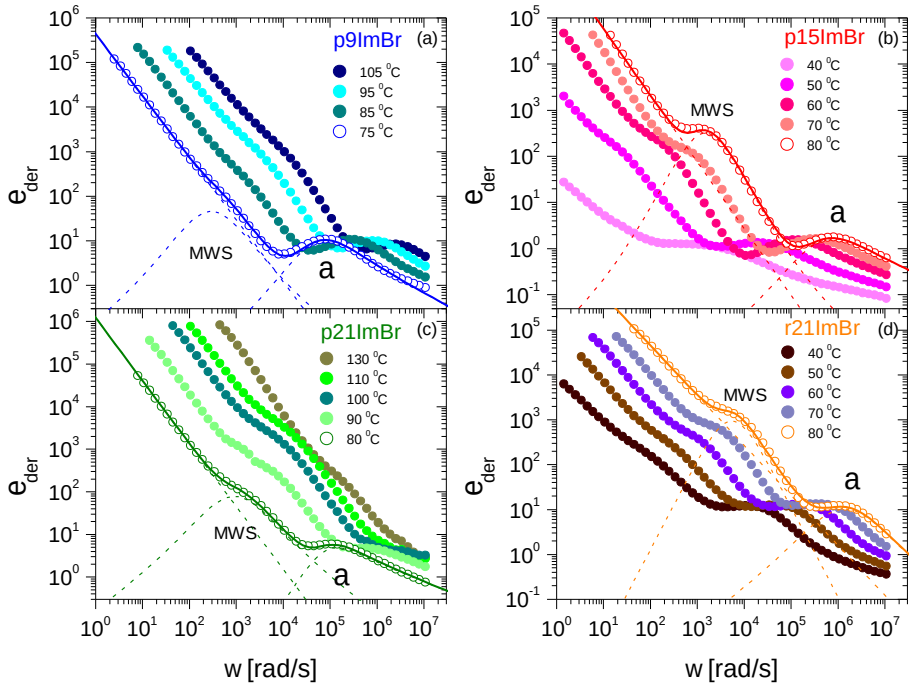

Figure A.7. Derivative spectra ε_{der} of (a) p9ImBr, (b) p15ImBr, (c) p21ImBr, and (d) r21ImBr at selected temperatures. Solid lines (overlaying open symbols for one temperature in each panel) are fits to Eq. 2 with values of the EP power law slope (s) and shape parameters (a and b) of the two HN functions for MWS interfacial polarization and polymer segmental motion (α) for (a) p9ImBr: $s=1.27\pm0.17$, $a_{MWS}=1$, $b_{MWS}=1$, $a_\alpha=0.83\pm0.10$, and $b_\alpha=0.77\pm0.17$ and for (b) p15ImBr: $s=1.36\pm0.12$, $a_{MWS}=1$, $b_{MWS}=1$, $a_\alpha=0.82\pm0.18$, and $b_\alpha=0.55\pm0.14$ and for (c) p21ImBr: $s=1.51\pm0.17$, $a_{MWS}=0.87\pm0.07$, $b_{MWS}=1$, $a_\alpha=0.90\pm0.08$, and $b_\alpha=0.51\pm0.10$ and for (d) r21ImBr: $s=1.15\pm0.15$, $a_{MWS}=0.81\pm0.11$, $b_{MWS}=1$, $a_\alpha=0.81\pm0.09$, and $b_\alpha=1$. For the same selected temperatures in each panel, individual contributions of the relaxations are shown as dashed lines.

The derivative spectra were then fit using a sum of a power law[53] for EP and two separate derivative forms of the Havriliak-Negami (HN) function for the MWS and α relaxation peaks (Figure A.7):

$$\varepsilon_{\mathrm{der}} = A\omega^{-s} - \frac{\pi}{2}\left(\left[\frac{\partial \varepsilon'_{\mathrm{HN}}(\omega)}{\partial \ln \omega}\right]_{\mathrm{MWS}} + \left[\frac{\partial \varepsilon'_{\mathrm{HN}}(\omega)}{\partial \ln \omega}\right]_{\alpha}\right) \text{ with } \varepsilon'_{\mathrm{HN}}(\omega) = \mathrm{Real}\left\{\frac{\Delta\varepsilon}{\left[1+(i\omega/\omega_{\mathrm{HN}})^{a}\right]^{b}}\right\}, \quad (2)$$

where A and s are constants, $\Delta\varepsilon$ is the relaxation strength, a and b are the shape parameters[54] and ω_{HN} is a characteristic frequency related to the frequency of maximum loss $\omega_{\max}$ by:

$$\omega_{\max} = \omega_{\mathrm{HN}}\left(\sin\frac{a\pi}{2+2b}\right)^{1/a}\left(\sin\frac{ab\pi}{2+2b}\right)^{-1/a}. \quad (3)$$

The peak relaxation frequency $\omega_{\max}$ and relaxation strength $\Delta\varepsilon$ of the MWS and α processes are determined from this fitting. On heating, the strength of the MWS process generally increases with temperature (along with σ_{DC}), and eventually merges with electrode polarization.

Segmental α process. The α process involves segmental motion of the polymer and hence exhibits typical characteristics of the glass transition dynamics. Representative behavior of the α relaxation as a function of temperature and frequency is displayed in Figure 1.8 for p9ImBr. It is important to point out that although the ionic liquid pendant groups are generally aggregated in this family of precise and pseudo-random ethylene

ionomers, some fraction of the ImBr species clearly participates in the α relaxation as determined from experimental relaxation strengths (Figure 1.9b). This indicates that not all of the ImBr species are fully immobilized in aggregates when using the processing conditions employed in the present study, and/or that aggregates are not symmetric and have a net dipole moment.

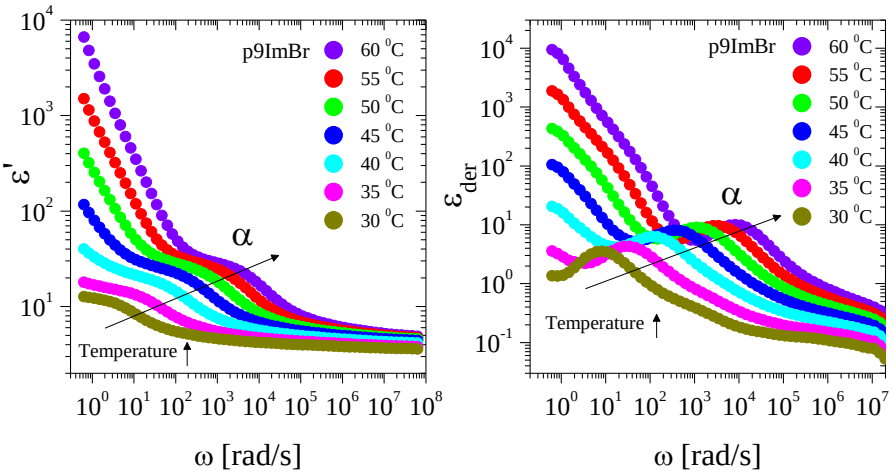

Figure 1.8. The dielectric constant (left) and derivative spectra (right) of p9ImBr as a function of temperature in the region of the dielectric spectrum where the α process is clearly observed.

The α peak relaxation frequencies are fit to the Vogel-Fulcher-Tammann (VFT) equation (see Figure **1.9**a),

$$\omega_{\max} = \omega_{\infty} \exp\left(-\frac{DT_0}{T - T_0}\right), \tag{4}$$

where ω_∞ is the high-temperature limiting frequency, D is the so-called strength parameter, and T_0 is the Vogel temperature, listed in Table 1A.2. The T_gs determined from DSC and those determined from the segmental relaxation by extrapolating the VFT fit of the peak relaxation time to $\tau_\alpha(=1/\omega_\alpha)=100$ s [55] are in relatively good agreement within experimental uncertainty (see Table 1A.1). Note that the T_gs from DRS are determined by extrapolation from the amorphous state. As noted earlier, although a DSC T_g could not be detected for r21ImBr, presumably arising from increased breadth and relatively small heat capacity change at T_g, the α relaxation is clearly visible in dielectric loss spectra.

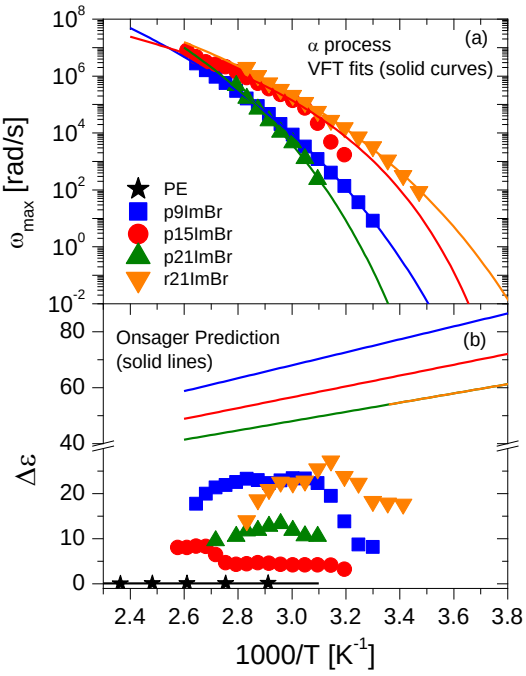

Figure 1.9. (a) Temperature dependence of relaxation frequency maxima ω_{max} of the α process: solid curves are fits of the VFT equation (Eq. 4).[56] (b) Temperature dependence of relaxation strength $\Delta\varepsilon$ of the α process: solid lines are predictions of the Onsager equation (with fixed concentration and strength of dipoles and assuming the Kirkwood correlation factor $g = 1$).

Table 1A.2. Fitting Parameters (Eq. 4) of the VFT Temperature Dependence and Fragility m of the α Process.

	$\log(\omega_\infty)$ (rad/s)	D	T_0 (˚C)	DRS T_g (˚C)	DRS T_g - T_0 (˚C)	(DRS T_g - T_0)/D	$m^a \pm 10$
p9ImBr	13.2	12.5	-63	13	76	6.0	57
p15ImBr	10.1	5.0	-41	1	42	8.4	79
p21ImBr	13.5	9.5	-38	25	63	6.6	73
r21ImBr	11.0	7.7	-63	-9	54	7.0	63

a) m determined from Eq. 5 using the VFT fit parameters for the segmental (α) peak frequency (Figure 1.9a).

As seen Table 1A.1, the T_gs determined for the precise ImBr ionomers vary over a modest temperature range when changing composition (and in the same fashion in DSC and DRS experiments). However, these (and correspondingly the ω_{max} in Figure 1.9a) vary in a non-systematic fashion, depending on composition, crystallinity and morphology. Using the relaxation of amorphous p9ImBr as a 'baseline', the α process becomes somewhat faster for p15ImBr, which contains longer ethylene spacer lengths between ImBr pendant groups. The α process then slows down for p21ImBr, becoming comparable to amorphous p9ImBr, presumably due to the influence of additional ethylene crystallization on the segmental dynamics. Even though p21ImBr and r21ImBr are

compositionally identical and exhibit similar crystallinities, the α relaxation for the polymer with random ImBr placement is considerably faster than that of p21ImBr. This is a clear manifestation of the important role of precise vs random pendant group placement on polymer dynamics, and likely arises from the occasional longer than average ethylene sequences in r21ImBr and perhaps also from the poorly-defined layered morphology of r21ImBr.

The parameter D in Eq. 4 is related to the fragility (i.e., deviation from Arrhenius behavior), providing additional information about the segmental relaxation time in the vicinity of T_g. The fragility m can be determined from:[57]

$$m = -\left.\frac{d\log(\omega)}{d(T_g/T)}\right|_{T=T_g} = \frac{DT_0}{T_g(\ln 10)(1-T_0/T_g)^2}, \quad (5)$$

wherein D and T_0 are VFT fitting parameters for ω_α (Figure 1.9a), using $T_g = \mathrm{DRS}\ T_g$. The estimated fragility m values of the semi-crystalline p15ImBr and p21ImBr ionomers (Table 1A.2) are essentially the same, while those for amorphous p9ImBr and crystalline r21ImBr appear at first glance to be slightly lower (m ~ 60). However, due to the limited number of data points available for this analysis (due to overlap of the segmental relaxation with MWS polarization) the uncertainty in the m values in Table 1A.2 is approximately ± 10, and consequently all are the same within experimental uncertainty. Prior observations have demonstrated the invariance of fragility with the presence and degree of crystallinity in other semi-crystalline polymers.[58-60]

Figure 1.9b displays the temperature dependence of the experimental relaxation strengths $\Delta\varepsilon$ of the α process for these ionomers and non-ionic polyethylene (PE). All

ionomers clearly have much higher $\Delta\varepsilon_\alpha$ than the non-ionic PE.[61] The increase in the strength arises from the enhanced dipole moment imparted by the ionic groups composed of imidazolium cations and Br^- anions. Given the disparity in chemical nature of the PE matrix and ionic liquid pendants as well as the sharp maxima observed in X-ray scattering, we adopt the view that all ImBr units reside in ionic aggregates. Consequently, this signifies that not all of the ImBr species are fully immobilized in aggregates and/or that aggregates are not symmetric and exhibit a net dipole moment.

As expected at higher temperatures, $\Delta\varepsilon_\alpha$ generally decreases with increasing temperature due to thermal dipole randomization. However, for the ionomers where $\Delta\varepsilon_\alpha$ can be reliably determined over a wider temperature range (p9ImBr and r21ImBr) the relaxation strength at lower temperatures is observed to increase significantly with temperature, indicating greater participation of ion dipoles in the segmental relaxation as temperature is increased.

We first consider the temperature dependence of $\Delta\varepsilon$ for these ionomers by utilizing the Onsager relationship,[47, 48, 62]

$$\frac{\Delta\varepsilon(2\Delta\varepsilon+3\varepsilon_\infty)}{(\Delta\varepsilon+\varepsilon_\infty)(\varepsilon_\infty+2)^2}=\frac{1}{9\varepsilon_0 kT}\sum_i \nu_i m_i^2, \tag{6}$$

where ν_i is the number density of dipoles, m_i is their dipole moment, k is the Boltzmann constant, T is absolute temperature, and ε_∞ is the high-frequency limit of the dielectric constant (here taken to as $\varepsilon_\infty = n^2$, where n is the refractive index, estimated from group contributions[63] and listed in Table 1A.1). The black solid line in Figure 1.99b is the fit to Eq. 6 with the $\sum_i \nu_i m_i^2$ term as the sole fitting parameter, showing that $\Delta\varepsilon$ of the non-

ionic PE is well described by the Onsager equation. For the ionomers with imidazolium cation - Br anion pendant groups, the contribution of the ions to the relaxation strength can be analyzed[47, 48, 64] by first considering the influence of contact ion pairs to Eq. 6:

$$\left[\frac{\Delta\varepsilon(2\Delta\varepsilon+3\varepsilon_\infty)}{(\Delta\varepsilon+\varepsilon_\infty)(\varepsilon_\infty+2)^2}\right]_{\text{ionomer}}=\frac{\nu_{\text{pair}}m_{\text{pair}}^2}{9\varepsilon_0 kT}+\left[\frac{\Delta\varepsilon(2\Delta\varepsilon+3\varepsilon_\infty)}{(\Delta\varepsilon+\varepsilon_\infty)(\varepsilon_\infty+2)^2}\right]_{\text{nonionic}}, \quad (7)$$

where ν_{pair} is the number density of ion pairs and m_{pair} is their dipole moment. For the dielectric constant range ($\varepsilon \sim 15 \pm 10$) of these ionomers, all ions are expected to remain paired because the coulombic interactions between anions and cations are strong (Bjerrum length [$1\text{ nm} < l_B \equiv e^2/(4\pi\varepsilon\varepsilon_0 kT) < 11\text{ nm}$], suggesting a pair energy > 60 ± 30 kT). The solid lines in Figure 1.9b are the Onsager predictions of Eq. 7 for each ionomer, for the hypothetical case where all ions are in the isolated ion pair state ($\nu_{\text{pair}} = p_0$, listed in Table 1A.1) with the contact pair dipole moment ($m_{\text{pair}} = 8.7$ D, determined from *ab initio* calculations[65]). Since ImBr groups are clearly seen in the X-ray scattering experiments to be aggregated and dynamic mechanical data reported in ref 33 displays a rubbery plateau consistent with aggregates reinforcing the polymer melt, it is expected and observed experimentally that the dielectric relaxation strengths for these ionomer are well below that of the corresponding Onsager prediction from Eq. 7. These ionomers are more polar than the non-ionic PE, but their ions are aggregated and largely immobilized at these temperatures, analogous to zinc-neutralized sulfonated polystyrene ionomers.[51] Nevertheless, the fact that the relaxation strength of the segmental process is much stronger than that of PE indicates that some fraction of ImBr pendants participates in the α process.

Since ionic species in aggregates are expected to lead to correlation of neighboring ion dipoles, one can estimate the fraction of the ImBr functional groups participating in the α relaxation of the precise ionomers by determining the Kirkwood – Fröhlich *g* factor (i.e., the dipole correlation factor): [66, 67,68]

$$g = \frac{9\varepsilon_0 kT}{\nu_{\text{pair}} m_{\text{pair}}^2}\left\{\left[\frac{\Delta\varepsilon(2\Delta\varepsilon + 3\varepsilon_\infty)}{(\Delta\varepsilon + \varepsilon_\infty)(\varepsilon_\infty + 2)^2}\right]_{\text{ionomer}} - \left[\frac{\Delta\varepsilon(2\Delta\varepsilon + 3\varepsilon_\infty)}{(\Delta\varepsilon + \varepsilon_\infty)(\varepsilon_\infty + 2)^2}\right]_{\text{nonionic}}\right\}, \qquad (8)$$

which is a measure of the effect of dipole interactions on the experimental relaxation strength. Dipole correlation factors were calculated from Eq. 8 for the case in which all ions are in the isolated ion pair state ($\nu_{\text{pair}} = p_0$ where p_0 is the total ion number density, listed in Table 1A.1) with the contact pair dipole moment ($m_{\text{pair}} = 8.7$ D). For p9ImBr, *g* ~ 0.2 – 0.4, indicating that (depending on temperature) about 20 – 40% of the ion dipoles in this ionomer contribute to the α relaxation, with ~60-80% either immobilized or having net anti-parallel arrangement in ion aggregates. The *g*-factors for p15ImBr and p21ImBr are similar, ranging from 0.1 – 0.2 for p15ImBr and 0.2 – 0.3 for p21ImBr. However, as can be inferred from Figure 1.9b, considerably more ImBr ion dipoles participate in the α process for the compositionally identical but pseudo-random r21ImBr (*g* ~ 0.4 – 0.6 depending on temperature), compared to p21ImBr. This is again a clear indication of the important role of precise vs random pendant group placement on the polymer dynamics. The origin of this difference is connected with the irregular ethylene sequence lengths and the poorly-defined layered morphology in r21ImBr, leading to relatively fewer ions fully immobilized in aggregates or that the relatively poorly organized aggregates in r21ImBr exhibit a comparatively larger net dipole moment than those in the precise ionomers. Finally, it is worth noting that in our recent study of precise ethylene – acrylic acid

copolymers with carboxylic acid functionality on every 9th, 15th or 21st carbon,[69] FTIR spectroscopy demonstrates that all of the acid groups exist in hydrogen-bonded dimers (and these assemble into acid aggregates). The dielectric relaxation strengths of the α processes for the precise acrylic acid – containing materials are comparatively very small, suggesting that the smaller acid functionality is more tightly bound in aggregates compared with the larger ImBr groups in the precise copolymers described herein.

Interfacial Polarization. Differences in dielectric permittivity and conductivity of the phases in heterogeneous materials give rise to interfacial polarization due to accumulation of charges near the interfaces between the various phases.[52] Such polarization typically occurs at frequencies lower than that of matrix segmental relaxation (and the onset of ion motion in the matrix phase) and with high relaxation strength. This interfacial polarization is referred to Maxwell-Wagner-Sillars polarization and has been studied previously for emulsions, multi-phase blends, block copolymers, and semi-crystalline polymers.[52, 70] Since all of the ImBr ionomers are clearly microphase-separated from the X-ray scattering measurements up to at least 120 ˚C (Figure 1.4), we expect the relaxation process observed at lower frequency in Figure A.7 to originate from charge build-up at the interfacial boundary between the microphase-separated aggregates (ion domains and lamellar interfaces) in a predominately non-polar PE matrix. As noted earlier, the observed relaxation strength of this process is on the order of $10^2 – 10^4$, which is far too large to be attributed to dipolar motions.

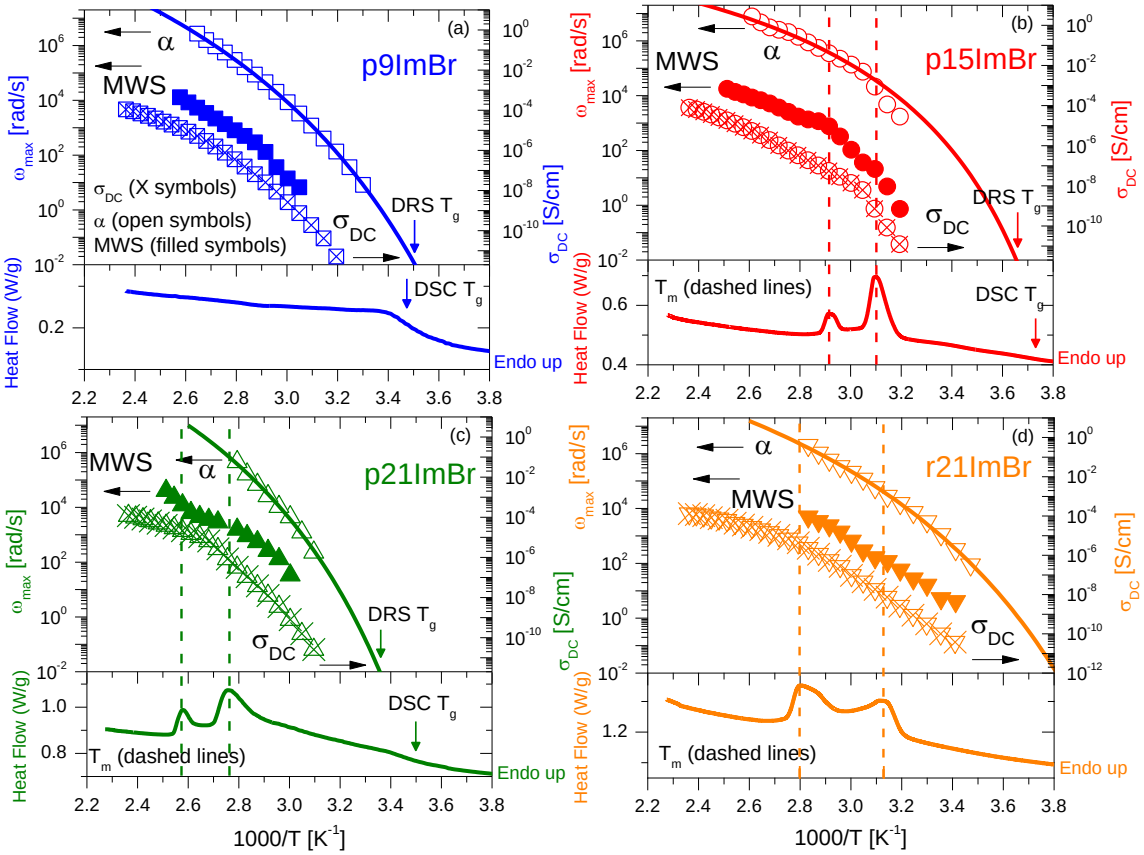

Figure 1.10. Temperature dependence of relaxation frequency ω_{max} for MWS process (filled symbols), α process (open symbols) and DC conductivity σ_{DC} (X symbols), along the DSC thermograms (solid lines) for (a) p9ImBr, (b) p15ImBr, (c) p21ImBr, and (d) r21ImBr. Vertical dashed lines indicate melting (T_m) transition temperatures from DSC and solid curves are VFT fits to the α relaxation frequencies.

The frequency and strength of the MWS process depend on the dielectric contrast (i.e., the difference in dielectric constant and conductivity) between the matrix and the microphase-separated ionic aggregates. Figure 1.10 shows that the relaxation frequencies for the interfacial MWS relaxation (ω_{MWS}, filled symbols) and DC conductivity (σ_{DC}, X symbols), along with the DSC thermograms (plotted as 1/T, solid lines) for all four

ionomers. Note that σ_{DC} is rather low (ca. 10^{-9} – 10^{-11} S/cm) for these materials at 40 ˚C, consistent with the segregated nature of the ionic species in the PE matrix and absence of significant ion domain connectivity. However, σ_{DC} increases rapidly as temperature increases well above T_g, generally following the expected VFT temperature dependence.

The peak relaxation frequencies of the MWS process follow a similar temperature dependence as their DC conductivity. Moreover, at the observed melting transitions (indicated by vertical dashed lines in Figure 1.10), the temperature dependence of ω_{MWS} and σ_{DC} exhibit a change in slope. This is additional evidence for the assignment of this process as originating from MWS polarization. Although not shown here, the relaxation strengths of the MWS process also depend strongly on temperature in the melting region. The MWS process does not disappear above T_m of the semi-crystalline ImBr ionomers, in agreement with findings from the higher temperature X-ray scattering experiments (Figure 1.4b) that ionic aggregates persist to high temperatures.

A.4 Summary

In this paper we report on the molecular dynamics of three polyethylene-based ImBr precise ionomers and one pseudorandom ionomer, in light of their microphase-separated morphologies. FTIR spectroscopy provides evidence of hydrogen bond formation between the aromatic protons and Br anions of ImBr pendants. X-ray scattering measurements demonstrate that semi-crystalline p15ImBr, p21ImBr and r21ImBr at room temperature exhibit layered morphologies, i.e., the ionic groups form planar aggregates that stack with long-range order, whereas amorphous p9ImBr exhibits ionic aggregates with liquid-like packing. All four of the ImBr precise ionomers exhibit liquid-like ordering of the microphase-separated ion aggregates at 120 ˚C.

DSC experiments confirmed the presence of crystallinity in the precise or pseudorandom ionomers with longer ethylene spacer length between pendant ImBr groups (p15ImBr, p21ImBr and r21ImBr). The degree of crystallinity is quite low however (on the order of 10%) as are the T_ms: the presence of the relatively large and polar ImBr, even when precisely spaced, severely disrupts the ability of the polyethylene sequences to crystallize under the preparation conditions used herein.

All of the ionomers display a single DSC T_g (when one can be determined) and correspondingly a single α process in dielectric relaxation experiments. T_gs range from approximately -9 to 20 ˚C depending on ImBr composition, ethylene segment crystallinity and microphase-separated morphology, and reflect the considerable slowing down of the motion of the matrix segments due to their attachment to ionic domains. r21ImBr, although compositional identical and having a similar crystallinity, exhibits significantly faster α relaxation dynamics compared to p21ImBr. This is in keeping with the important role of precise vs random pendant group placement on polymer segmental dynamics, and likely arises from the occasional longer than average ethylene sequences in r21ImBr.

As the X-ray scattering experiments clearly demonstrate that ImBr groups are aggregated, it is expected and observed experimentally that the segmental relaxation strengths for these ionomers are well below that of the corresponding Onsager prediction. However, $\Delta\varepsilon_\alpha$ was found to be much larger than that of PE alone and indicates that some fraction of ImBr pendants participates in the α process. Based on our proposal that all ImBr units reside in ionic aggregates, this suggests that not all of the ImBr species are fully immobilized in aggregates and/or that aggregates are not symmetric and exhibit a net dipole moment. Kirkwood dipole correlation factors were calculated for the precise ImBr ionomers to estimate the fraction of ImBr species participating in segmental relaxation.

For the precise ionomers, calculated *g*-factors range from ca. 0.1 – 0.4, depending on polymer composition and temperature. In other words, ~10 – 40% of the ion dipoles participate in the segment process for the precise ionomers, with the remainder immobilized or with net anti-parallel orientation in aggregates. However, considerably more ImBr ion dipoles participate in the α process for the compositionally identical but pseudo-random r21ImBr (g ~ 0.4 – 0.6 depending on temperature), compared to p21ImBr. This is again a clear indication of the important role of precise vs random pendant group placement on the polymer segmental dynamics.

A.5 References

1. Eisenber, A. *Adv. Polymer Sci.* **1967,** 55, 59-112.

2. Eisenber, A.; Kim, J. S., *Introduction to ionomers*. Wiley: New York, 1998.

3. Grady, B. P. *Polym Eng Sci* **2008,** 48, (6), 1029-1051.

4. Tant, M. R.; Mauritz, K. A.; Wilkes, G. L., *Ionomers: synthesis, structure, properties and applications*. Blackie Academic & Professional: London, 1997.

5. Armand, M.; Bruce, P. G.; Forscyth, M.; Scrosati, B.; Wieczorek, W., Polymer electrolytes. In *Energy materials*, Bruce, D. W.; O'Hare, D.; Walton, R. I., Eds. Wiley: New York, 2011.

6. Bouchet, R.; Maria, S.; Meziane, R.; Aboulaich, A.; Lienafa, L.; Bonnet, J.-P.; Phan, T. N. T.; Bertin, D.; Gigmes, D.; Devaux, D.; Denoyel, R.; Armand, M. *Nat Mater* **2013,** 12, (5), 452-457.

7. Schlick, S., *Ionomers: Characterization, Theory and Applications*. CRC Press: Boca Raton, 1996.

8. Eisenberg, A.; Hird, B.; Moore, R. B. *Macromolecules* **1990,** 23, (18), 4098-4107.

9. Laurer, J. H.; Winey, K. I. *Macromolecules* **1998,** 31, (25), 9106-9108.

10. Kutsumizu, S.; Tagawa, H.; Muroga, Y.; Yano, S. *Macromolecules* **2000,** 33, (10), 3818-3827.

11. Sauer, B. B.; McLean, R. S. *Macromolecules* **2000,** 33, (21), 7939-7949.

12. Taubert, A.; Winey, K. I. *Macromolecules* **2002,** 35, (19), 7419-7426.

13. Benetatos, N. M.; Winey, K. I. *J. Polym. Sci. Part B: Polym. Phys.* **2005,** 43, 3549-3554.

14. Loo, Y.-L.; Wakabayashi, K.; Huang, Y. E.; Register, R. A.; Hsiao, B. S. *Polymer* **2005,** 46, (14), 5118-5124.

15. Wakabayashi, K.; Register, R. A. *Polymer* **2005,** 46, (20), 8838-8845.

16. Wakabayashi, K.; Register, R. A. *Macromolecules* **2006,** 39, (3), 1079-1086.

17. Scogna, R. C.; Register, R. A. *J. Polym. Sci. Part B: Polym. Phys.* **2009,** 47, (16), 1588-1598.

18. Scogna, R. C.; Register, R. A. *Polymer* **2009,** 50, (2), 585-590.

19. Boz, E.; Wagener, K. B.; Ghosal, A.; Fu, R.; Alamo, R. G. *Macromolecules* **2006,** 39, 4437-4447.

20. Baughman, T. W.; Chan, C. D.; Winey, K. I.; Wagener, K. B. *Macromolecules* **2007,** 40, (18), 6564-6571.

21. Alamo, R. G.; Jeon, K.; Smith, R. L.; Boz, E.; Wagener, K. B.; Bockstaller, M. R. *Macromolecules* **2008,** 41, (19), 7141-7151.

22. Rojas, G.; Inci, B.; Wei, Y. Y.; Wagener, K. B. *J Am Chem Soc* **2009,** 131, (47), 17376-17386.

23. Opper, K. L.; Markova, D.; Klapper, M.; Mullen, K.; Wagener, K. B. *Macromolecules* **2010,** 43, 3690-3698.

24. Hall, L. M.; Seitz, M. E.; Winey, K. I.; Opper, K. L.; Wagener, K. B.; Stevens, M. J.; Frischknecht, A. L. *J Am Chem Soc* **2012,** 134, (1), 574-587.

25. Seitz, M. E.; Chan, C. D.; Opper, K. L.; Baughman, T. W.; Wagener, K. B.; Winey, K. I. *J Am Chem Soc* **2010,** 132, (23), 8165-8174.

26. Buitrago, C. F.; Alam, T. M.; Opper, K. L.; Aitken, B. S.; Wagener, K. B.; Winey, K. I. *Macromolecules* **2013,** 46, 8995-9002.

27. Buitrago, C. F.; Jenkins, J. E.; Opper, K. L.; Aitken, B. S.; Wagener, K. B.; Alam, T. M.; Winey, K. I. *Macromolecules* **2013,** 46, 9003-9012.

28. Buitrago, C. F.; Opper, K. L.; Wagener, K. B.; Winey, K. I. *Acs Macro Lett* **2012,** 1, 71-74.

29. Bolintineanu, D. S.; Stevens, M. J.; Frischknecht, A. L. *Acs Macro Lett* **2013,** 2, (3), 206-210.

30. Bolintineanu, D. S.; Stevens, M. J.; Frischknecht, A. L. *Macromolecules* **2013,** 46, (13), 5381-5392.

31. Hall, L. M.; Stevens, M. J.; Frischknecht, A. L. *Phys. Rev. Lett.* **2011,** 106, 127801.

32. Lueth, C. A.; Bolintineanu, D. S.; Stevens, M. J.; Frischknecht, A. L. *J. Chem. Phys.* **2014,** 140, 054902.

33. Aitken, B. S.; Buitrago, C. F.; Heffley, J. D.; Lee, M.; Gibson, H. W.; Winey, K. I.; Wagener, K. B. *Macromolecules* **2012,** 45, (2), 681-687.

34. Heiney, P. A. *Comm. Powder Diffr. Newsl.* **2005,** 32, 9-11.

35. Kaner, P.; Ruiz-Orta, C.; Boz, E.; Wagener, K. B.; Tasaki, M.; Tashiro, K.; Alamo, R. G. *Macromolecules* **2014,** 47, 236-245.

36. Elaiwi, A.; Hitchcock, P. B.; Seddon, K. R.; Srinivasan, N.; Tan, Y. M.; Welton, T.; Zora, J. A. *Dalton Trans.* **1995**, 3467-3472.

37. Berg, R. W.; Deetlefs, M.; Seddon, K. R.; Shim, I.; Thompson, J. M. *J Phys Chem B* **2005,** 109, (40), 19018-19025.

38. Holomb, R.; Martinelli, A.; Albinsson, I.; Lassègues, J. C.; Johansson, P.; Jacobsson, P. *J Raman Spectrosc* **2008,** 39, (7), 793-805.

39. Nath, A. K.; Kumar, A. *Ionics* **2013,** 19, 1393-1403.

40. HSU, T. S. *J Polym Sci Pol Phys* **1980,** 18, (12), 2379-2389.

41. Hagemann, H.; Strauss, H. L.; Snyder, R. G. *Macromolecules* **1987,** 20, (11), 2810-2819.

42. Sworen, J. C.; Smith, J. A.; Wagener, K. B.; Baugh, L. S.; Rucker, S. P. *J Am Chem Soc* **2003,** 125, (8), 2228-2240.

43. Snyder, R. G. *J Mol Spectrosc* **1961,** 7, (2), 116-144.

44. Brandrup, J.; Immergut, E. H., *Polymer Handbook*. John Wiley & Sons: New York, 1989.

45. Wübbenhorst, M.; van Turnhout, J. *J. Non-Cryst. Solids* **2002,** 305, (1-3), 40-49.

46. Fragiadakis, D.; Dou, S.; Colby, R. H.; Runt, J. *Macromolecules* **2008,** 41, (15), 5723-5728.

47. Fragiadakis, D.; Dou, S.; Colby, R. H.; Runt, J. *J. Chem. Phys.* **2009,** 130, (6), 064907.

48. Choi, U. H.; Lee, M.; Wang, S.; Liu, W.; Winey, K. I.; Gibson, H. W.; Colby, R. H. *Macromolecules* **2012,** 45, 3974-3985.

49. Choi, U. H.; Mittal, A.; Price, T. L.; Gibson, H. W.; Runt, J.; Colby, R. H. *Macromolecules* **2013,** 46, 1175-1186.

50. Castagna, A. M.; Wang, W.; Winey, K. I.; Runt, J. *Macromolecules* **2010,** 43, (24), 10498-10504.

51. Castagna, A. M.; Wang, W.; Winey, K. I.; Runt, J. *Macromolecules* **2011,** 44, (8), 2791-2798.

52. Kremer, F.; Schönhals, A., *Broadband Dielectric Spectroscopy*. Springer-Verlag: New York, 2002.

53. The EP process was fit with a simple power law because the slope on the high-frequency side of EP is nearly identical to that of a simpler power law. This reduces the number of overall fitting parameters and achieves more stable fits. This method has been utilized previously to analyze relaxation processes of ionomers with rather good success.[46, 48, 49].

54. In order to reduce the number of overall fitting parameters and to achieve more stable fits, we set the HN shape parameters (a and b) for the MWS process to the Cole-Cole type (0 < a < 1 and b = 1) in the fit of derivative spectra.

55. Angell, C. A. *Chem Rev* **1990,** 90, (3), 523-542.

56. The three data points at lower temperatures for p15ImBr are not included in the VFT fit. The semi-crystalline p15ImBr shows a transition in Wmax at Tm: above Tm the temperature dependence is well described by a single VFT expression, but below Tm it deviates. As a result, the Tg from extrapolation to 100 s is from the amorphous state.

57. Angell, C. A. *Science* **1995,** 267, (5206), 1924-1935.

58. Mijović, J.; Sy, J.-W. *Macromolecules* **2002,** 35, (16), 6370-6376.

59. Kanchanasopa, M.; Runt, J. *Macromolecules* **2004,** 37, (3), 863-871.

60. Ngai, K. L.; Roland, C. M. *Macromolecules* **1993,** 26, (11), 2688-2690.

61. Sayre, J. A.; Swanson, S. R.; Boyd, R. H. *J Polym Sci Pol Phys* **1978,** 16, (10), 1739-1759.

62. Onsager, L. *J Am Chem Soc* **1936,** 58, (8), 1486-1493.

63. van Krevelen, D. W., *Properties of Polymers*. Elsevier: New York, 1990.

64. Wang, W.; Tudryn, G. J.; Colby, R. H.; Winey, K. I. *J Am Chem Soc* **2011,** 133, (28), 10826-31.

65. Liu, W.; Janik, M. J.; Colby, R. H., First Principles Design of Ionomers for Facile Ion Transport. In *Polymers for Energy Storage and Delivery: Polyelectrolytes for Batteries and Fuel Cells*, Page, K. A.; Soles, C. L.; Runt, J., Eds. American Chemical Society: Washington, 2011; pp 19-44.

66. Kirkwood, J. G. *J. Chem. Phys.* **1939,** 7, (10), 911-919.

67. Oster, G.; Kirkwood, J. G. *J. Chem. Phys.* **1943,** 11, (4), 175-178.

68. Fröhlich, H., *Theory of Dielectrics : Dielectric Constant and Dielectric Loss*. Oxford : Clarendon Press: London, 1949.

69. Soccio, M.; Choi, U. H.; Middleton, L. R.; Buitrago, C. F.; Masser, H. Q.; Cordaro, J.; Winey, K. I.; Runt, J. *Manuscript in preparation*.

70. Priou, A., *Dielectric Properties of Heterogeneous Materials*. Elsevier: New York, 1992.

APPENDIX B

High Frequency Dielectric Relaxation Spectroscopy Experiments

B.1 Motivation.

Conventional batteries use electrolytes in a liquid phase typically consisting of acids or solvents which are highly volatile and extremely flammable. An alternative, more stable, electrolyte under current research are polymer electrolytes. The tradeoff of the improved safety in using these alternative electrolyte material systems is most often decreased ion conduction. A component of my thesis research has been studying the effects of nano-scale ionic aggregate morphologies on the atomic scale dynamics in ion-containing polymer systems, Chapter 5. The purpose of these studies is to identify if the polymer dynamics and the ion dynamics can be decoupled, resulting in design rules for polymers with improved ion conduction for energy storage applications.

During the summer of 2015, with the help and guidance of Dr. Ryusuke Nozaki and his research group at the University of Hokkaido, Japan, I set out to extend the capabilities of one of their specialized instruments to operate at elevated temperatures. Successful operation of this dielectric relaxation spectrometer (DRS) instrument, the Agilent 8510C Network Analyzer, would allow the study of the dynamics of charged species on the time scales of nanoseconds down to picoseconds. Furthermore, high

frequency DRS is more sensitive to dipole motions and would complement the polymer dynamics measured by QENS experiments, Chapter 5.

B.2 Results

After equipping and assembling the sample fixture and sample holding stage with new components capable of withstanding high-temperatures, systematic studies were performed to qualify the instrument. With any DRS setup there are background electromagnetic signals from the setup (cables, junctions, etc.) which are usually accounted for through calibrating with a standard. It became clear, however, there was background electromagnetic signals in this new setup that were strongly temperature dependent. This unexpected experimental difficulty necessitated careful study to remove this background and to extract accurate signal from the samples.

More careful examination into the source of this background signal suggested two components of the signal. First can be characterized by a strong increase, sometimes as high as 40 a.u., in the dielectric storage followed by the signal plummeting into the negative dielectric storage value, as seen in Figure 2.1. This behavior is consistent with a resonance somewhere within the assembly. As Figure 2.1 demonstrates three equivalent measurements of air at 70°C on separate occasions are substantially different in collected signal. Moreover, the upturn in the dielectric storage coincides with a peak in the dielectric loss, Figure B.**2**, which also suggests a resonance phenomenon. This resonance peak shifted with temperature, sample to sample, and even when repeating measurements on the same material on different days. This inconsistent background signal due to a resonance prohibits reliable background subtraction even if the system was calibrated prior to each experiment.

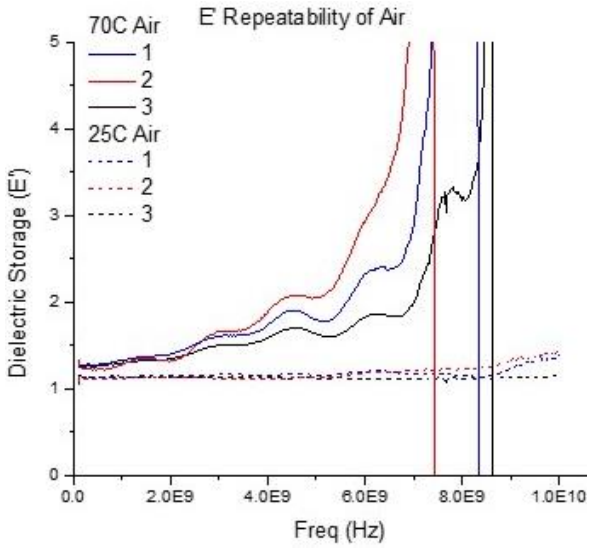

Figure 2.1. Measurement of the dielectric storage of air with three representative replicate measurements. Air was measured on separate days in an identical fashion and at a range of temperatures. The inconsistency in E' sudden drop off, vertical line left, between experiments suggests a variable background that makes background removal unreliable.

The second source of background appeared as a highly repetitive, but significant, wave function in the dielectric constant, known to the community as multiple reflections of the ENM wave within the fixture. While this signal alone can be modeled and removed, the superposition of these multiple reflections with the strong and irregular resonance signal make fitting and removing the background intractable.

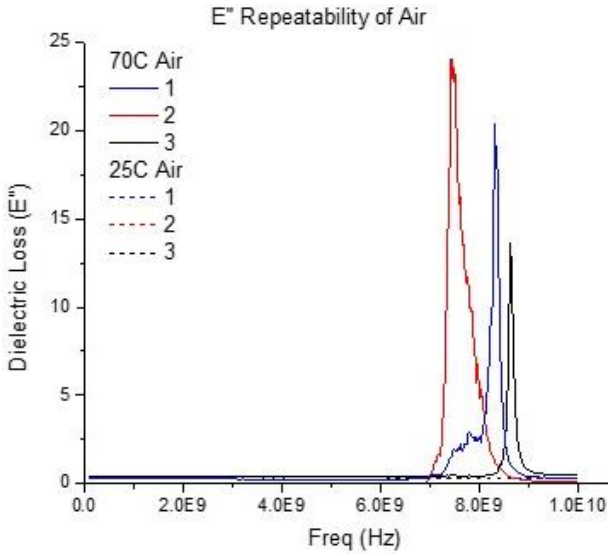

Figure B.2. Measurement of the dielectric loss of air with three representative replicate measurements. Air was measured on separate days in an identical fashion and at a range of temperatures. The inconsistency in E'' peak, right, between experiments suggests a variable background that makes background removal unreliable.

The combination of these two signals leads to significant and inconsistent background noise relative to the weak measured dielectric response. Moreover, the small number acid groups, whose dynamics are of most interested, are difficult to detect. The relatively low signal to noise ratio that our samples are capable of producing, combined with the erratic and strong background signal, has prevented me from conclusively identifying the sample relaxations of interests.

Dr. Nozaki's expertise and support was essential in my progress in both experimental work and in my professional and cultural development. He and his lab were encouraging, knowledgeable, and accommodating to our experimental plan. Our good faith effort to overcome the unexpected experimental difficulties lead to our conclusion that the significant and irregular background noise made reliable testing impossible in the

short 10 week timeline. Significant characterization of the setup are necessary to diagnose and eliminate the background noise at higher frequencies and high temperatures.

APPENDIX C

Fourier-transform infrared spectroscopy characterization of residual protecting groups in precise acrylic acid polymers

In Fourier-transform infrared spectroscopy (FTIR) is a non-destructive characterization technique that is sensitive to the local environment of the polar pendant groups. FTIR was able to confirm the presence of these residual ester groups, as seen in Figure 6.2.

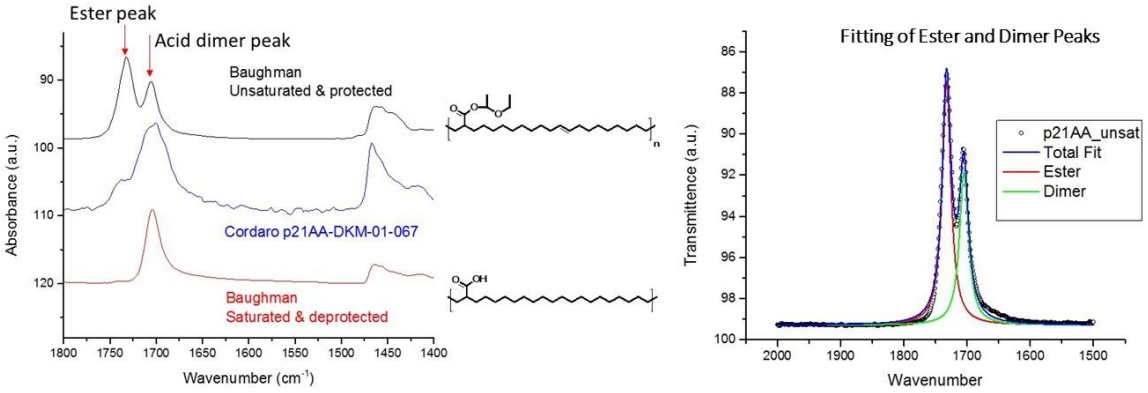

Figure 3C.1. Left, FITR measurements on p21AA-DKM-01-067 synthesized by Joe Cordaro at Sandia National Laboratory. Comparisons are made with FTIR measurements conducted at the University of Florida before and after the saturation and deprotection step of the synthesis. Right, an example of the fitting procedure of FTIR data to compare the area of the ester and dimer peaks.

An approximate quantification of the degree of residual protection groups were made through fitting of the FTIR data. An example of the fitting procedure is shown in Figure 6.2.Using the unstaturated form of the polymer from Baughman's original

synthesis, the ratio of the ester peak to dimer peak was used as a baseline. Using these as normalization factor, estimated residual protecting groups were made and reported in Table C3.1.

Table C3.1. Estimated residual protecting groups on precise polymers synthesized by Joseph Cordaro, as calculated through fitting of FTIR data.

Material	Ratio Dimer/Ester Peak Area	Normalized Ratio Dimer/Ester:
p21AA-Baughman Unsaturated/Protected	140%	
p21AA-Baughman Saturated/Deprotected	~0%	
p21AA-DKM 041	7.1%	5.10%
p21AA-DKM 067	8.0%	5.72%
p21AA-DKM 068	6.9%	4.92%
p15AA-DKM 065	4.2%	2.97%
p9AA-DKM 071	6.5%	4.61%
p9AA-DKM 066	7.8%	5.61%

These data confirm that FTIR characterization on these batches of precise acid-containing polymers and ionomers contain an incomplete synthesis step. It should be noted that these small fraction of ester group do not contribute as strongly to other forms

of characterization, such as QENS which is dominated by the incoherent scattering of hydrogens.

APPENDIX D

Supplemental Information for Chapter 2

D.1 Synthesis of Well-Defined Poly(ethylene-co-acrylic acid) Copolymers

The synthesis of 1-ethoxyethyl-2-(pent-4-enyl)hept-6-enoate (**1**), 1-ethoxyethyl-2-(oct-7-enyl)dec-9-enoate (**2**), and 1-ethoxyethyl-2-(undec-10-enyl)tridec-12-enoate (**3**) and corresponding polymeric materials were synthesized via modification of the literature procedures.[1, 2]

Representative Monomer Synthesis: ***2,2-di(pent-4-en-1-yl)malonic acid***. In an argon-filled glove box solid NaH (7.05 g, 294 mmol) was added to a 500 mL round-bottom flask equipped with a stir bar. Anhydrous THF cooled to -35 °C (150 mL) was added to form a suspension. Diethyl malonate (13.43 g, 84 mmol) was added drop-wise over the course of 10 minutes while stirring. 5-Bromo-1-pentene (25 g, 167.9 mmol) was then added drop-wise, allowed to warm to room temperature and stirred overnight. After this time, additional 5-bromo-1-pentene (5.00 g, 34 mmol) was added and the reaction mixture was vigorously refluxed for 24 hours. The mixture was then removed from the glove box, cooled in an ice bath, and water was added slowly to neutralize the remaining NaH. An additional 50 mL of water (total ~ 100 mL) and ethanol (50 mL) were added along with NaOH (16.8 g, 420 mmol) and the reaction was vigorously refluxed for 24 hours under argon. After cooling to room temperature the solution was acidified to pH ~ 2-3 with concentrated HCl and vigorously stirred for 2 - 3 hours at room temperature. The mixture was extracted with diethyl ether (10x100 mL) and chloroform (3x50 mL). The organic portions were combined and filtered through a thick pad of diatomaceous earth. The volatiles materials were removed *in vacuo* to afford an off-white residue. Addition of

pentane resulted in rapid crystallization of a white solid, which was collected on a frit and washed with additional pentane to afford 2,2-di(pent-4-en-1-yl)malonic acid in 69.4 % (14.0 g, 58.3 mmol) yield. Note: The literature procedure details a 1-pot synthetic procedure for generation of the mono-acid. It was found that purification of intermediates was required to obtain the final product in appreciable yields. ***2,2-di(oct-7-en-1-yl)malonic acid:*** Starting with NaH (4.88 g, 203 mmol), diethyl malonate (9.31 g, 58.1 mmol), 8-bromo-1-octene (25 g, 131 mmol) and NaOH (5.78 g, 145 mmol) and using the above procedure the product was isolated in 58.6 % yield (11 g, 33.9 mmol). ***2,2-di(undec-10-en-1-yl)malonic acid:*** Starting with NaH (2.24 g, 93 mmol), diethyl malonate (4.27 g, 26.7 mmol), 11-bromoundec-1-ene (14 g, 60 mmol) and NaOH (4.73 g, 118 mmol) and using the above procedure the product was isolated in 66.3 % yield (7.04 g, 17.7 mmol).

2-(pent-4-en-1-yl)hept-6-enoic acid. 2,2-di(pent-4-en-1-yl)malonic acid (14.0 g, 58.3 mmol), decalin (50 mL), and *N,N*-(dimethylamino)pyridine (DMAP) (0.35 g, 2.9 mmol)were added to a 500 mL round-bottom flask equipped with a stir bar and a reflux condenser. The flask was lowered into a 190 °C oil bath. The immediate release of CO_2 was evident. After the frothing had ceased the reaction was stirred for an additional 30-45 minutes at this temperature. Decalin was then removed via distillation. Purification of the residue by flash chromatography using a hexanes:ethyl acetate gradient as the eluent gave 7.3 g of a colorless oil (37.2 mmol, 64 %). Characterization was consistent with what was reported in the literature. ***2-(oct-7-enyl)dec-9-enoic acid:*** Starting with 2,2-di(oct-7-en-1-yl)malonic acid (11.0 g, 33.9 mmol), decalin (50 mL), and *N,N*-(dimethylamino)pyridine (DMAP) (0.40 g, 3.27 mmol) and using the above procedure the product was isolated in 81.1 % yield (7.71 g, 27.5 mmol). Characterization was consistent with what was reported in the literature. ***2-(undec-10-enyl)tridec-12-enoic acid.*** Starting with 2,2-di(undec-10-en-1-yl)malonic acid (11.0 g, 27.9 mmol), decalin (50 mL), and *N,N*-

(dimethylamino)pyridine (DMAP) (0.34 g, 2.79 mmol) and using the above procedure the product was isolated in 71.6 % yield (7.07 g, 20.0 mmol). Characterization was consistent with what was reported in the literature.[1]

General Procedure for Acid Protection. ***1-ethoxyethyl-2-(pent-4-enyl)hept-6-enoate* (1).** Under a flow of argon a solution of 2-(pent-4-en-1-yl)hept-6-enoic acid (7.3 g, 37.2 mmol) in diethyl ether (20 mL) was slowly added to a cooled (0 °C), degassed solution of ethyl vinyl ether (13.4 g, 186 mmol) and phosphoric acid (5-10 drops from capillary pipet) in diethyl ether (20 mL). The solution was stirred at 0 °C and slowly warmed to room temperature overnight and allowed to stir for 3 days. After this time, basic alumina (~5 g) was added and the reaction mixture stirred for 4 hours at room temperature. The mixture was filtered through a pad of alumina, which was rinsed copiously with diethyl ether. Removal of the solvent and distillation afforded the pure product as a colorless oil (5.4 g, 20.1 mmol, 54.1%) Characterization was consistent with what was reported in the literature.[1] ***1-ethoxyethyl-2-(oct-7-en-1-yl)dec-9-enoate* (2).** Starting with 2-(oct-7-enyl)dec-9-enoic acid (7.9 g, 28.2 mmol), ethyl vinyl ether (10.28 g, 143 mmol) and phosphoric acid (5-10 drops from capillary pipet) the product was isolated in 83 % yield (8.3 g, 23.5 mmol). Characterization was consistent with what was reported in the literature.[1] ***1-ethoxyethyl-2-(undece-10-en-1-yl)tridec-12-enoate* (3).** Starting with 2-(undec-10-enyl)tridec-12-enoic acid (5.9 g, 16.8 mmol), ethyl vinyl ether (4.87 g, 67.6 mmol) and phosphoric acid (~5 drops from capillary pipet) and using the above procedure afforded a crude material. Activated charcoal was added to the crude material and the mixture stirred for one hour at room temperature. After this time, the material was filtered through a silica plug, eluted with CH_2Cl_2 and recrystallized from pentane to afford the monomer as a white solid (5.03 g, 11.52 mmol, 68.2 %). Characterization was consistent with what was reported in the literature.[1]

General Optimized Procedure for ADMET Polymerizations. Neat protected monomer (3 – 5 grams) was added to a 100 mL Schlenk flask equipped with a magnetic stir bar and degassed by stirring under high vacuum for 4 h at room temperature. Grubbs first-generation catalyst (100:1 monomer:catalyst) was dissolved in CH_2Cl_2 and added to the flask under argon. In the case of 1-ethoxyethyl-2-(undece-10-en-1-yl)tridec-12-enoate the solid material was dissolved in xylenes (10 mL) and the procedure carried out analogously**.** High vacuum was slowly applied and the mixture stirred at room temperature for 4 hours. Afterwards, the temperature was slowly raised to 35 °C and the mixture stirred overnight. After this time, the solid mixture was heated to 50 °C at which point stirring resumed. Grubbs first-generation catalyst (100:1 monomer:catalyst) was dissolved in xylenes (10 mL) and added to the viscous reaction mixture. Vacuum was applied slowly and the reaction allowed to stir overnight. After this time the reaction was heated to 55 °C and Grubbs first-generation catalyst (200:1 monomer:catalyst), dissolved in xylenes (10 mL), was added to the flask and stirred under vacuum until stirring ceased. Upon cooling the room temperature, ethyl vinyl ether (~50 drops) in toluene (50 mL) was added to the flask and the mixture stirred until all solids dissolved. Precipitation of the crude solution into water (500 mL, 0.5 M HCl) afforded a brown tacky solid. The solid material was dissolved in THF and filtered through a thick pad of diatomaceous earth. The solvent was reduced and the polymer precipitated into water, collected, dried overnight in a vacuum oven and used in the next step without further purification.

Optimized Conditions for Hydrogenation. A solution of unsaturated polymer **(**typically 3 - 5 grams**)** was dissolved in a mixture of toluene (150 mL) and 1-butanol (75 mL). Argon was bubbled through the mixture for approximately 30 minutes. Wilkinson's catalyst [$RhCl(PPh_3)_3$] (0.5 mol %) was added to the solution, and the reactor was pressurized to 400 psi with hydrogen gas and purged three times while stirring. The reactor

was then filled to 750 psi with hydrogen, and heated to 100 °C for 48 h. Upon cooling to room temperature, the solvent was removed *in vacuo* and the crude material was dissolved in THF and filtered through a thick pad of diatomaceous earth. Concentration of the THF and precipitation of the crude solution into water (500 mL) afforded a brown tacky solid. In the case of the P9AA and P15AA polymers, the solid material was dissolved in acetone and precipitated into a water:methanol mixture (1:1) to afford a brown tacky solid. In the case of the P21AA polymer, the residue was dissolved in THF and precipitated into methanol to afford a white solid. The polymers were dried in a vacuum oven at 65 °C overnight. Samples for GPC were prepared by sonicating a portion of the material at 30 °C in THF for a few hours prior to filtration and analysis. M_n and PDI values are relative to PS standards in THF at room temperature.

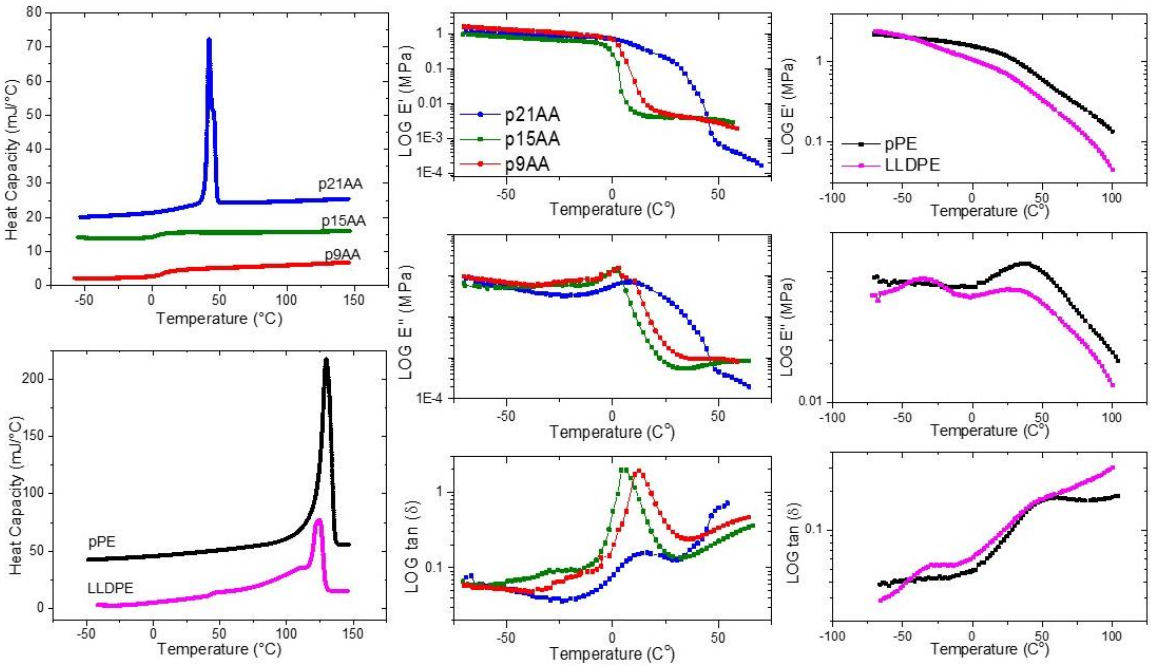

Figure D.1. Differential scanning calorimetry plots (left), and dynamic mechanical analysis storage (E'), loss (E'') and tan(δ) plots (right). The thermal transitions were extracted from DSC during the first scan with T_g at the point of inflection and T_m as the maximum in the melting peak, while the T_g extracted from DMA as the maximum in the tan(δ) peak. Additional peaks in tan(δ) appear in the semi-crystalline samples. The data are reported in Table 2.2 of the manuscript.

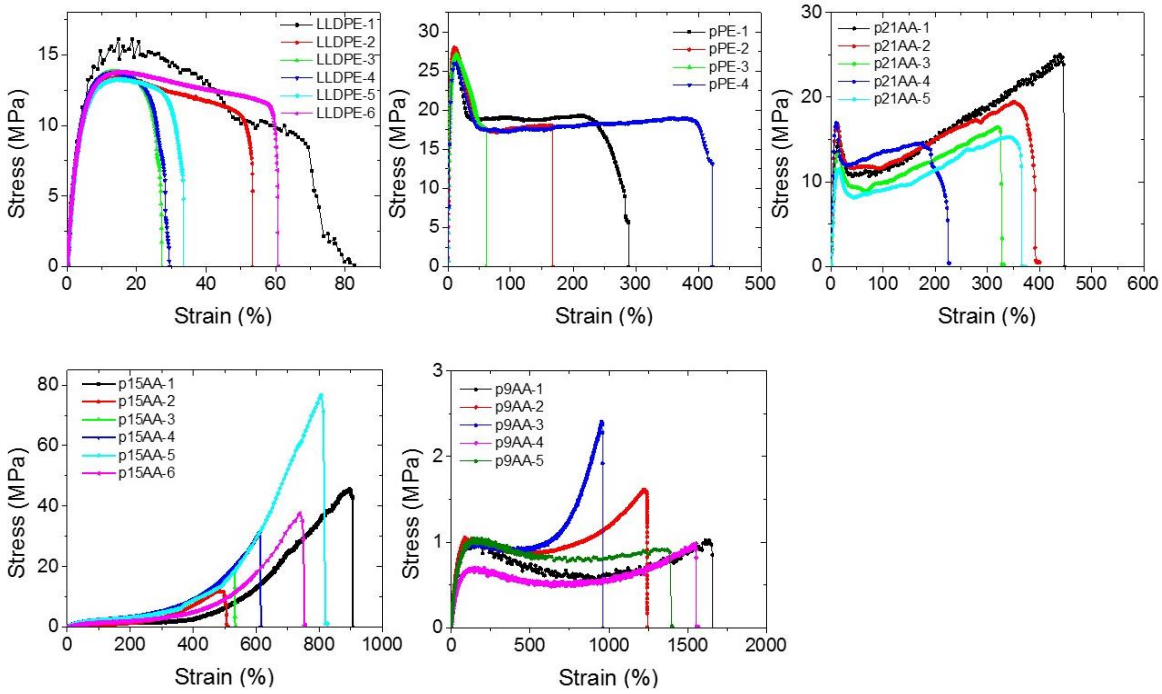

Figure D.2. Duplicate tensile tests at $\dot{\varepsilon}$=0.17^{-1}. The average and standard deviation of the data is reported in Table 2.2. The specific tensile curves that correspond to the *in situ* data are samples p9AA-1, p15AA-1, p21AA-1 and LLDPE-1.

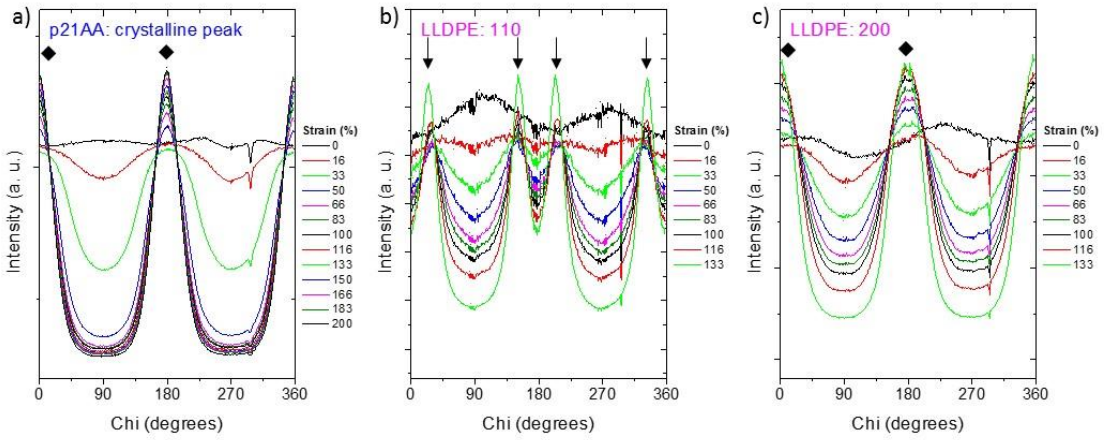

Figure D.3. The X-ray scattering profiles showing the intensity vs azumthal angle CHI for the semi-crystalline samples examined. a) In p21AA, which is semi-crystalline, there is no observable 4-point pattern or evidence for fine slip in the lamella. The chain scattering consistently orients during deformation converge into a 2-point pattern indicating alignment in the tensile direction, at 0° and 180° CHI (black diamonds). b) LLDPE during yielding exhibits fine slip within the PE lamellae leading to the martensitic transformation observed as a “4-point pattern” in the [110] peak show in in black arrows. c) The [200] peak aligns with deformation indicating consistently increased degrees of orientation and converge into a 2-point pattern in the tensile direction, at 0° and 180° CHI (black diamonds). The I vs CHI plots were integrated over a *q* range of 12.5-14nm^{-1} for p21AA, 12.5-14nm^{-1} for LLDPE [110], and 14.2-16nm^{-1} for LLDPE [200].

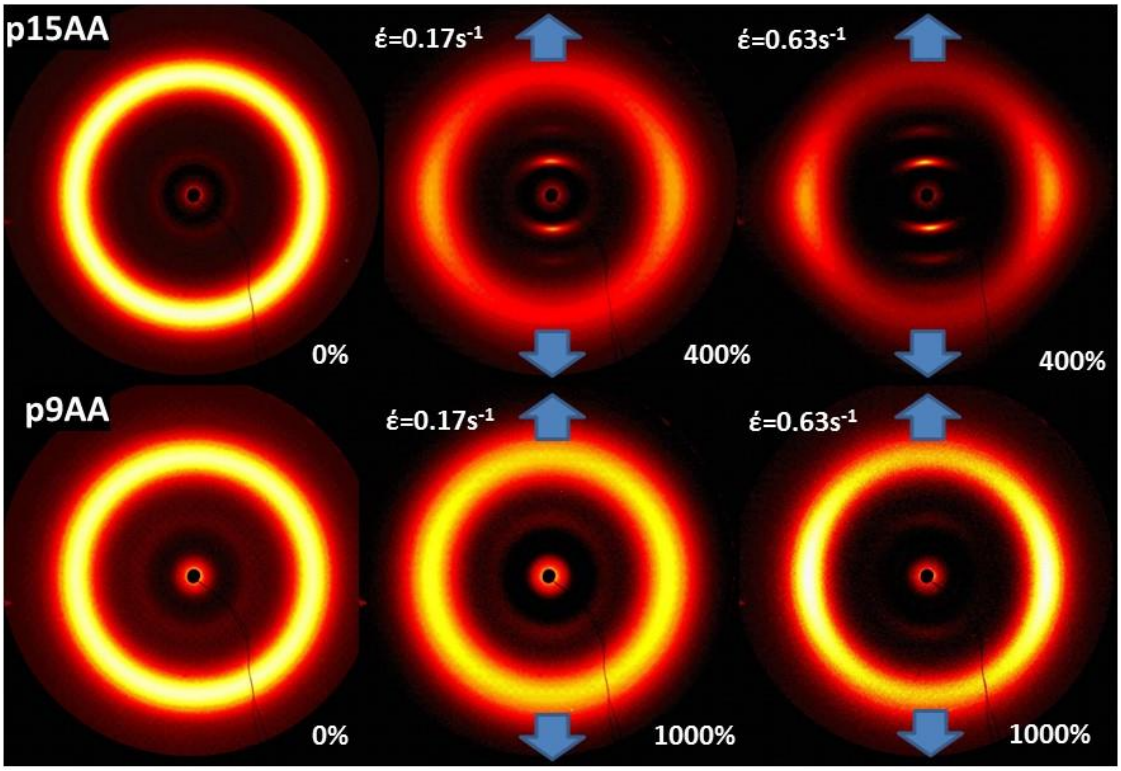

Figure D.4. The *in situ* X-ray scattering data for samples deformed at an intermediate and fast strain rate. Top) X-ray scattering data for p15AA at two different strain rates and captured at the same elongation both show a layered morphology. In the lower strain rate the amorphous halo shows less chain alignment, the acid aggregate peak is weaker and less oriented, and there are fewer higher order reflections. This confirms that the morphology is less aligned in the samples, consistent with the lower tensile behavior in Figure 3.2a-c of the manuscript. Bottom) The p9AA sample at the highest strain rate tested showed the persistence of the liquid-like morphology. The higher strain rate does result in an increase in the acid aggregate peak intensity and orientation but no layered morphology however was not observed.

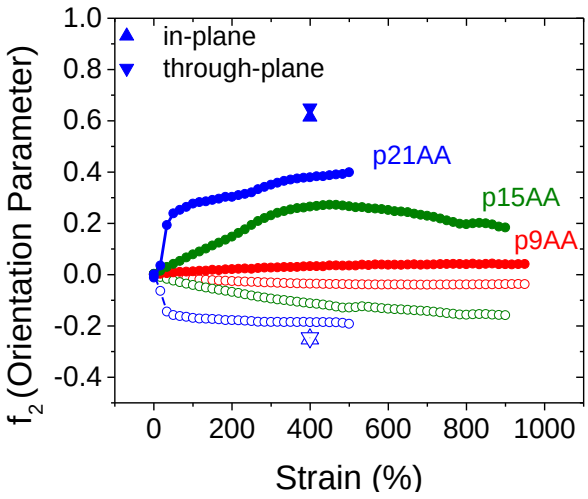

Figure D.5. Confirmation of fiber symmetry to validate use of Herman's orientation parameter, f_2. Blue triangles show the *ex situ* calculated f_2 for the acid peak (solid triangles) and amorphous halo (open triangles) symbols for p21AA. The Herman's orientation parameter confirmed that the morphology is nearly identical in the in-plane direction as the through-plane direction, consistent with fiber-symmetry. The sample of p21AA was deformed to 400% strain at room temperature. The sample was held at this fixed strain and X-ray scattering was performed *ex situ* to deformation in the in-plane direction and through-plane direction. The same *q*–range was used for the acid peak and amorphous halo as in Figure 2.6.

References

1. Baughman, T. W.; Chan, C. D.; Winey, K. I.; Wagener, K. B. *Macromolecules* **2007,** 40, (18), 6564-6571.

2. Frischknecht, A. L.; Todd, M. A.; Azoulay, J.; Bolintineanu, D. S.; Cordaro, J. G.; Hall, L. M.; Jenkins, J. E.; Lueth, C. A.; Murtagh, D.; Rempe, S. L. B.; Stevens, M. J.

Effects of Morphology on Ion Transport in Ionomers for Energy Storage; SAND2012-8304; Sandia National Laboratories: Sandia Report, Sept, 2012; pp 1-24.

APPENDIX E

Supplemental Information for Chapter 5

E.1 Simulations

Simulations Force Field. We performed all new simulations for this paper using the LOPLS force field. Specifically, we used the new C-C-C-C dihedral parameters and associated changes to the partial charges and LJ parameters from Siu *et al*.[2] The H-C-C-C dihedral came from Price *et al*.[3] (as also used by Siu et al.), while the C-C-C-O dihedral for the OH group in the acids is from Clifford *et al*.[4] (we also used this dihedral parameter in our previous simulations). All other parameters are from the original OPLS force field of Jorgensen *et al*.[5]

Simulation Thermostat. In our previous atomistic simulations to investigate structure in precise ionomers, we used the Langevin thermostat with a damping constant of 100.0 fs.[6-8] (Note that our previous simulations of precise acid copolymers used a Nosé-Hoover thermostat).[9] Here we found that simulations with the Langevin thermostat exhibited significantly slower relaxation than simulations with the Nosé-Hoover thermostat, also with a damping constant of 100.0 fs. Furthermore, simulations of hexadecane, PE, and the precise acid copolymers using the Nosé-Hoover thermostat are in better agreement with available QENS data. Hence all simulations in this paper used the Nosé-Hoover thermostat.

Hexadecane and PE Simulations using LOPLS. To further validate the accuracy of the LOPLS force field for dynamics, we performed MD simulations of both hexadecane and polyethylene and compared with QENS data in the literature. As shown in Figure E.1, for hexadecane there is very good agreement in *S(q,t)* between our simulations with the

LOPLS force field (lines) and QENS data reproduced from Morhenn *et al.*[10] (points). Similarly, Figure **5.2** shows good agreement between MD simulations of PE (with 84 carbons) using the LOPLS force field at 477K with QENS data on PE from Arbe and Colmenero.[11] These results give us confidence that the LOPLS force field yields accurate dynamics for long alkanes and PE oligomers.

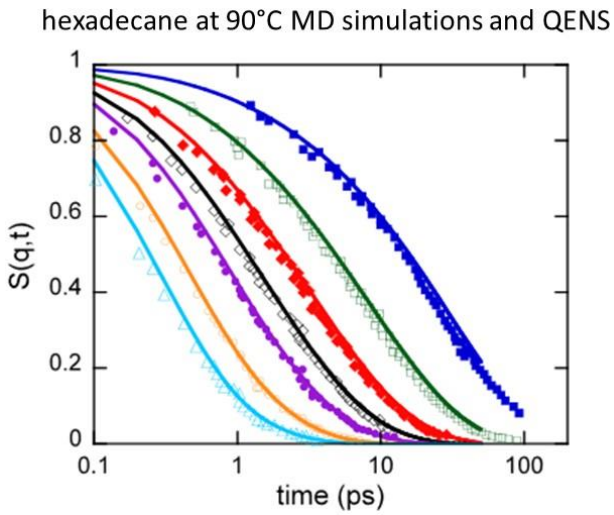

Figure E.1. Comparison of the LOPLS MD simulations calculated in this study with experimental QENS data reported by Morhenn et al[10] for hexadecane at 90 °C. Results are for q = 0.4, 0.6 0.8, 1.0, 1.2, 1.6 and 2.0 $Å^{-1}$, from the right to the left curves (dark blue squares at q = 0.4 $Å^{-1}$ to cyan triangles at q = 2.0 $Å^{-1}$).

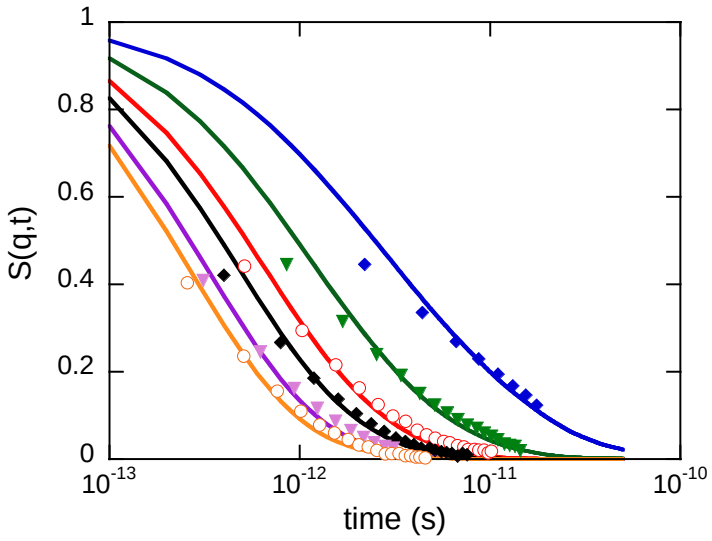

Figure 5.2. Comparison of the LOPLS MD simulations calculated in this study with experimental QENS data reported by Arbe and Colmenero for PE at 477K. Results are for q = 0.7, 1.0, 1.3, 1.5, 1.8 and 2.0 $Å^{-1}$, from the right to the left curves (dark blue diamonds at q = 0.7 $Å^{-1}$ to orange circles at q = 2.0 $Å^{-1}$).

Comparison of OPLS and LOPLS force fields. The LOPLS force field was developed to improve liquid state properties of long alkanes and lipids, and results in both improved thermodynamic and dynamic quantities.[2, 12] We found that the simulations using LOPLS result in faster relaxation in *S(Q,t)* and better agreement with our QENS data than simulations using the original OPLS force field. p21AA *S(Q,t)* results from both force fields are shown in Figure **E**.3.

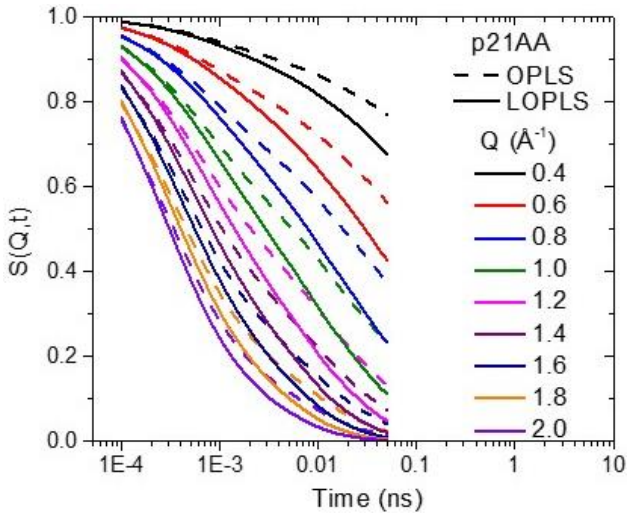

Figure E.3. Comparison of the OPLS (dashed) and LOPLS (solid) force fields used in MD simulations. Data is for p21AA at 423K.

E.2 Fitting with KWW of *S(Q, ω)* and *S(Q, t)* data

The QENS data from the disc-chopper spectrometer (DCS) were fit in the energy domain, *S(Q, ω)* using the Dave software developed by NIST.[1] The data were fit completely with two Lorentzian functions that are convoluted with the resolution function (functional forms reported in the software manual[1]). A Lorentzian in energy-space represents exponential decay (KWW with β = 1). The elastic incoherent structure factor (EISF) was calculated for each dynamic process. The fast and slow processes deviate at *Q*-values smaller than the amorphous halo (*Q* ~ 1.3Å^{-1}) as seen in the incoherent structure factor. The half-width at half-maximum of the Lorentzians provide an approximate timescale of dynamics as a function of length scale (Q^2). The fast dynamics are on the order of 0.1 ps and the slower dynamics on the order of 1 ps, similar to those calculated in MD simulations. The slow process has a larger Q^2 dependence when compared to the fast process, indicative of α- and β-processes.

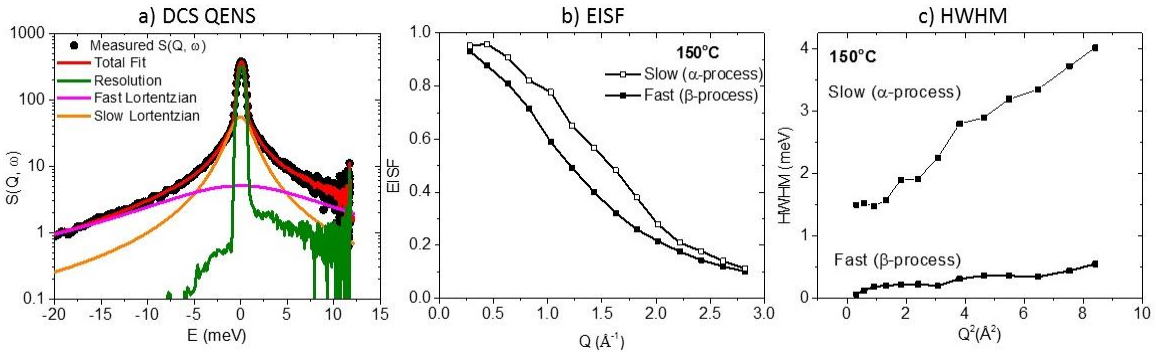

Figure E.4. a) Fitting of p9AA S(Q, ω) data from experimental QENS. b) The calculated elastic incoherent structure factor was calculated for both dynamic process. c) The Q^2 dependency of the Lorentzians half-width at half-maxima.

2KWW Fitting of S(Q,t) calculated from QENS data. The DCS QENS data were Fourier transformed with the Data Analysis and Visualization Environment (DAVE) software developed by NIST.[1]– Example data for p21AA is shown in Figure 5.5a and b. The experimental data was fit with two KWW's, examples for p21AA (Figure 5.5b) and p9AA (Figure 5.5c) are shown below. Both fast and slow components indicated by dashed lines and dotted line, respectively, are needed to fully capture the *S(Q,t)* data. Fitting the data with a single KWW failed. The extracted fitting parameters from QENS data and MD simulations are shown in Table 5.1.

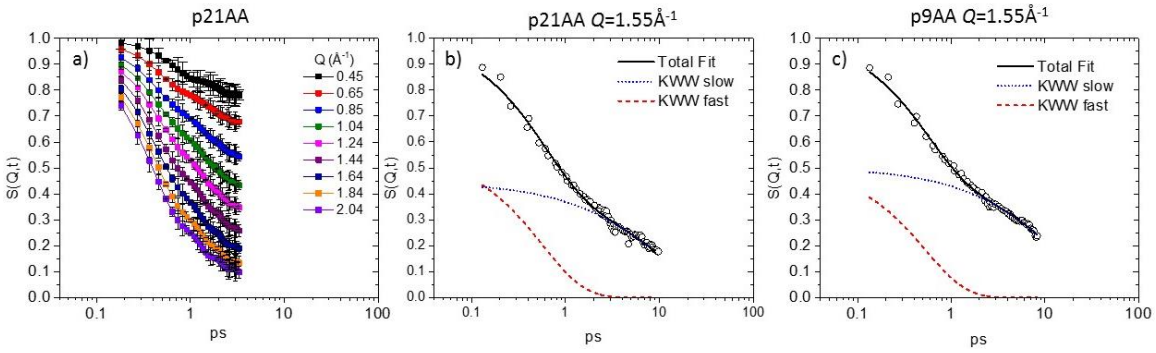

Figure 5.5. a) S(Q,t) transformed from experimental QENS data for p21AA at T = 150 °C. Example fitting of experimental QENS data with Equation 3 demonstrating the contribution of the two KWW functions for b) p21AA and c) p9AA.

Table 5.1. The extracted fitting parameters of the two KWW functions shown in Figure 5.5 at Q = 1.55Å^{-1} and T = 150 °C.

Material	**ϕ (slow)**	**τ fast (ps)**	**β fast**	**τ slow (ps)**	**β slow**
p21AA QENS	0.45	0.57	0.96	10.27	0.72
p21AA MD	0.34	0.58	1	3.45	0.49
p9AA QENS	0.5	0.53	0.99	12.96	0.73
p9AA MD	0.27	0.53	1	9.78	0.41

Fitting of MD S(Q,t) data with two KWW functions. The fits for all four polymers with two KWW functions (Equation 3) are shown.

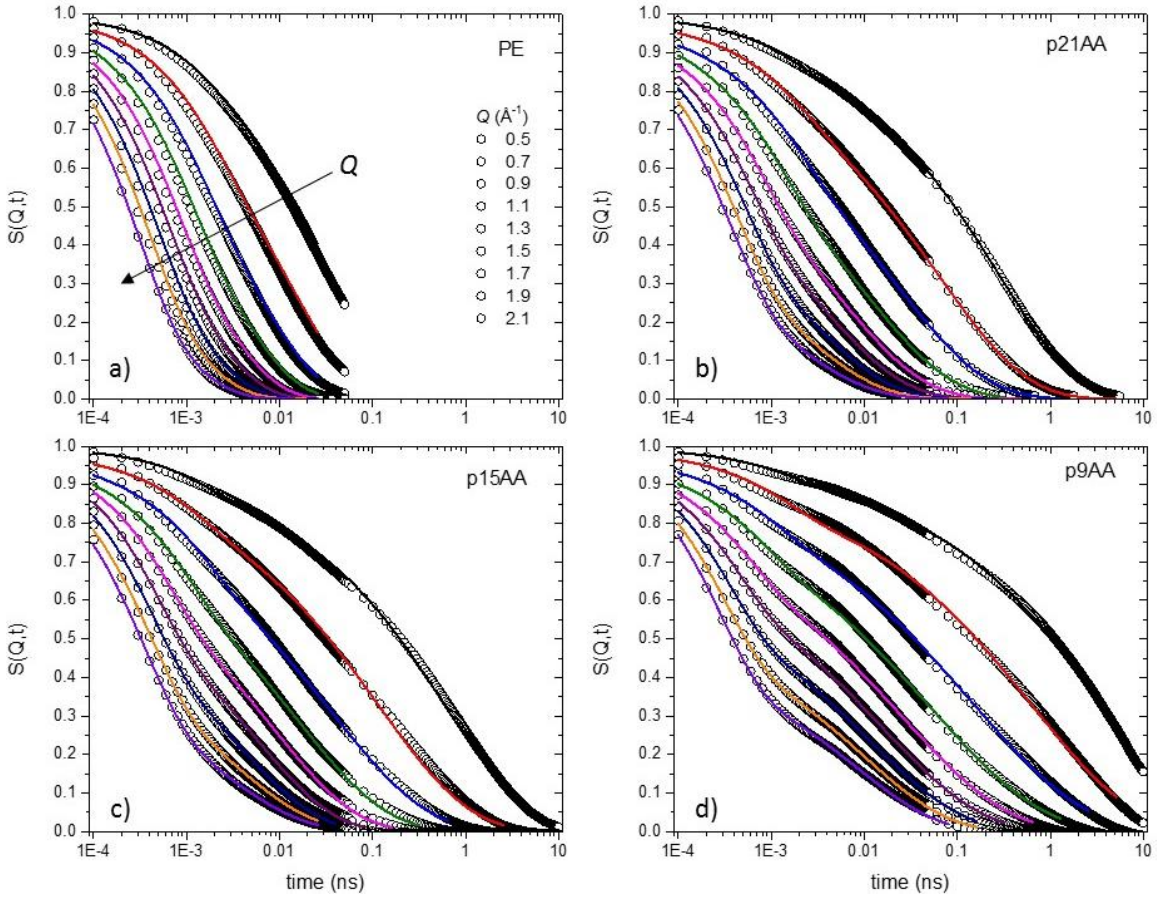

Figure 5.6. MD S(Q,t) data (points) and the fits of Equation 3 (lines) are shown for T = 150 °C for a range of Q-values. Q = 0.5 $Å^{-1}$ to 2.1 $Å^{-1}$ in 0.2$Å^{-1}$ steps.

E.3 References

1. Azuah, R. T.; Kneller, L. R.; Qiu, Y.; Tregenna-Piggott, P. L. W.; Brown, C. M.; Copley, J. R. D.; Dimeo, R. M. DAVE: A comprehensive software suite for the reduction, visualization, and analysis of low energy neutron spectroscopic data. *Journal of Research of the National Institute of Standards and Technology* **2009,** 114, (6), 341-358.

2. Siu, S. W. I.; Pluhackova, K.; Böckmann, R. A. Optimization of the OPLS-AA Force Field for Long Hydrocarbons. *Journal of Chemical Theory and Computation* **2012,** 8, (4), 1459-1470.

3. Price, M. L. P.; Ostrovsky, D.; Jorgensen, W. L. Gas-phase and liquid-state properties of esters, nitriles, and nitro compounds with the OPLS-AA force field. *J Comput Chem* **2001,** 22, (13), 1340-1352.

4. Clifford, S.; Bolton, K.; Ramjugernath, D. Monte Carlo simulation of carboxylic acid phase equilibria. *The Journal of Physical Chemistry B* **2006,** 110, (43), 21938-21943.

5. Jorgensen, W. L.; Maxwell, D. S.; TiradoRives, J. Development and testing of the OPLS all-atom force field on conformational energetics and properties of organic liquids. *Journal of the American Chemical Society* **1996,** 118, (45), 11225-11236.

6. Bolintineanu, D. S.; Stevens, M. J.; Frischknecht, A. L. Atomistic Simulations Predict a Surprising Variety of Morphologies in Precise Ionomers. *ACS Macro Letters* **2013,** 2, (3), 206-210.

7. Bolintineanu, D. S.; Stevens, M. J.; Frischknecht, A. L. Influence of Cation Type on Ionic Aggregates in Precise Ionomers. *Macromolecules* **2013,** 46, (13), 5381-5392.

8. Buitrago, C. F.; Bolintineanu, D. S.; Seitz, M. E.; Opper, K. L.; Wagener, K. B.; Stevens, M. J.; Frischknecht, A. L.; Winey, K. I. Direct Comparisons of X-ray Scattering and Atomistic Molecular Dynamics Simulations for Precise Acid Copolymers and Ionomers. *Macromolecules* **2015,** 48, (4), 1210-1220.

9. Lueth, C. A.; Bolintineanu, D. S.; Stevens, M. J.; Frischknecht, A. L. Hydrogen-bonded aggregates in precise acid copolymers. *J Chem Phys* **2014,** 140, (5), 054902.

10. Morhenn, H.; Busch, S.; Unruh, T. Chain dynamics in a hexadecane melt as seen by neutron scattering and identified by molecular dynamics simulations. *Journal of physics. Condensed matter : an Institute of Physics journal* **2012,** 24, (37), 375108.

11. Arbe, A.; Colmenero, J. Characterization of the “simple-liquid” state in a polymeric system: Coherent and incoherent scattering functions. *Physical Review E* **2009,** 80, (4).

12. Pluhackova, K.; Morhenn, H.; Lautner, L.; Lohstroh, W.; Nemkovski, K. S.; Unruh, T.; Böckmann, R. A. Extension of the LOPLS-AA Force Field for Alcohols, Esters, and Monoolein Bilayers and its Validation by Neutron Scattering Experiments. *The Journal of Physical Chemistry B* **2015,** 119, (49), 15287-15299.